7-3-2014

Experimental Deuteron Momentum Distributions with Reduced Final State Interactions

Hari Khanal
Florida International University, hkhan003@fiu.edu

FLORIDA INTERNATIONAL UNIVERSITY

Miami, Florida

EXPERIMENTAL DEUTERON MOMENTUM DISTRIBUTIONS WITH REDUCED FINAL STATE INTERACTIONS

A dissertation submitted in partial fulfillment of the

requirements for the degree of

DOCTOR OF PHILOSOPHY

in

PHYSICS

by

Hari P. Khanal

2014

To: Interim Dean Michael R. Heithaus
College of Arts and Sciences

This dissertation, written by Hari P. Khanal, and entitled Experimental Deuteron Momentum Distributions with Reduced Final State Interactions, having been approved in respect to style and intellectual content, is referred to you for judgment.

We have read this dissertation and recommend that it be approved.

Pete Markowitz

Misak Sargsian

Cem Karayalcin

Werner U. Boeglin, Major Professor

Date of Defense: July 3, 2014

The dissertation of Hari P. Khanal is approved.

Interim Dean Michael R. Heithaus
College of Arts and Sciences

Dean Lakshmi N. Reddi
University Graduate School

Florida International University, 2014

DEDICATION

This dissertation is dedicated to my late father Devi Prasad Khanal.

ACKNOWLEDGMENTS

I would like to acknowledge the support, guidance and encouragement of those individuals who put me on the path of this accomplishment.

First, I would like to thank my advisor, Prof. Werner Boeglin for his continuous support and excellent guidance through out this work. With his excellent mentoring, and the pleasant working environment he provided, I consider myself very fortunate to have him as my advisor. Working with Prof. Boeglin for six years gave me not only the excellent research experience but also the important lesson of life: sincerity and hard work. I am so greatful to him. I would also like to thank the members of my thesis committee: Profs. Cem Karayanlcin, Misak Sargsin, and Pete Markowitz for their suggestion and guidance during this work. Thanks to Prof. Brain Raue for his great advice when I was new graduate student at FIU.

I would also like to thank Jefferson Lab Hall A collaboration for their tremendous efforts to make this experiment successful. Thanks to Ole Hansen and Robert Michaels for their support in software development during the data processing. I would like to express my sincerely gratitude to all individuals who worked at the time of data collection, and the spoke persons of this experiment.

I would like to thank my lab mates for their support, and creating fun working environment. I am greatful to Eric Pooser for software discussions and reading first draft of my thesis. Thanks to Dipak, Jason, Will and Adam for their suggestions to improve my work, and presentation skills

I would like to thank all faculty and staff members of Tribhuvan University Physics Department for providing the excellent education. Special thank goes to Prof. Devendra Raj Mishra and Prof. Shekhar Grung for their great advices and suggestions about life, and about being good physicist.

I would like to express my deepest gratitude to my late father, Devi Prasad Khanal, for his support, encouragement, and scrifies to my eduction. I am always indebted for every things he did for me. Thanks to my mother Thama Devi, bother, Lokpriya, and sister, Gita for their unconditional love, and scrifies to make me more happy in my personal goal.

Finally, I would like to thank my beautiful wife, Anuja and son, Aarav for their understanding my busy life. I am so greatful with Anuja for her moral support during this work.

Thank you all again.

ABSTRACT OF THE DISSERTATION

EXPERIMENTAL DEUTERON MOMENTUM DISTRIBUTIONS WITH REDUCED FINAL STATE INTERACTIONS by

Hari P. Khanal

Florida International University, 2014

Miami, Florida

Professor Werner U. Boeglin, Major Professor

This dissertation presents a study of the $D(e, e'p)n$ reaction carried out at the Thomas Jefferson National Accelerator Facility (Jefferson Lab) for a set of fixed values of four-momentum transfer $Q^2 = 2.1$ and 0.8 $(\mathrm{GeV/c})^2$ and for missing momenta p_m ranging from $p_m = 0.03$ to $p_m = 0.65$ GeV/c. The analysis resulted in the determination of absolute $D(e, e'p)n$ cross sections as a function of the recoiling neutron momentum and it's scattering angle with respect to the momentum transfer $\vec{q}$. The angular distribution was compared to various modern theoretical predictions that also included final state interactions. The data confirmed the theoretical prediction of a strong anisotropy of final state interaction contributions at Q^2 of 2.1 $(\mathrm{GeV/c})^2$ while at the lower Q^2 value, the anisotropy was much less pronounced. At Q^2 of 0.8 $(\mathrm{GeV/c})^2$, theories show a large disagreement with the experimental results. The experimental momentum distribution of the bound proton inside the deuteron has been determined for the first time at a set of fixed neutron recoil angles. The momentum distribution is directly related to the ground state wave function of the deuteron in momentum

space. The high momentum part of this wave function plays a crucial role in understanding the short-range part of the nucleon-nucleon force. At $Q^2 = 2.1$ (GeV/c)^2, the momentum distribution determined at small neutron recoil angles is much less affected by FSI compared to a recoil angle of 75^0. In contrast, at $Q^2 = 0.8$ (GeV/c)^2 there seems to be no region with reduced FSI for larger missing momenta. Besides the statistical errors, systematic errors of about 5 -6 % were included in the final results in order to account for normalization uncertainties and uncertainties in the determination of kinematic veriables. The measurements were carried out using an electron beam energy of 2.8 and 4.7 GeV with beam currents between 10 to 100 μA. The scattered electrons and the ejected protons originated from a 15cm long liquid deuterium target, and were detected in conicidence with the two high resolution spectrometers of Hall A at Jefferson Lab.

TABLE OF CONTENTS

LIST OF FIGURES

LIST OF TABLES

TABLE PAGE

Chapter 1

Introduction

1.1 Motivation

While the nucleon-nucleon (NN) interaction is attractive at distances of about ~ 1.5 fm, a strong repulsive core at short distances (<1 fm) is required for the stability of nuclei. The short-range part of the NN interaction is currently only poorly understood, and very difficult to access experimentally. The exclusive electo-disintegration of the deuteron offers a possible way to access this elusive part of the NN interaction. The deuteron (D) is the starting point of understanding the nuclear force between nucleons because it only consists of a proton and a neutron. With a suitable reaction and kinematic settings, one can study the NN interaction in the deuteron without the additional effects of three body interactions. The $D(e, e'p)n$ reaction, where e and e' denote the incident and the scattered electron respectively, is one of the best reactions for such studies since the final state is completely specified kinematically. However, extracting information regarding to the deuteron's structure requires a quantitative understanding of the full reaction dynamics.

Although the deuteron is a loosely bound two body system, its high momentum structure is similar to that of more complex nuclei. A precise measurement of the high momentum component of the deuteron ground state wave function is the key to understanding the short-range part of nuclear structure. Three types of reactions

are used to study the high momentum part of the deuteron wave function: elastic scattering, inclusive and exclusive electro-disintegration reactions [3]. High nucleon momenta can be investigated through the exclusive, quasielatic electro-disintegration of the deuteron at high missing momenta. The missing momentum $\vec{p}_m$ is defined as the momentum of the recoiling neutron $\vec{p}_m = \vec{q} - \vec{p}_p$, where $\vec{q}$ is the three-momentum of the exchanges virtual photon, and $\vec{p}_p$ is the momentum of the outgoing proton as shown in Fig. 1.1. In the Plane Wave Impulse Approximation (PWIA), the virtual photon is absorbed by a single bound nucleon, which leaves the nucleus without further interaction. Within PWIA, $-\vec{p}_m$ corresponds to the initial momentum of the bound target nucleon before the interaction. Thus, the main objective of these studies is to determine the $D(e, e'p)n$ reaction cross section at different p_m values. However, additional processes such as final state interactions (FSI), where the outgoing proton interacts with the recoiling neutron, meson exchange currents (MEC), where the virtual photon couples to the exchanged meson, and isobar configurations (IC), where the nucleon is excited to an intermediate state (Δ), all contribute to the measured cross section.

At high Q^2 and high p_m, FSI can dominate the reaction while contributions of MEC and IC decrease with increasing Q^2. One important consequence of these additional processes is that the momentum carried by the bound nucleon before the interaction with the electron is not equal to $-\vec{p}_m$ [9]. Thus, FSI can significantly change the momentum of the detected nucleon. The present study of the deuteron helps to probe the effect of different reactions mechanisms on the reaction cross section. Differential

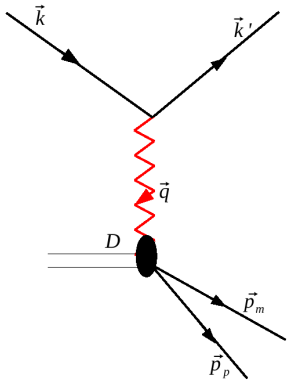

Figure 1.1: Feynman diagram for electro-disintegration of deuteron

cross sections were measured over a wide range of neutron recoil angles for different missing momenta to test the validity of various reaction models such as the PWIA, standard Glauber Approximation [10] and Generalized Eikonal Approximation[11, 12, 13].

In PWIA, the incoming and scattered electrons, and the ejected protons are described by plane waves, and the ejected proton is assumed to have no interaction with the residual neutron. The combination of these assumptions leads to the factorized description of the $D(e, e'p)n$ cross section [14]. The reduced cross section or momentum distribution, $\rho(p_m)$ can be determined by integrating the cross section over the missing energy and dividing it by $K\sigma_{ep}$, where K is a kinematic factor and σ_{ep} is the off-shell electron-proton cross section [15]. In the present work, reduced cross sections were determined at $Q^2 = 0.8$ and 2.1 GeV ^{2} for a set of four fixed recoil angles.

1.2 Experiment Overview

Electron scattering provides a powerful tool for studying the structure of the nucleons and nuclei because the electro-magnetic interaction is well understood, and is well de-

scribed by Quantum Electrodynamics (QED). The interaction between the electron and the target nucleus is weak($\alpha \approx 1/137$) as compared to the hadronic interaction, and is well described by the model of single virtual photon exchange between the incident electron and bound nucleon. At low energy and momentum transfers, the virtual photon interacts coherently with the entire nucleus, scattering elastically or exciting a bound nuclear state. At higher energy and momentum transfer, the scattering is dominated by quasielatic scattering, where the photon interacts with a single bound nucleon. As the energy and momentum transfers increase further, the photon probes smaller distance scales, and the interaction will be more sensitive to the quark degrees of freedom [16].

In this experiment, energy and momentum transfers were chosen in such a way that different missing momenta and different recoil angles could be measured. Each of the kinematic settings emphasizes different aspects of the reaction mechanism. In order to study the deuteron short-range structure, one must select kinematics which minimize FSI, MEC and IC reaction effects or correctly account for such effects. Theoretical treatments of MEC and IC at high Q^2 are very difficult and have a substantial amount of theoretical uncertainties associated with them. For energy transfers, ω, below the quasielatic peak, $x_{bj} > 1$ ($x_{bj} = \frac{Q^2}{2\omega m_p}$), where x_{bj} is the Bjorken scaling variable, and MEC and IC are expected to be small since the energy transfer is relatively low.

1.3 Previous Experiments

Several experiments measured the $D(e, e'p)n$ reaction cross section at low Q^2 for a wide range of missing momenta [1, 4, 17, 18] at various laboratories such as MIAMI

(Mainz, Germany) [1], SLAC (Standford, CA, USA) [19], NIKHFF (Amsterdam, The Netherlands)[20], MIT-Bates (Middleton, USA) [21], ALS (Saclay, France) [22] and CEBAF (Newport News, VA, USA) [2, 3, 4]. Before experiment E01020, the cross section were measured for large missing momenta, p_m up to 0.95 GeV/c only at small $Q^2 \approx 0.1 - 0.4$ GeV^2 [1] or at large $Q^2 \approx 1.2$ GeV ^{2} for small $p_m \leq 0.15$ GeV/c [19]. From these experiments it has been observed that with increasing p_m, FSI, MEC and IC effects increase rapidly and the PWIA is no longer valid. Fig. 2.2 shows the $D(e, e'p)n$ cross section as a function of missing momentum measured at MAMI [1] and Arenhovel's calculations with FSI, MEC and IC effects [23].

In previous experiments, truly systematic studies in the $D(e, e'p)n$ cross section could not be carried out due to the limitations of the various accelerators. For example, accelerator and spectrometer energy limitations in Mainz [1], Saclay [22], and NIKHIFF [20] forced the data to be taken in the Δ region of the inclusive (e, e') spectrum where lack of knowledge of the reaction mechanism made it difficult to access the short distance structure of the deuteron. Even though the accelerator energy is high at SLAC [19], the limitations in the duty factor restricted measuring a wide range of missing momenta. On the other hand, Jefferson Lab has an unique combination of high beam energy, luminosity and duty factor that allows one to study the reaction $D(e, e'p)n$ over a broad kinematic range at both high p_m and high Q^2.

In order to measure the angular dependence of FSI, the angular distributions of the recoiling neutrons were measured in different experiments [2, 3]. Fig. 1.3 shows the angular distribution of the recoiling neutron measured at Jefferson Lab in Hall B[2].

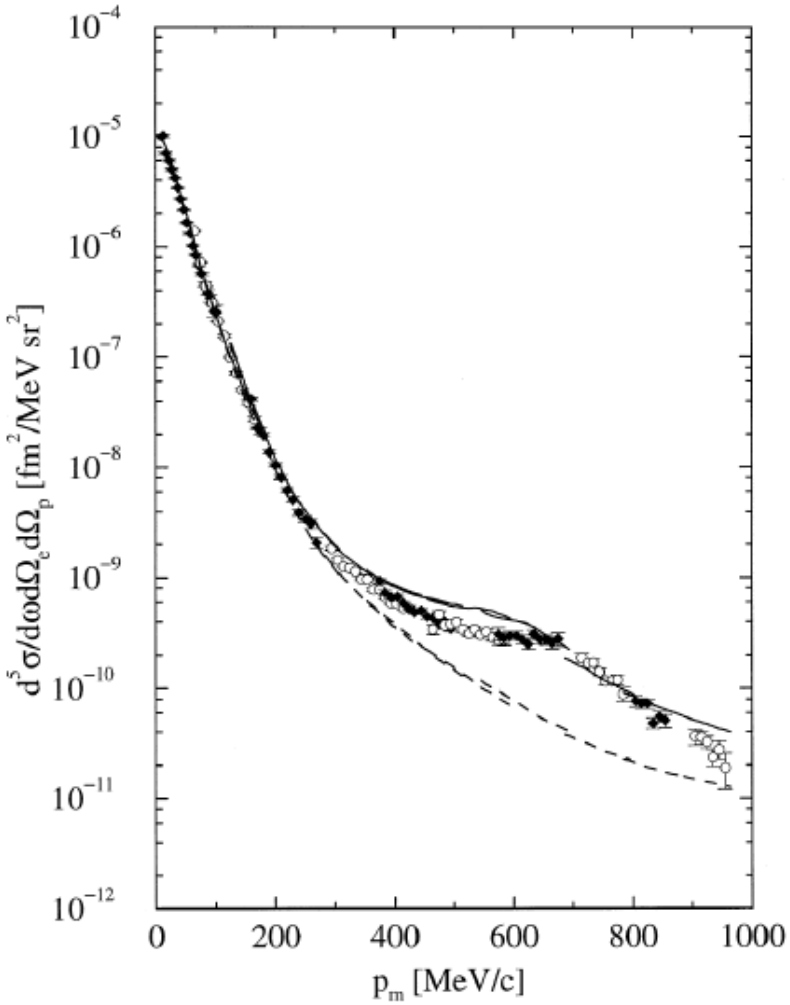

Figure 1.2: Comparison of the measured $D(e, e'p)n$ cross section at MAMI to the calculation by Arenhovel with (solid curve) and without (dashed curve) MEC and IC [1]

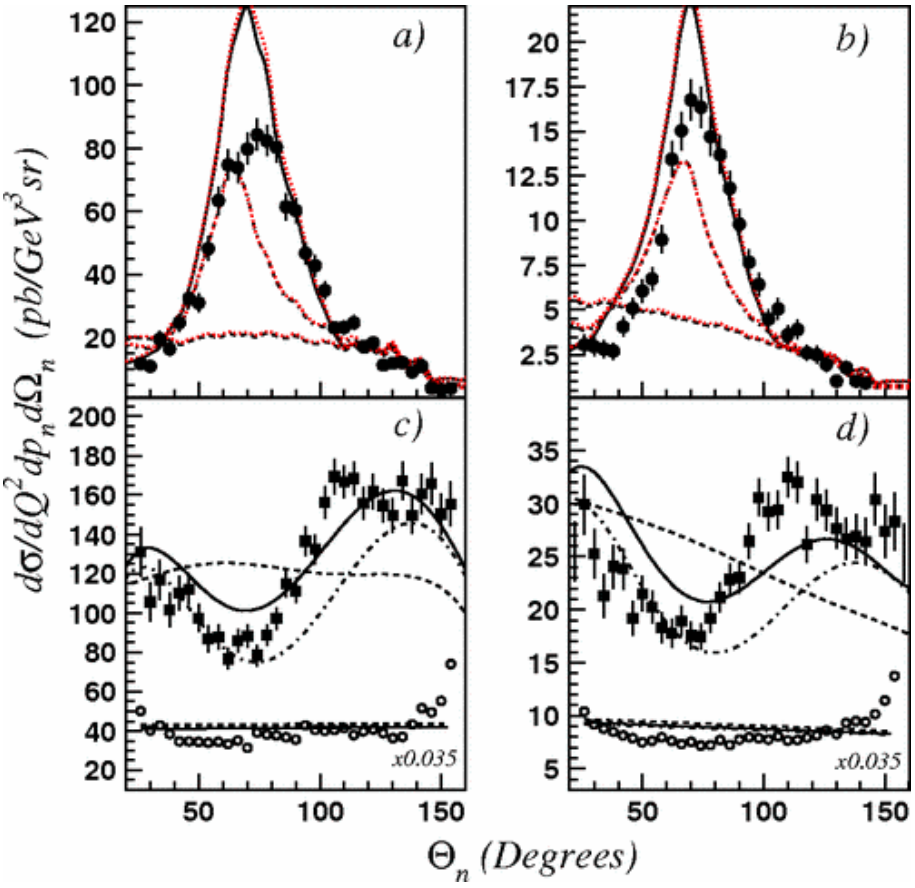

Figure 1.3: The recoil neutron angular distribution for (a) $Q^2 = 2\pm0.25$ (GeV/c)^2, $400< p_m < 600$ MeV/c,(b) $Q^2 = 2\pm0.5$ (GeV/c)^2, $400< p_m < 600$ MeV/c,(c) $Q^2 = 2\pm0.25$ (GeV/c)^2, $200< p_m < 300$ MeV/c, (d) $Q^2 = 3\pm0.5$ (GeV/c)^2, $200< p_m < 300$ MeV/c. The data for $0 < p_m < 100$ MeV/c are plotted in the bottom part of (c) and (d) and scaled by 0.035. The solid curves are the calculations with the Paris potential for PWIA, PWIA+FSI, and PWIA+FSI+MEC+IC[2].

At $Q^2 = 3.5$ (GeV/c)^2, the angular distribution of the neutron for $p_m = 0.2$, 0.4 and 0.5 GeV/c as measured at Jefferson Lab in Hall A, and a comparison to the theoretical calculations [3] is shown in Fig. 1.4. In both experiments [2] and [3], FSI effects are found be maximal around a recoil angle of 70^0.

Reduced cross sections or momentum distributions in the $D(e, e'p)n$ reaction were also measured in a previous JLab experiment E94-004 [4]. The cross sections were

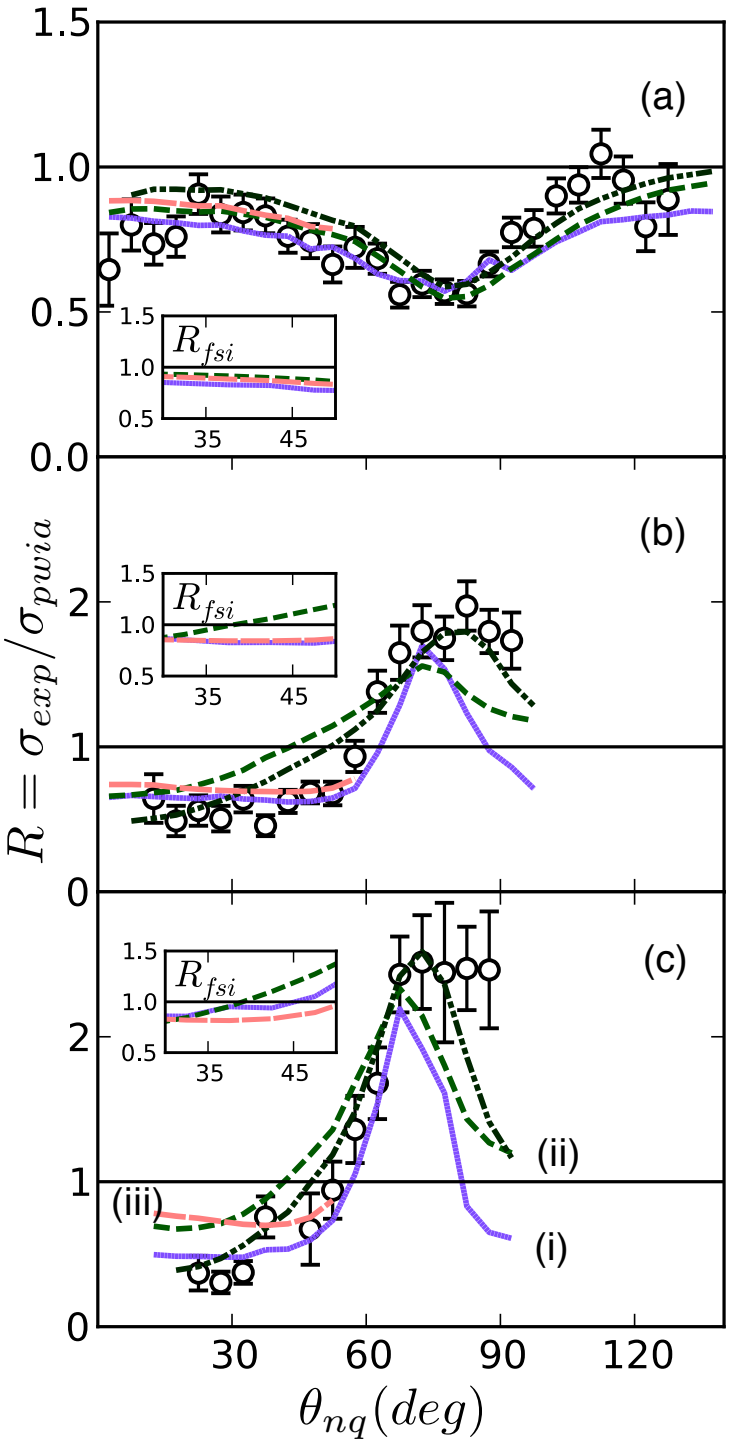

Figure 1.4: The ratio R($\theta_{nq} = \sigma_{exp}/\sigma_{PWIA}$). (a) $p_m = 0.2$ GeV/c,(b) $p_m = 0.4$ GeV/c, (c) $p_m = 0.5$ GeV/c. The color lines denote the theoretical calculation with different models [3].

measured near the top of the quasielatic peak (Bijorken $x_{bj} = 0.964$) at $Q^2 = 0.665$ (GeV/c)^2 and for neutron recoil momenta p_m up to 550 MeV. Fig. 1.5 shows the reduced $D(e, e'p)n$ cross section for experiment E94-004.

1.4 Theoretical Models

Several theoretical models were developed to describe the exclusive electro-disintegration of the deuteron at high Q^2 and high recoil momenta, p_m. Many of these models used the most advanced nucleon-nucleon (NN) potentials such as the Paris, Bonn or Argonne V18 model [24, 25, 26] to calculate the deuteron initial and final state wave functions.

Arenhovels's model [27, 28, 29] makes it possible to investigate the dynamical feature of the nuclear system with the use of a polarized target and/or of a polarized beam, and to see to what extent the various observables are affected by the NN interaction, and by non-nucleonic effects like meson exchanged currents (MEC) and isobar configurations (IC). Arenhovel's calculations are not expected to be valid at the high energies and momentum transfers measured in this work. FSI at high energies can be described as small angle rescatterings of the ejected nucleon with the residual system. In this case, most of the theoretical calculations for the $D(e, e'p)n$ reaction are based on Glauber theory (the momentum transfer in the rescattering of the two nucleons is purely transverse) derived models such as the generalized eikonal approximation [5, 30, 31, 32, 33] or the diagrammatic approach used by J.M.Laget [34]. Most of these calculations use the central part of the NN scattering amplitude only. S. Jeschonnek and W. van Orden [32] present a new approach that uses a fully relativistic formalism

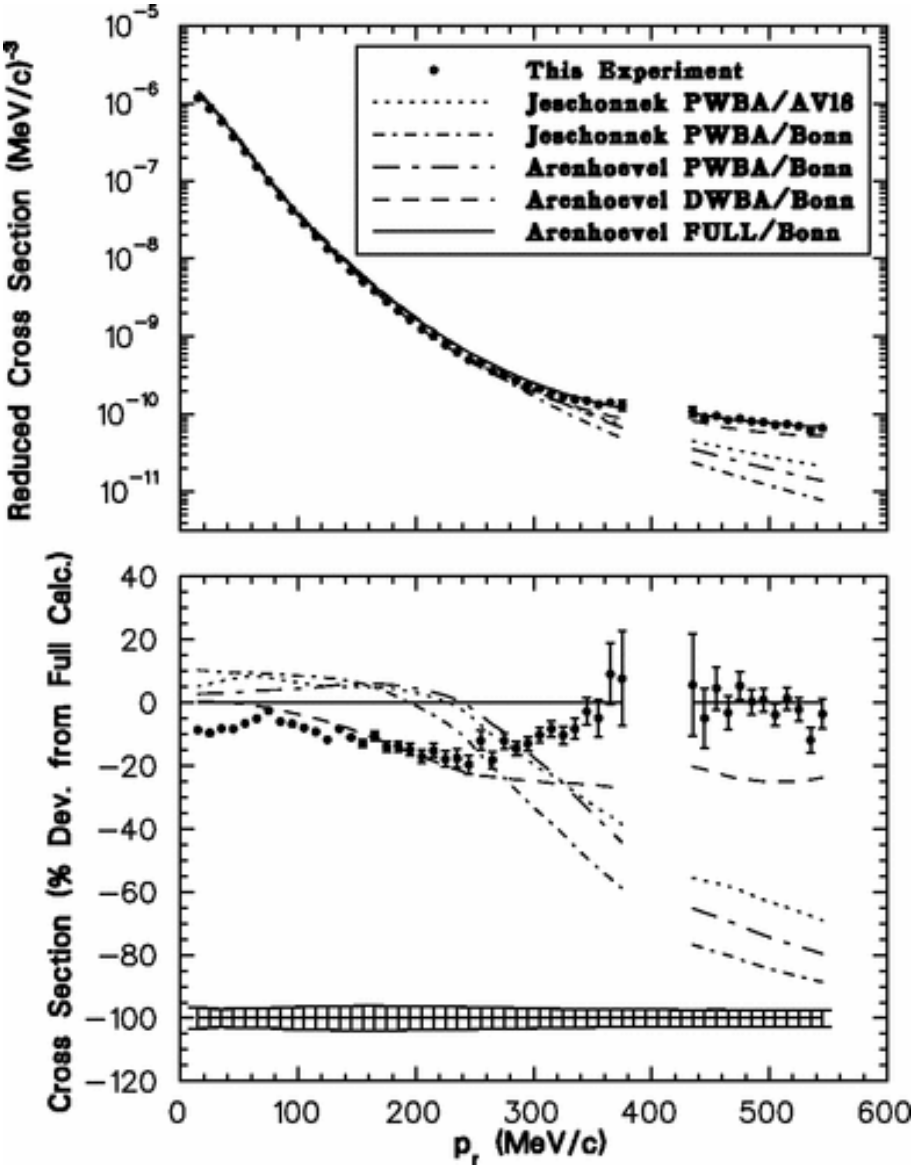

Figure 1.5: The reduced $D(e, e'p)n$ cross section for Jefferson Lab Experiment E94-004, compared with various models [4].

and investigates the different contributions to the NN scattering amplitude: central, spin-orbit, and double spin-flip part without any approximations on the energy and momentum transferred. In the conventional Glauber approximation, the electron scatters on a proton at rest which propagates on-shell and rescatters on the neutron, which is also at rest. In the lab frame the soft neutron recoils with negligibly small momentum at 90^o with respect to the fast proton, which is emitted along the direction of momentum transfer $\vec{q}$. This approximation is no longer valid at a high missing momentum, p_m. In the generalized eikonal approximation (GEA), relativistic effects due to finite energy and momentum of the recoiling nucleon are taken into account, and the angle of the rescattering peak at high recoil momenta moves to around 70^o. Therefore, the classical Glauber model can not describe the $D(e, e'p)n$ reaction at large angle and large recoil momenta.

M. Sargsian's model is based on the GEA [33, 35] where the scattering amplitudes are calculated in a covariant form using effective Feynman diagram rules. This model describes the high Q^2 exclusive electro-disintegration of the deuteron based on the virtual nucleon approximation. The following are the assumptions made for the virtual nucleon approximation.

- Only the pn component of the deuteron is considered, neglecting inelastic initial-state transitions. The deuteron isosinglet state limits the kinetic energy of the recoil nucleon i.e $T_n < 500$ MeV/c.

- The negative energy projection of the virtual nucleon propagator gives a neg-

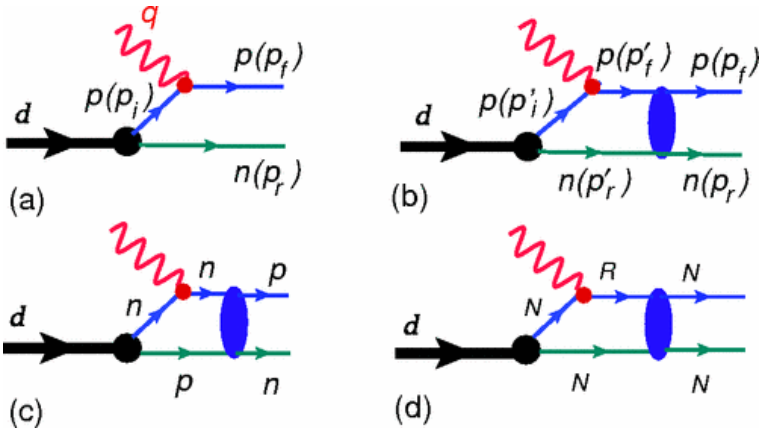

Figure 1.6: The Feynman diagram with GEA [5].

ligible contribution to the scattering amplitude. This condition is satisfied if $M_d - \sqrt{(m^2 + p^2)} > 0$, where M_d is the mass of the deuteron and p is the relative momentum of the bound pn system.

- At large Q^2, the interactions of the virtual photon with the exchanged mesons are neglected.

The first two conditions are satisfied only at $p_m < 700$ MeV/c. M. Sargsian's model completely neglects the non-nucleonic contributions such as MEC and IC in the reaction cross section. Fig. 1.6 shows the Fynman diagram withins GEA, where (a) corresponds to PWIA, (b) forward FSI, (c) charge-exchange FSI, and (d) Δ isobar (IC) contributions. In this model, only the first three diagrams are used for the cross section calculation. Therefore, the total scattering amplitude is the sum of the PWIA, forward and charge-exchange FSI amplitudes:

$$\langle s_f, s_r | A^\mu | s_d \rangle = \langle s_f, s_r | A^\mu_p | s_d \rangle + \langle s_f, s_r | A^\mu_1 | s_d \rangle + \langle s_f, s_r | A^\mu_{1,chex} | s_d \rangle. \qquad (1.1)$$

All wave functions associated with scattering amplitude were calculated using the Paris potential [36].

J.M. Laget's [34, 37, 38] model uses a diagrammatic approach to calculate the nucleon-nucleon scattering amplitude, and the reaction cross section. In his model [34], he calculates the PWIA and FSI amplitudes for the $D(e, e'p)n$ reaction using relativistic expressions of the proton $J_p(q^2)$ and neutron $J_n(q^2)$ current densities. The IC and MEC amplitudes are calculated by taking into account both π and ρ exchange.

Chapter 2

Theory

2.1 The Reaction D(e, e'p)n

For light nuclei, like the deuteron, one photon exchange is assumed to be a good approximation in the process of electron scattering. Fig. 2.2 shows schematically the $D(e,e'p)n$ reaction, where $k^\mu = (E, \vec{k})$ and $k'^\mu = (E', \vec{k}')$ are the four-momenta of the incident and the scattered electrons, $p_p^\mu = (E_p, \vec{p}_p)$ and $p_n^\mu = (E_n, \vec{p}_n)$ are the four-momenta of the ejected proton and the recoiling neutron, and $p_D^\mu = (E_D, \vec{p}_D)$ is the four-momentum of the initial target. In the relativistic limit, the mass of the electron can be neglected as compared to its momentum, such that $k \equiv |\vec{k}| = E$ and $k' \equiv |\vec{k}'| = E'$. The vectors $\vec{k}$ and $\vec{k}'$ form the scattering plane, and the vectors $\vec{q}$ and $\vec{p}_p$ form the reaction plane. ϕ denotes the angle between the reaction plane and the scattering plane. In Hall A, only the two possible values of ϕ, 0^0 and 180^0 for the central spectrometer settings can be set. The kinematic setting with $\phi = 0$ is refered to as in-plane forward of $\vec{q}$, and the kinematic setting with $\phi = 180^0$ is referred to as in-plane backward of $\vec{q}$. When an incident electron is scattered by the nucleus, it emits a virtual photon. The four-momentum carried by the virtual photon is given by:

$$q^\mu = k^\mu - k'^\mu = (\omega, \vec{q}), \tag{2.1}$$

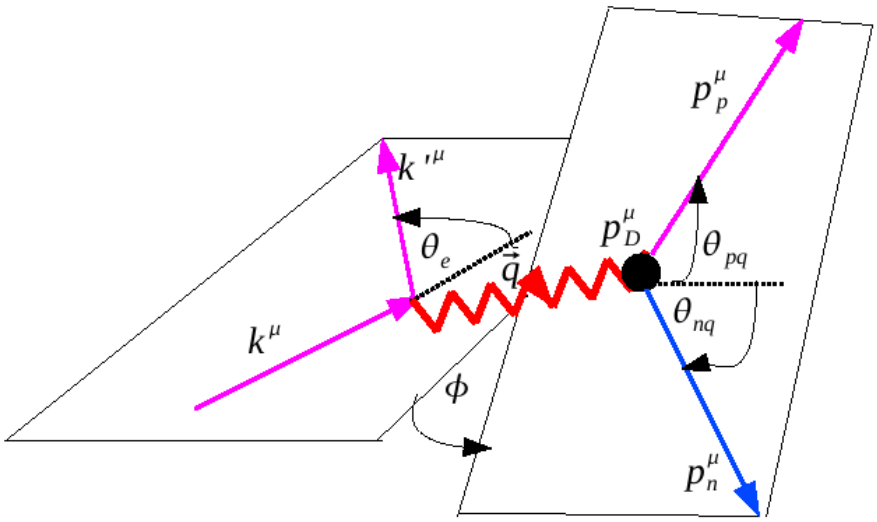

Figure 2.1: Feynman Diagram of Electro-disintegration of Deuteron

where:

$$\omega = E - E', \tag{2.2}$$

is the energy transfer and

$$\vec{q} = \vec{k} - \vec{k'} \tag{2.3}$$

is the 3-momentum vector of the virtual photon. The direction of the virtual photon with respect to the electron beam direction is given by:

$$\cos\theta_q = \frac{k - \vec{k'}\cos\theta_e}{q}, \tag{2.4}$$

where θ_e is the electron scattering angle.

The square of the four-momentum transfer is given by:

$$q_\mu^2 = -Q^2 = \omega^2 - q^2 = 2(\vec{k} \cdot \vec{k}' - EE' + m_e^2). \tag{2.5}$$

Neglecting the electron mass, one can write

$$Q^2 = 4EE' \sin^2(\frac{\theta_e}{2}). \tag{2.6}$$

The target is initially at rest i.e. $\vec{p}_D = 0$, and $E_d = M_d$. The square of the invariant mass is given by

$$W^2 = (\omega + M_d)^2 - q^2 = M_d^2 + 2\omega M_d - Q^2 \tag{2.7}$$

Using conservation of energy, one can write

$$\omega + M_d = E_p + E_n = M_p + T_p + M_n + T_n, \tag{2.8}$$

where T_p and T_n are the kinetic energies of the out-going proton and the recoiling neutron, respectively. From Eqn. 2.8, one can calculate the missing energy of the reaction, which is equal to the binding energy of the deuteron:

$$E_{miss} = M_d - M_p - M_n = \omega - T_p - T_n \tag{2.9}$$

The missing momentum $\vec{p}_m$ is defined as the momentum of the undetected residual

system. In this reaction, $\vec{p}_m$ refers to the momentum of the recoil neutron, which is given by

$$\vec{p}_m = \vec{q} - \vec{p}_p. \tag{2.10}$$

Where $\vec{p}_p$ is the momentum vector of the out-going proton. The angle between the missing momentum and the momentum of the virtual photon, θ_{nq}, can be written as:

$$\cos\theta_{nq} = \frac{q - p_p \cos\theta_{pq}}{\sqrt{q^2 + p_p^2 - 2qp_p \cos\theta_{pq}}}, \tag{2.11}$$

where θ_{pq} is the angle between the momentum transfer and the out-going proton. In deuteron electro-disintegration, θ_{nq} is the recoil angle of the neutron with respect to the momentum transfer. When the proton is detected on either side of $\vec{q}$, conservation of momentum requires that $\vec{p}_m$ should be close to perpendicular to $\vec{q}$ ($\theta_{nq} \approx 90$), and the kinematic setting is called "perpendicular" kinematics. If the proton is detected along the direction of $\vec{q}$ ($\theta_{pq} \approx 0$), then the kinematic setting is called "parallel" kinematics. In this case, $\vec{p}_m$ is parallel to $\vec{q}$, if $q > p_p$, and anti-parallel if $q < p_p$.

In Plane Wave Impulse Approximation (PWIA), the ejected proton carries all the momentum of the virtual photon, and the missing momentum $\vec{p}_m$ is equal to the initial momentum of neutron $\vec{p}_{in}$. The total initial momentum of the deuteron in the ground state can be written as:

$$\vec{p}_{in} + \vec{p}_{ip} = 0, \tag{2.12}$$

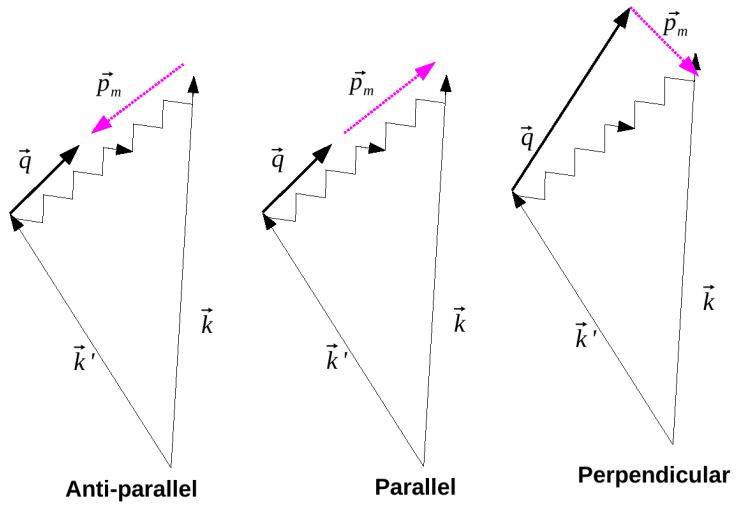

Figure 2.2: Kinematic Settings Convention in the $D(e, e'p)n$ reaction

where p_{ip} is the initial momentum of the proton. In PWIA, we have

$$\vec{p}_{in} = \vec{p}_m. \tag{2.13}$$

Therefore, one can write:

$$\vec{p}_m = -\vec{p}_{ip}. \tag{2.14}$$

Therefore, in PWIA, the momentum of the recoil neutron, $\vec{p}_m$, is equal and opposite to the initial momentum of the proton.

2.2 Reaction Cross Section

The differential cross section of the exclusive (e, e'p) reaction can be written as [39, 40, 41].

$$\frac{d^6\sigma}{dE'd\omega d\Omega_e d\Omega_p} = \frac{p_p E_p}{(2\pi)^3}\frac{E'}{E}\frac{\alpha^2}{Q^4}\eta_{\mu\nu}W^{\mu\nu} \tag{2.15}$$

Where $d\Omega_e$ and $d\Omega_e$ are the electron and proton solid angles in the laboratory coordinate system, and $\eta_{\mu\nu}$ and $W^{\mu\nu}$ are the electron and nuclear response tensors, respectively, E' and E are the energies of scattered and incident electron, and E_p is the energy of the ejected proton. The nuclear response function is written as the product of the matrix elements of averaged electromagnetic four-current density, which is given by

$$W^{\mu\nu} = \langle J^\mu J^\nu \rangle, \tag{2.16}$$

where $J^\mu = (\rho, \vec{J})$ is the four-nuclear current operator, and the angle bracket denotes the product of matrix elements averaged over initial states and summed over final states. The electron response tensor can be expressed as,

$$\eta_{\mu\nu} = K_\mu K_\nu - q_\mu q_\nu - Q^2 g_{\nu\mu}, \tag{2.17}$$

where $K_\mu = k_\mu + k'_\mu$ and $q_\mu = k_\mu - k'_\mu$. Nuclear electromagnetic current conservation

requires

$$q_\mu W^{\mu\nu} = W^{\mu\nu} q_\nu = 0. \tag{2.18}$$

The contraction of the electron and nuclear response tensors reduces to the form:

$$\eta_{\mu\nu} W^{\mu\nu} = \langle K \cdot J K \cdot J^+ - Q^2 J \cdot J^+ \rangle. \tag{2.19}$$

If one selects a coordinate system where the z-axis points in the the direction of the momentum transfer, then the z-component of the current density becomes:

$$J_z = \frac{\omega}{q} \hat{\rho}, \tag{2.20}$$

where $\hat{\rho}$ is the charge density operator. After some algebra, one obtains

$$\eta_{\mu\nu} W^{\mu\nu} = 4EE' cos^2 \frac{\theta}{2} [V_L R_L + V_T R_T + V_{LT} R_{LT} \cos\phi + V_{TT} R_{TT} \cos 2\phi], \tag{2.21}$$

where the V_j's are the leptonic kinematic factors, the R_j's are the nuclear response functions, and ϕ is the angle between the deuteron scattering plane and the reaction plane. The kinematic factors are given by:

$$V_L = \frac{Q^2}{q^2}, \tag{2.22}$$

$$V_T = \frac{Q^2}{2q^2} + \tan^2\frac{\theta_e}{2}, \tag{2.23}$$

$$V_{LT} = \frac{Q^2}{q^2}[\frac{Q^2}{q^2} + \tan^2\frac{\theta_e}{2}]^{1/2}, \tag{2.24}$$

$$V_{TT} = \frac{Q^2}{2q^2}. \tag{2.25}$$

The nuclear response functions are expressed in the form of nuclear current tensors

$$R_L = \langle \rho\rho^+ \rangle \tag{2.26}$$

$$R_T = \langle J_{||}J_{||}^+ + J_\perp J_\perp^+ \rangle \tag{2.27}$$

$$R_{LT}cos\phi = -\langle \rho J_{||}^+ + J_{||}\rho^+ \rangle \tag{2.28}$$

$$R_{TT}cos2\phi = \langle J_{||}J_{||}^+ - J_\perp J_\perp^+ \rangle \tag{2.29}$$

where ρ is the charge component of the nuclear current operator, $J_{||}$ is the transverse component of the nuclear current operator in the scattering plane, and $J_\perp$ is the transverse component of the nuclear current operator orthogonal to that plane. Both $J_{||}$ and $J_\perp$ are orthogonal to $\vec{q}$. From Eqns. 2.15 and 2.21, we get

$$\frac{d^6\sigma}{dE'd\omega d\Omega_e d\Omega_p} = \frac{E_p p_p}{(2\pi)^3}\sigma_M[V_L R_L + V_T R_T + V_{LT}R_{LT}\cos\phi + V_{TT}R_{TT}\cos 2\phi], \tag{2.30}$$

where

$$\sigma_M = (\frac{2\alpha E' \cos\frac{\theta_e}{2}}{Q^2})^2 \tag{2.31}$$

is the Mott cross section of electron scattering on an infinitely massive and spinless charged point particle. If as the result of the $(e, e'p)$ reaction only a single discrete state or narrow resonance of the target is excited, one can integrate the sixfold differential cross section given in Eqn. 2.30 over missing energy to obtain the fivefold differential cross section, which is given by:

$$\frac{d^5\sigma}{d\omega d\Omega_e d\Omega_p} = \frac{E_p p_p M_n}{(2\pi)^3 M_d}\sigma_M f_{rec}[V_L R_L + V_T R_T + V_{LT} R_{LT}\cos\phi + V_{TT} R_{TT}\cos 2\phi], \tag{2.32}$$

where

$$f_{rec} = (1 + \frac{2E\sin^2\frac{\theta_e^2}{2}}{M_d})^{-1}, \tag{2.33}$$

is the recoil factor. The longitudinal response function, R_L, arises because of the charge distribution. The transverse component of the response function, R_T, is the incoherent sum of the transverse components of the current density with respect to the virtual photons. The transverse-transverse response function, R_{LT}, is the interference between the two transverse components of the nuclear current density. The longitudinal-transverse response function, R_{TT}, arises due to the interference of the longitudinal current with the transverse component of the nuclear current.

2.3 Plane Wave Impulse Approximation

In the Plane Wave Impulse Approximation (PWIA), the virtual photon emitted by the scattered electron is totally absorbed by the bound proton, which subsequently emerges without further interaction with the residual nucleus. In PWIA approximation, the initial momentum of the proton is equal and opposite to the missing momentum. In PWIA, the reaction cross section can be factorized as:

$$\frac{d^6\sigma}{dE' d\omega d\Omega_e d\Omega_p} = \frac{E_p p_p}{(2\pi)^3}\sigma_{ep} S(E_m, \vec{p}_m) \tag{2.34}$$

where σ_{ep} is the off-shell electron-nucleon cross section and $S(E_{miss}, \vec{p}_m)$ is the spectral function. In PWIA, the spectral function can be interpreted as the probability of finding a nucleon with initial momentum $-\vec{p}_m$ and bounded inside the nucleus with binding energy equal to E_{miss}. For the independent particle model [42], the spectral function can be written as:

$$S(E_{miss}, \vec{p}_{miss}) = \sum_{\alpha} |\psi(p_m)|^2 \delta(E_\alpha - E_{miss}). \tag{2.35}$$

where $|\psi(\ p_m)|^2$ is the momentum distribution of proton, and E_α is the binding energy of the shell α.

2.4 Final State Interaction (FSI)

In PWIA, the outgoing proton carries all the momentum of the virtual photon and it does not further interact with the neutron. However, at a high missing momentum

the relation $\vec{p}_m = -\vec{p}_i$ does not hold any longer because of the rescattering between the proton and neutron after the interaction between the photon and the proton. The maximum re-scattering happens in the transverse direction relative to the momentum transfer, $\vec{q}$. As a consequence, FSI are expected to be reduced for parallel and anti-parallel to kinematics. FSI have been calculated within the generalized eikonal approximation (GEA) and diagrammatic approach of Laget.(see 1.4).

2.5 Meson Exchange Current and Isobar Configuration

At high Q^2, the contributions of Meson Exchange Currents(MEC) and Isobar Configurations (IC) to the $D(e, e'p)n$ cross section are expected to be small. At high Q^2, the calculation of MEC and IC is very difficult because the virtuality of the exchanged mesons exceeds their masses [9]. However, it is possible to estimate the Q^2 dependence of the MEC and IC contributions from the corresponding Feynman diagrams. The MEC and IC effects decrease with increasing Q^2. This suppression arises from the following two major factors:

- When the knocked-out proton is fast, and carries almost the entire momentum of the virtual photon $\vec{q}$, then the exchanged meson propagator is proportional to $(1+Q^2/m^2_{meson})^{-1}$, where $m_{meson} \approx 0.17$ (GeV/c)^2 is the mass of the exchanged meson.

- An additional Q^2 dependence comes from the NN-meson form factor,$(1+Q^2/\Lambda^2)^{-1}$, where $\Lambda^2 = 0.8$ - 1 GeV ^{2}.

Therefore, one expects that MEC contributions will be suppressed as soon as $Q^2 \geq m^2_{meson}$ and Λ^2 =1 GeV^2.

Chapter 3

Experimental Setup

Data have been taken with electron beam energies of 2.83 , 4.7 and 5.0 GeV for a set of fixed four-momentum transfers Q^2 = 0.8, 2.1 and 3.5 GeV^2, respectively. The data at Q^2 = 0.8 and 2.1 GeV^2 were taken in May and June of 2002, while data at Q^2 = 3.5 GeV^2 were taken in October and September of 2002. The Hall A cryogenic target system provided a 15 cm long liquid deuterium target capable of handling beam currents ranging from 1 to 100 μA. The scattered electrons and out-going protons were detected by the two 4 GeV/c High Resolution Spectrometers (HRSs). In chapter 3, an overview of the instrumentation employed in E01020 will be described. A detailed description of the Hall A instrumentation cab be found in [7].

3.1 Linear Accelerator

The continuous electron beam accelerator facility (CEBAF) at Jefferson Lab was designed to accelerate electrons up to 6 GeV by recirculating the beam up to five times through two superconducting linear accelerators (LINAC), each producing an energy gain of 600 MeV per pass. The primary goal of the CEBAF at Jefferson Lab was to study the structure of nuclei and hadrons, and the fundamental nuclear interactions in the region below the high-energy "asymptotically free", regime [7].

The schematic layout of the accelerator is shown in Fig. 3.1. The electron beam

is produced at the injector by illuminating a GaAs photocathode. They are then injected into the north linac, a 600 MeV linac. The electrons are accelerated by the electric field of 1497 MHz microwaves injected into superconducting niobium cavities. The cavities are kept at a temperature of about 2^0 K by circulating super-fluid ^4He on their outside surface. As a consequence of their superconducting state, the cavities transfer the almost all the microwave power into the beam. Because of their small mass (0.5MeV), electrons quickly gain a velocity close to the speed of light (3×10^8 m/s), and are accelerated together as beam bunches. The distance between the moving electron beam packets is $\frac{3\times10^8}{1497} = 20cm$, which is equal to the longitudinal period of the cavity shape. The length of each electron packet is about 0.5 mm. Electron beam of different energies and intensities can be delivered simultaneously to each of the three experimental halls: A, B, and C.

3.2 Beam Energy Measurement

The accurate and precise measurement of the beam energy is crucial to determine the (e, e'p) cross section. In Hall A, the absolute beam energy is measured by two independent methods: the arc method and the eP method.

3.2.1 Arc Measurement

The arc measurement method is carried out in the arc section of the beam line and is performed by deflecting the electron beam in a constant magnetic field. The nominal bending angle of the beam in the arc section is 34.3^0. The momentum of the beam,

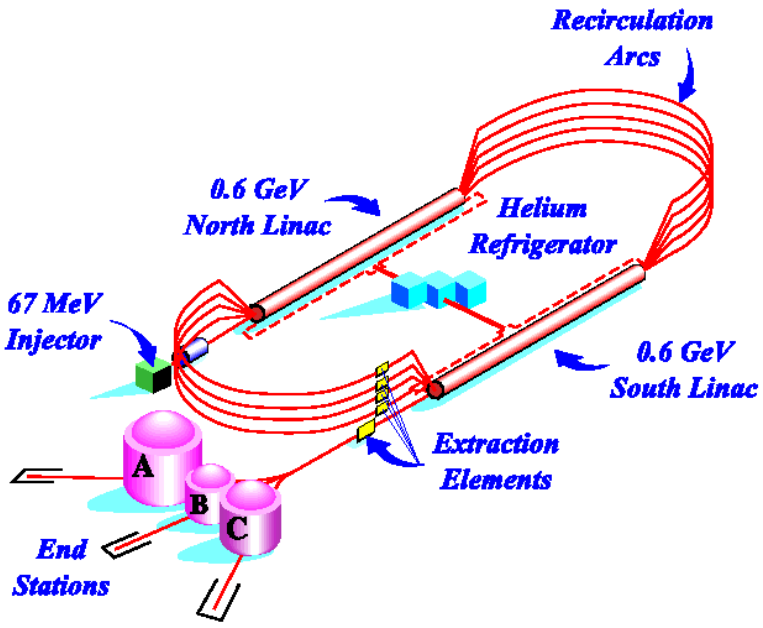

Figure 3.1: The Electron Beam Accelerator

p, is related to the field integral of the dipole, $\oint \vec{B} \cdot \vec{dl}$ and the bend angle of the arc section, θ, by

$$p = k \frac{\oint \vec{B} \cdot \vec{dl}}{\theta}. \tag{3.1}$$

where $k = 0.299792 GeV rad T^{-}1 m^{-}1/c$.

3.2.2 eP Measurement

In the eP measurement method, the beam energy is determined from the kinematics of elastic scattered of the electron beam by a hydrogen target. By measuring the

scattered electron angle, θ_e, and the recoil proton angle, θ_p in the $^1H(e,e'p)$ elastic reaction, the beam energy is calculated from the following relation:

$$E = M_p \frac{cos(\theta_e) + sin(\theta_e)/tan(\theta_p) - 1}{1 - cos(\theta_p)} + O(m_e^2/E'^2). \tag{3.2}$$

Where M_p is the proton mass, and m_e and E' are the mass and energy of the scattered electron, respectively. The higher order terms $O(m_e^2/E'^2)$ are very small at high E' and are neglected. This method employs two sets of silicon micro-strip detectors placed symmetrically with respect to the beam direction. The energies of the scattered particles measured in the respective detectors are expressed in terms of the electron and proton angles with respect to the beam direction.

Both methods of measurement of the beam energy in general show good agreement with each other within a relative uncertainty of $\frac{\delta E}{E} \leq 3 \times 10^{-4}$ [7]. In the present work, the beam energy measured from the arc method was used. The beam energy determined with the eP method indicated problems with an unacceptable shift in the physics analysis results. In addition, arc measurements gave a better agreement in the missing energy than the eP measurements.

3.3 Beam Position Monitors

The position and direction of the beam at the target were measured by two Beam Position Monitors (BPMs) located at distances of 7.524 m and 1.286 m upstream from the nominal target center. Each BPM has a cavity with four antennae, each oriented parallel to the nominal beam direction as shown in Fig. 3.2. The electron

beam passing through the cavity induces signals in the antennae, with an amplitude inversely proportional to the distance between the beam and each of the antennae. The signals from the BPMs antennae are recorded in the CODA data stream on an event by event basis. The Analog-to-Digital Converter (ADC) values from antennae pair are combined with calibration constants to determine the beam position in each of the two directions. During the data taking for $Q^2 = 0.8$ and 2.1 $(\mathrm{GeV/c})^2$, the BPM ADCs were operated in "burst mode" [43]. In burst mode, the beam position in the two BPMs is read out four times per trigger, with a time interval of $4\mu s$. This allows one to precisely track the motion of the beam while registering each event. The beam positions measured in the BPMs coordinate system are converted to the Hall A coordinate system during event reconstruction.

3.4 Beam Current Monitors

The beam current at Hall A is measured by two identical Beam Current Monitors (BCMs), a stainless steel cylindrical cavity of 15.48cm in diameter and 15.24 cm in length, with the cylinder axis coinciding with the nominal beam direction, and both approximately located 25 m upstream from the target center. The BCM consists of an Unser monitor, two Radio Frequency (RF) cavities and a data-acquisition system. The cavities and the Unser Monitor are enclosed in a temperature stabilized box which is also used for magnetic shielding. In each RF cavity, there are two loop antennae, one of which provides an output signal proportional to the beam current. The RF output signal is amplified, and split into two parts. One part of the amplified output is sent to a high-precision digital AC voltmeter that provides, once every second, a

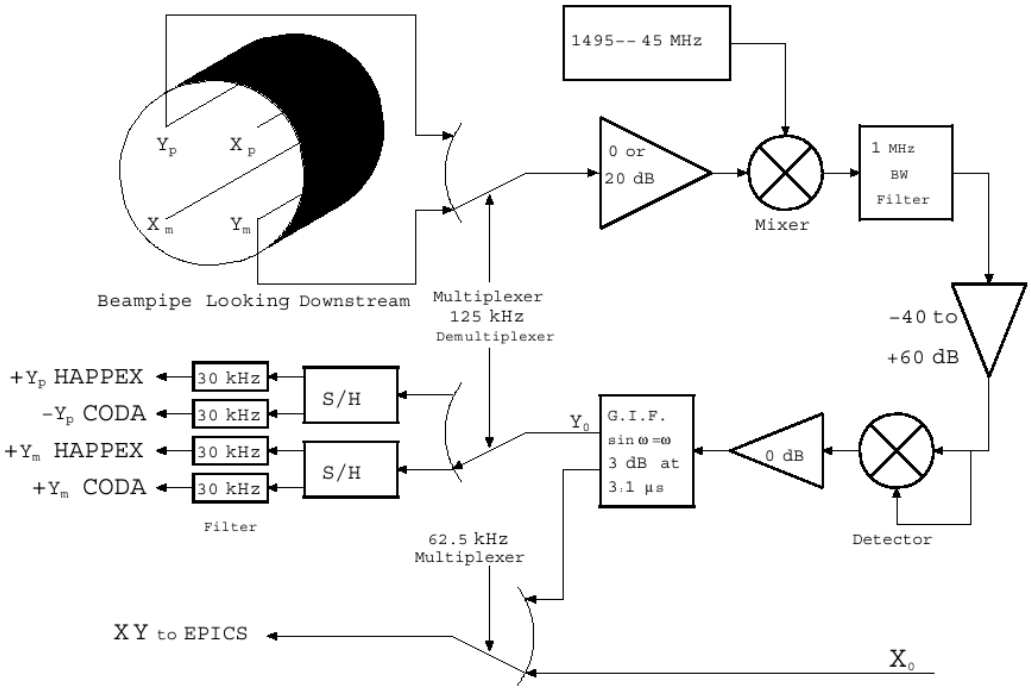

Figure 3.2: The Electronic Set up of the Beam Position Monitor [6].

digital output that represents the RMS of the signal during that second. The other part of the signal is converted by DC converter into an analog DC voltage level. The DC voltage level is then converted to a frequency signal by a V-to-F converter. This output signal is then sent to scalers, the output of which provides the beam charge accumulated during the runs.

3.5 High Resolution Spectrometers

Two high-resolution spectrometers (HRSs) were designed to determine the four-momenta of particles emerging from the target. The schematic side view of Hall A with one of the HRSs is shown in Fig. 3.3. The QQDQ, where Q is a Quadrupole and D is a Dipole magnet, configuration is used in each spectrometer to deflect the

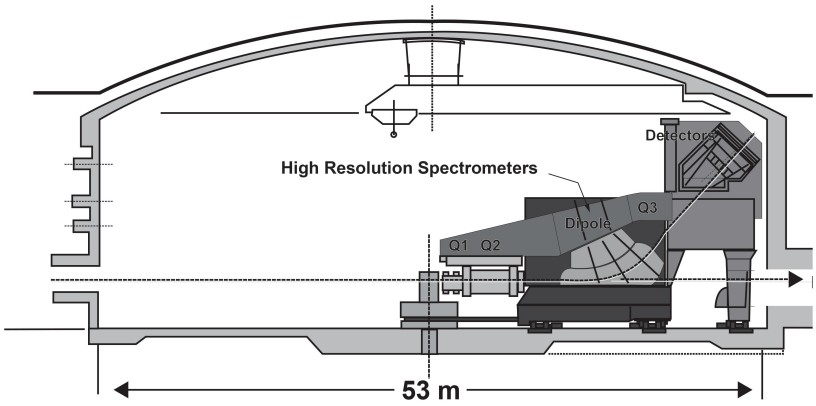

Figure 3.3: Schematic side view of the Jefferson Lab Hall A, and one of the Spectrometers [7].

charged particles from scattering planes into their focal planes. The two quadruples, along with dipole magnet, are designed to achieve the desired momentum and angular resolution with a minimum bending angle.

Each of the spectrometers is operated in either polarity with a central momentum range of 0.3 - 4 GeV/c. The optical length of the spectrometer is 23.4 m, and the nominal bending angle of the central ray is about 45^0. The scattering angle of the measured particles can be changed through the rotation of either spectrometer around the hall center. The nominal angular acceptance of each spectrometer is ± 30 mrad in the horizontal direction, ± 60 mrad in the vertical. The central momentum acceptance is $\delta p/p = \pm 4.5\%$, and ± 5 cm in the target length acceptance. The spectrometer located on the lelft side of the nominal beam direction was labeled as LHRS, and was used to detect scattered electrons. The other was labeled as RHRS, and was used to detect the protons.

Each spectrometer contains a set of collimators, positioned about 1 m from the center of the target. Mainly three types of collimators were used in the experiment: open, 6 *msr* and sieve.

- The open collimator was used for production data.
- The 6 *msr* collimator was used for acceptance studies.
- The sieve slit collimator was used for optics studies.

A more detailed description of the collimator system is found in [7].

3.6 Detectors

The dectors employed in the experiment were used to measure the position and direction of the scattered electrons and the knocked out protons. Moreover, they were also used to separate protons and electrons from other particles with same charge such as pions. The detector package of both spectrometers consisted of two scintillator planes and two vertical drift chambers. The Gas Cerenkov detector placed in the left spectrometer was used for the separation of electrons from negative pions. The aerogel Cerenkov detector of the right arm and the electromagnetic calorimeter in left arm were not used in the final analysis. Auxiliary triggers were generated by the S_0 scintillator paddle, and used for the measurement of the efficiency of main trigger types. Fig. 3.4 shows the detector package for the LHRS and RHRS.

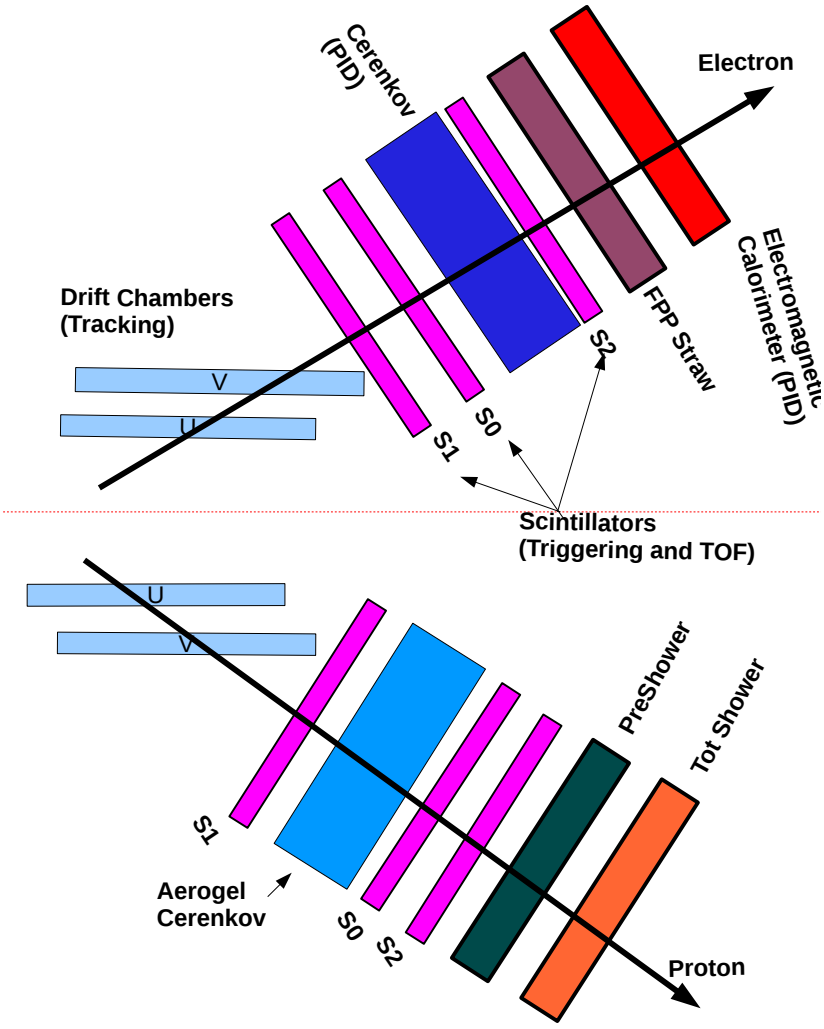

Figure 3.4: Detectors for left and right spectrometer

3.6.1 Scintillators

In each spectrometer two scintillator planes, known as S_1 and S_2, were installed at distances of 1.5m and 3.5m respectively, downstream of the center of the first vertical drift chamber (VDC) as shown in Fig. 3.4. Each scintillator plane was segmented into 6 paddles with a 0.5cm overlap. The total active area of S_1 was $170cm \times 35cm$, while the active area of S_2 was $220cm \times 54cm$. Each end of a paddle was connected to photomultiplier tubes (PMTs) for detecting the scintillation light. These scintillators play a crucial role in obtaining timing information necessary to determine the time of flight (TOF) of particles in each spectrometers as well as the coincidence time for the (e, e'p) reaction products.

3.6.2 Vertical Drift Chambers

Tracking information in each spectrometer is provided by a pair of VDCs. The detailed description of the VDCs can be found in [8]. Each VDC is composed of two wire planes in a standard UV configuration. The wires of each planes are oriented at 90° to one another. The wires are inclined at an angle of 45° with respect to the dispersive and non-dispersive directions. Each wire plane is sandwiched between two high voltage(HV) planes. The HV plane is separated from the wire plane by 13mm. The first and last 16 wires on each wire plane are grounded to shape the electric field. The remaining 368 wires are all 20 μm diameter signal wires made of tungsten coated with gold. A mixture of Argon 50% and Ethane 50% by volume was supplied between

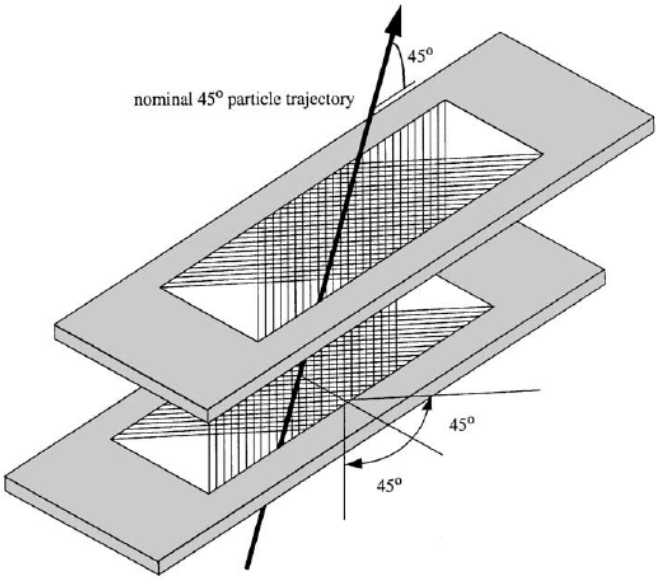

Figure 3.5: The Systematics diagram of the VDC and the nominal direction of the particle trajectory with respect to the plane of the wire[8]

the two HV planes of each wire plane independently. During operation, each wire plane is grounded, and HV planes are kept at negative potential of -4kV. A charged particle crossing a VDC ionizes atoms in the gas mixture which creates a trace of released electrons. The released electrons are then accelerated by an electric field due to the high potential difference between wire planes and HV planes. The electrons drift towards the signal wires where they create avalanches. The electron avalanche induces a signal on a wire , which is then amplified , discriminated and sent to a multihit TDC. The wires provides the TDC start signal and the common stop signals are provided by the trigger. From the drift time information in the TDCs, the track of the charged particles through the VDC's can be determined.

3.6.3 Gas Cherenkov

In the LHRS, a gas Cherenkov detector was placed between two S_1 and S_2 scintillator planes. It was filled with CO_2 gas at atmospheric pressure. A charged particle traversing through the chamber with a velocity greater than (1/n), where n is the refractive index of the gas mixture, produces Cherenkov radiation. Ten spherical mirrors located at the chamber wall focus the Cherenkov light to ten corresponding PMT photocathods. The Cherenkov radiation thresholds for negative pions (π^-) and electrons in CO_2 at atmospheric pressure are 4.8 GeV/c and 17MeV/c respectively. Therefore the gas Cherenkov detector allows the separation of electrons from π^- in the electron spectrometer as the largest momentum that can be detected by the LHRS is 4 GeV/c. The maximum momentum for the LHRS is therefore less than the Cherenkov threshold momentum of the pion. However, pions could produce Cherenkov signals through the production of knock-on electrons. Fig. 3.6 shows the distribution of the sum of the ADC values of all ten PMTs (ADC sum) corrected for pedestals and gain. The red line indicates the cut applied to separate the ADC sum of scattered electron, and that of knock-on electrons.

3.7 Target

During the experiment, liquid cyrogenic and solid targets were used. The cyrogenic target system mounted inside the standard scattering vacuum chamber consisted of independent target loops for liquid hydrogen(LH2), liquid deuterium (LD2) and helium ^4He. Each of the three target loops has two cylindrical aluminum target cells,

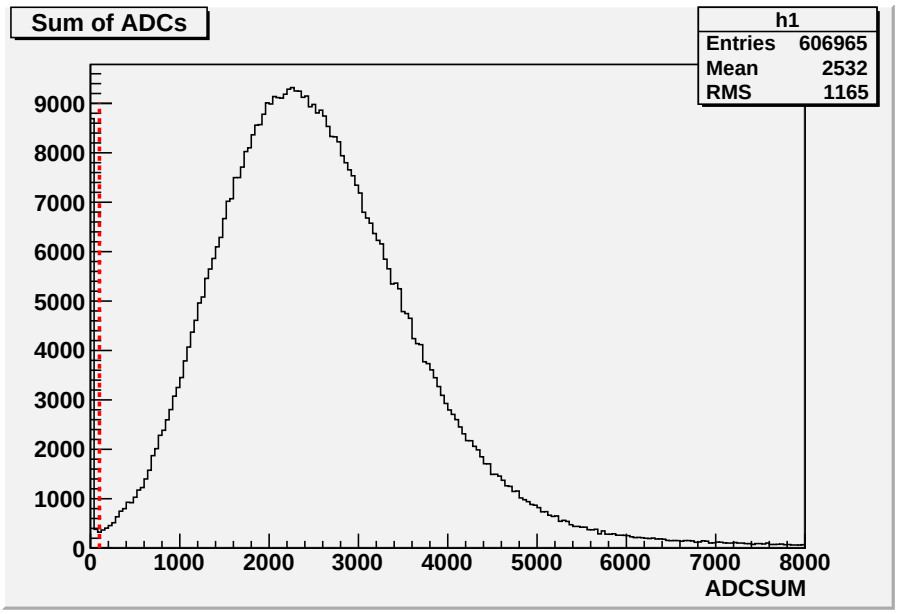

Figure 3.6: The distribution of the sum of the corrected ADCs. $ADCSUM > 100$ is the sum of ADC values obtained due to the Cerenkov radiation of electron.

4 cm and 15 cm long, with their axes along the nominal direction of the beam as shown in Fig. 3.7. The nominal diameter of each cell was 4.066 cm. The loop with liquid ^4He was not operated in experiment. The side walls of the target cells were 178 μm thick, and entrance and exit windows were about 71 μm and 102 μm thick, respectively. Besides the liquid targets, there were other solid targets: a nine-foil carbon target, a thick carbon target, a so-called dummy target, and a beryllium-oxide target (BeO). The nine-foil carbon foil target was normally placed perpendicular to the nominal direction of the beam. It is used to measure the mispointing of the spectrometers and for the optics optimization. The aluminum "dummy" target consists of apair of thin aluminum plates. The dummy targets are normally used for the measurement of the contributions from the wall of the liquid target cell. When the beam is incident on a BeO target, it causes the target to glow brilliantly which provides an optical check

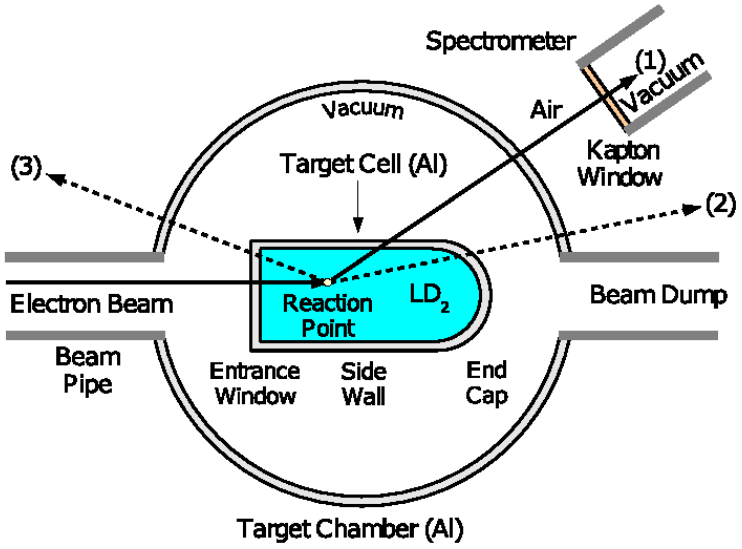

Figure 3.7: Target chamber and Target cell

that beam is present and in the correct position.

3.8 Coordinate Systems

The main coordinate systems used in the Hall A experiments are described below.

3.8.1 Hall Coordinate Systems (HCS)

The origin of the Hall coordinate systems is defined as the point of intersection of the unrastered beam with the plane perpendicular to the beam rotated at the axis of rotation of the target system. A top view of the Hall coordinated system is shown in Fig. 3.8. The z-axis points in the direction of the beam, the y axis is vertically upward and the x -axis is $\vec{x} = \vec{y} \times \vec{z}$. All the kinematic variables are reconstructed in the HCS coordinate system.

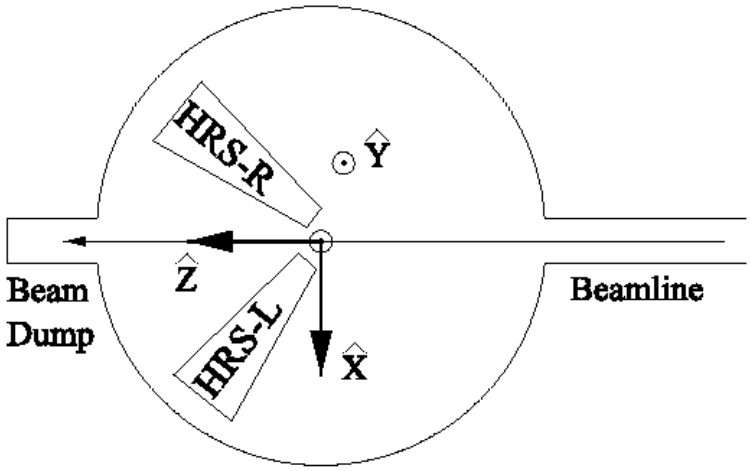

Figure 3.8: Top view of the Hall A Coordinate System

3.8.2 Target Coordinate Systems (TCS)

The Target coordinate systems (TCS) is associated with each spectrometer. The z-axis of the TCS passes through the mid-point of the central sieve slit hole of each spectrometer. The x-axis points downward crossing the center of sieve slit, and the y-axis points in the perpendicular direction of the x-z plane i.e $\vec{y} = \vec{z} \times \vec{x}$ as shown in Fig. 3.9. Ideally, the origin of the TCS should coincide with the origin of the HCS. In the TCS, the out-of-plane angle θ_{tg} and the in-plane angle ϕ_{tg} of the particle trajectory in the target coordinate system are defined as:

$$\tan\theta_{tg} = \frac{dx}{dz} \tag{3.3}$$

$$\tan\phi_{tg} = \frac{dy}{dz} \tag{3.4}$$

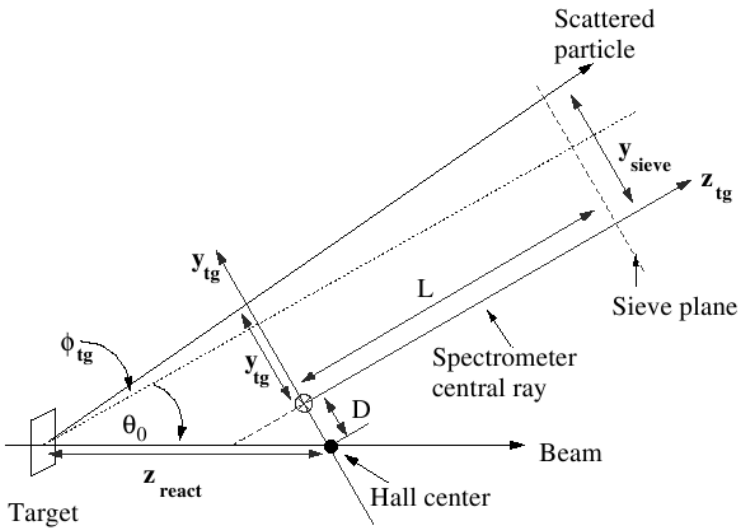

Figure 3.9: Target Coordinate System (TCS)

The relative momentum in the TCS is defined by:

$$\delta_{tg} = \frac{p - p_0}{p_0} \tag{3.5}$$

Where p is the particle momentum and p_0 is the central momentum of the spectrometer.

3.9 Data Acquisition

The experiment used the CEBAF Online Data Acquisition system (CODA). The schematic diagram of the Hall A CODA system is shown in Fig. 3.10. It consists of the following major parts:

The Digitizing System converts analog electronic signals to a proportional number. It's components are installed on the front end crates. The system includes time-to-

digital converters (TDCs), analog-to-digital converters (ADCs) and scalers.

The Read-out Controllers (ROCs) read the digital data after registering a hit from the detectors. The main function of the ROCs is to receive a trigger from the trigger supervisor, execute the correspond readout list, structure the information and pass it to the next CODA components, "the event Builder".

The Trigger Supervisor is that part of the CODA controlled system which links the experiment triggering system and ROCS. It accepts the trigger from different channels, prescaler multiple triggers and maintains the busy system while the trigger is being processed. During the trigger processing time, no additional trigger is accepted until the ROCs finish processing the data, a period of time which is measured and called the CODA dead time.

The Event Builder collects all the ROCs data fragments, and orders and merges the pieces into a CODA data structure, called an event.

The Event Recorder records the events to disc. Each recorded data file starts with a header which contains the run size and run number.

3.10 Trigger Setup

The trigger formation in both spectrometers is very similar, and the coincidence trigger is formed by an AND of the two single spectrometer triggers. Three major triggers were used for the physics analysis in this dissertation, and they are: T_1 (proton spectrometer(RHRS) single trigger), T_3(electron spectrometer(LHRS) single trigger and T_5 (coincidence trigger).

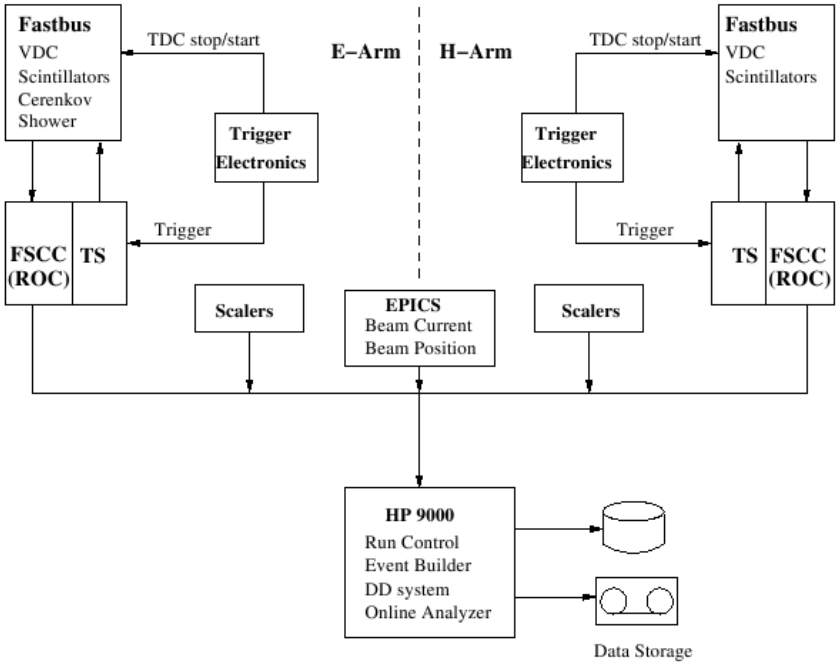

Figure 3.10: Systematic diagram of Hall A CODAQ.

The schematic diagram of the main trigger setup is shown in Fig. 3.11. In each spectrometer, the scintillators were arranged in two planes S_1(lower) and S_2(upper), with six paddles in each plane, and two photomultiplier tubes (PMTs) on either sides of each paddle. Therefore, the scintillator planes provide 2(Scintillators) $\times$ 6(paddles)$\times$ 2 (PMTs) = 24 signals for each spectrometer. $S_1 - L$ and $S_1 - R$ denote the signal from the left and right PMT of the lower scintillator plane. Similarly $S_2 - L$ and $S_2 - R$ correspond to the upper scintillator plane. The analog signals from the two side of each scintillator paddle were sent to a discriminator. The discriminator provides both analog and digitized outputs. The analog signals were sent to ADCs. The digitized signals were split into three parts: the first and second part of the signals were delayed and sent to scalers and TDCs, and the third part was sent to

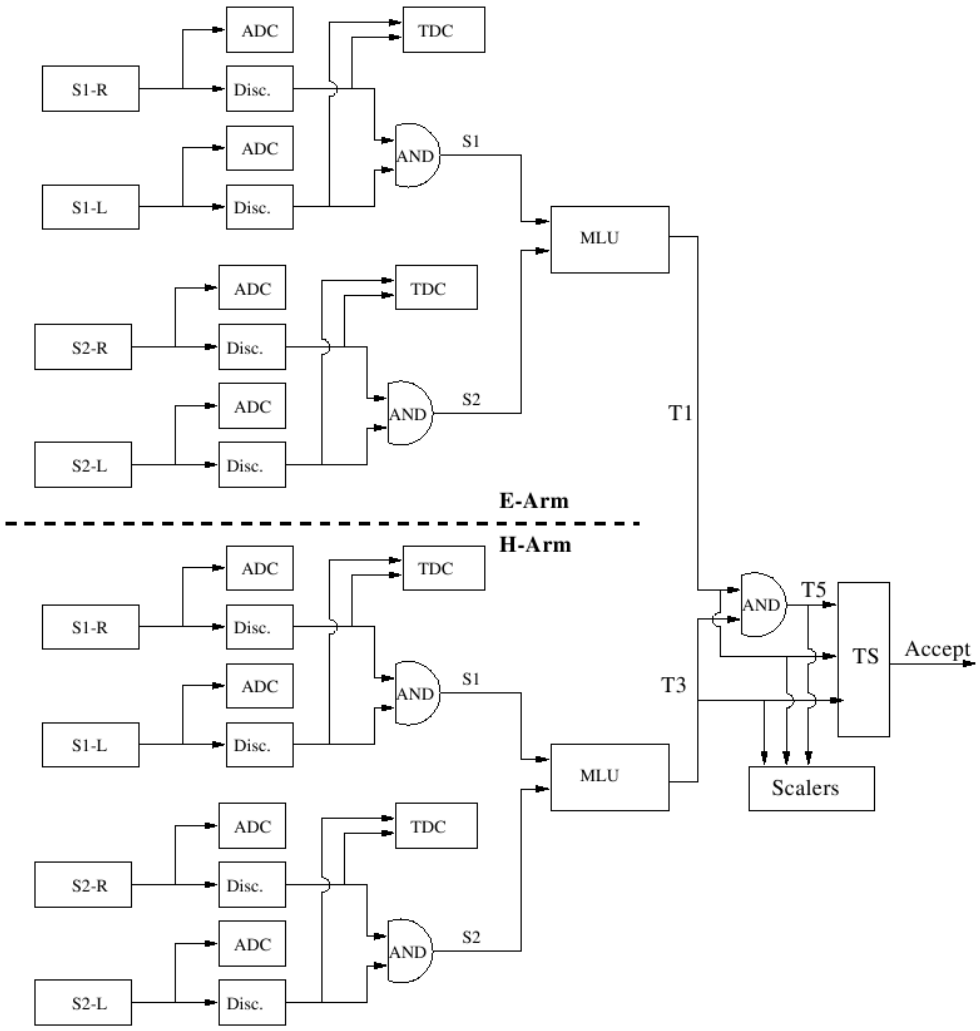

Figure 3.11: Main Trigger Setup for Physics Analysis.

a logical AND unit making a coincidence between pairs of PMT signals viewing the same paddle. Twelve outputs of the logical AND unit for each spectrometer were fed into the Memory Look up Unit (MLU). The MLU is a programmable device that provides the corresponding logical signals at its output. The MLU output from the RHRS was denoted as proton spectrometer signals trigger T_1 and the output from the LHRS was denoted as electron spectrometer signals trigger T_3. The AND of T_1 and T_3 formed the coincidence trigger T_5.

Chapter 4

Calibration and Correction

In the first step of the analysis, raw data from the CODA file have been analyzed using the Hall A standard event reconstruction software ANALYZER. The results from this first analysis step have been used to calibrate the detectors in each spectrometer. In chapter 4, we will describe the details of the various correction and calibration procedures.

4.1 Luminosity Studies

Luminosity studies have been carried out by using the flat carbon target(C12) and the extended liquid deuterium (LD2) target. The observed event rates in the detectors are primarily affected by the:

- beam current
- effective target thickness (target boiling)
- detector efficiency
- computer dead time
- electronic dead time.

These contributions need to be separated and determined individually as much as possible in order to correct the accumulated number of events.

4.1.1 The Carbon Target

We used a thick carbon target with thickness 595.0 gm/cm^2 for the luminosity study to assure that the effective target thickness is not affected by the beam current. This made it possible to study variations of the measured event rate as a result of detector efficiency variations and dead time effects. Coincidence events were selected using the Hall A Trigger Supervisor(TS) pattern, and tracking cuts as described in section 5.7 were applied. The TS patterns for coincidence event types are as follows:

- (TS =16) events without any prescaler signal
- (TS =17) events with a right prescaler signal
- (TS =20) events with a left prescaler signal
- (TS =21) events with prescaler signals present in both spectrometers

The normalized event rates has been defined as :

$$Yield = \frac{N}{Q\epsilon_d T_{lt}} \tag{4.1}$$

where N is number of coincidence events, Q is the accumulated beam charge, ϵ_d is the detector efficiency and T_{lt} the computer live time. The electronic dead time was not measured and assumed to be negligible.

Fig. 4.1 shows the normalized event rate as a function of beam current. The observed fluctuations at different beam currents are found to be less than 2 % and statistical

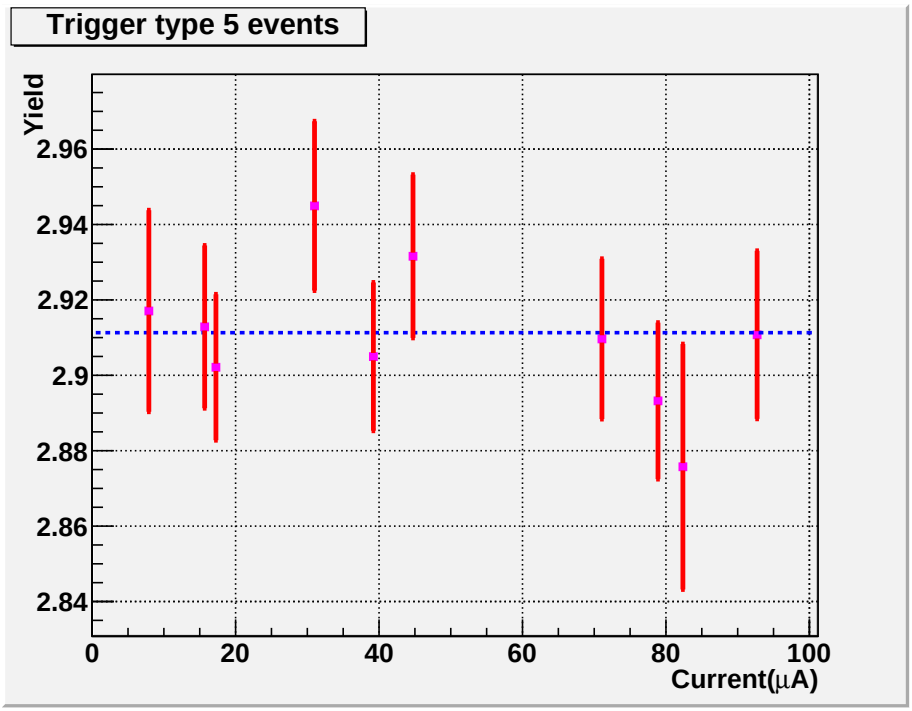

Figure 4.1: Rate of coincidence events with the beam current in the flat carbon target

in nature. This study has been carried out at $Q^2 = 0.8$ GeV ^{2} with an average beam energy of 2.8428 GeV.

4.1.2 Extended Target (Boiling Study)

The boiling study of the extended target refers to the study of the change in the density of the Hall A cryotarget material with beam current. The main reason for the density change is heat transferred from the electron beam to the target material (typically on the order of 600W at 100μA). The power deposited in the target is proportional to the beam current and beam energy loss in the target. The boiling effects were investigated using a 15 cm long and 4.066cm diameter liquid deuterium target cell. During the measurements, the beam was rastered over a 2 $\times$ 2 mm^2

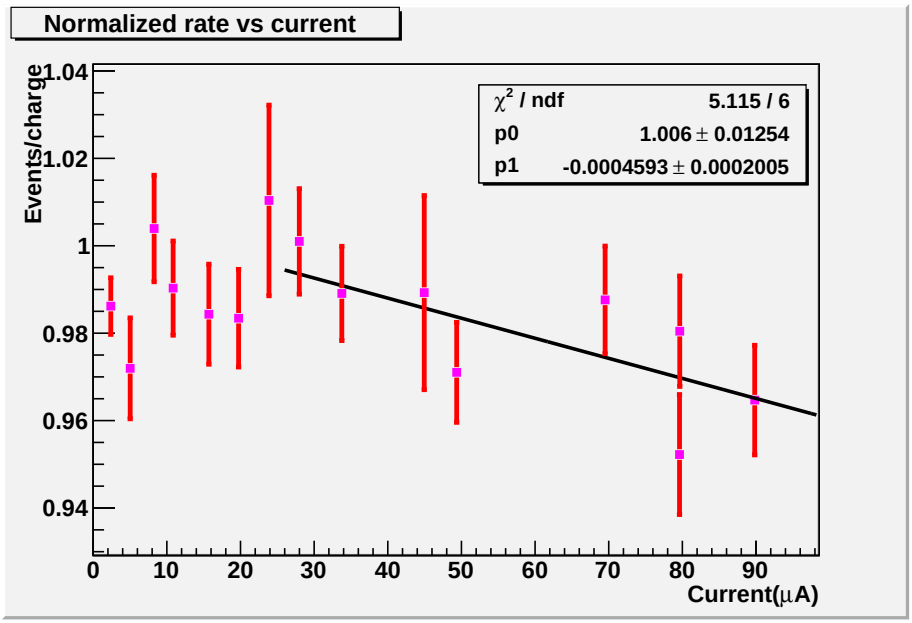

Figure 4.2: Normalized yields as a function of the beam current in deuterium target

spot, and the same raster size was later used for the production data on deuterium. Fig. 4.2 shows the normalized yield of coincidence events as a function of beam current. At low currents ($< 30\mu A$), there is no significant reduction of the target density. The variation of the target density was found to depend on the location of the reaction point along the beam (z_{react}) and on the beam current. For currents $\geq 30\mu A$, the change in density of the liquid deuterium (LD2) with the beam current can be expressed as:

$$\rho(z, I) = \rho_0 \cdot [1 + \alpha \cdot (z - z_0)(I - I_0) \tag{4.2}$$

where ρ_0 is the density of the target below $30\mu A$, $I_0 = 30\mu A$, $z_0 = 0.05m$ and I is the beam current in μA. The value of $\alpha = -0.00173 \pm 0.0034$ has been obtained by fitting the normalized yield.

4.2 Spectrometer Mispointing

The High Resolution Spectrometers(HRS) were rotated around the center of the hall in order to set the different scattering angles for the scattered electron and the knocked out proton. Reading the the same angular location at different times lead to small misalignments for each spectrometer. These movements were not reproducible. The mispointing of the spectrometer lead to a horizontal displacement of the origin of the Target Coordinate System (TCS) with respect to the origin of the Hall Coordinate System(HCS). In an ideal situation, the origin of the TCS should coincide with the origin of the HCS. As shown in Fig. 4.3, the vector $\vec{r}_{sp}$, where $|r_{sp}| = h_0$, denotes the mispointing. In order to determine and correct for this mispointing the data from the nine foils carbon target and survey results of the HRS were used. In the nine foils carbon target, the position of the central foil measured from either spectrometer provides the displacement of the origin of the TCS with respect to the HCS. The components of the horizontal displacement vector along x and z axis in HCS are denoted by x_0 and z_0 respectively.

The beam x-position, x_{beam}, the spectrometer central angle, θ_0, which is positive for the left arm and negative for the right arm, the target z-position as given in the survey, and reconstructed target variables y_{tg} and ϕ_{tg} are used to calculate the spectrometer horizontal displacement, h_0. The intersection between the trajectory of the incoming electron beam and the trajectory of the scattered particles, as shown Fig. 4.3, determines the reaction vertex. The trajectory of the beam along the x-axis

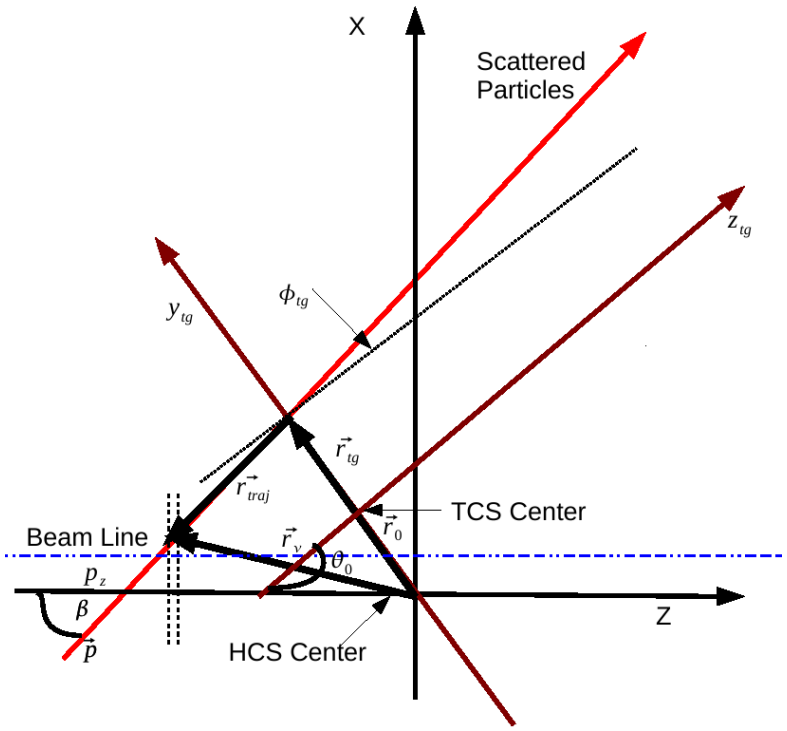

Figure 4.3: Mispointing calculation.

in the HCS is given by:

$$x_{beam} = x_{ob} + ztan\theta_{beam} \tag{4.3}$$

where x_{ob} is the point of intersection of the beam with the x-axis of the HCS, and θ_{beam} is the angle made by the electron with respect to the z-axis in the HCS. The trajectory of the scattered particles in HCS is given by:

$$x_{sc} = x_{os} + ztan\beta \tag{4.4}$$

where x_{os} is the point of intersection of the scattered particles with the x-axis in the HCS and β is the angle made by the scattered particles with the z-axis in the HCS.

At the vertex, one can write,

$$x_{sc} = x_{beam}. \tag{4.5}$$

Referring to Fig. 4.3, the vector equation can be written as:

$$\vec{r}_o + \vec{r}_{tg} + \alpha \hat{r}_{traj} = \vec{r}_v \tag{4.6}$$

where:

$$\vec{r}_o = \begin{pmatrix} x_0 \\ \\ z_0 \end{pmatrix} = \begin{pmatrix} h_0 cos\theta_0 \\ \\ -h_0 sin\theta_0 \end{pmatrix} \tag{4.7}$$

$$\vec{r}_{tg} = \begin{pmatrix} -y_{tg} sin\theta_0 \\ \\ -y_{tg} cos\theta_0 \end{pmatrix} \tag{4.8}$$

$$\vec{r}_v = \begin{pmatrix} -z_{tg} \\ \\ x_{tg} \end{pmatrix} \tag{4.9}$$

$$\hat{r}_{traj} = \begin{pmatrix} cos(\theta_0 + \phi_{tg}) \\ \\ sin(\theta_0 + \phi_{tg})) \end{pmatrix} = \begin{pmatrix} cos\beta \\ \\ sin\beta \end{pmatrix} \tag{4.10}$$

and α is the distance between the vertex and the intersection of the scattered particle trajectory with the y_{tg}-axis in the TCS. Solving Eqn. 4.6 for h_0, one gets:

$$h_0 = -y_{tg} + \frac{x_{beam} cos\beta - z_{tg} sin\beta}{cos\phi_{tg}} \tag{4.11}$$

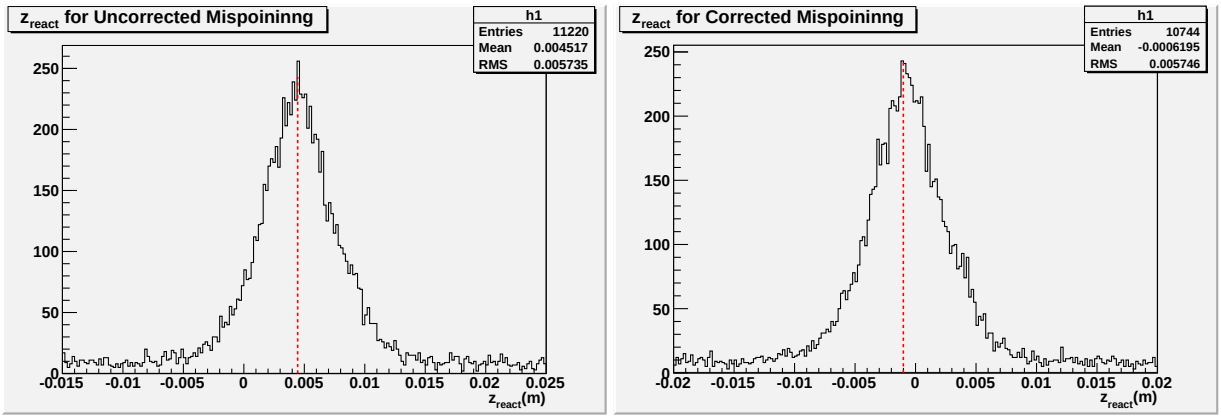

Figure 4.4: z position of the reaction vertex before and after the mispointing correction

Substituting the value of h_0 in Eqn. 4.7, the components of the offset along the x and z-axis in the HCS can be obtained. The offsets for the different kinematic settings were determined and stored in the run data base. Afterwards the ANALYZER was run again using the new modified data base. The reconstructed reaction point, z_{ract}, along the z-axis then agreed with the target position z_{tg} in the HCS, as determined from the survey. The survey result of the horizontal offset along the z-axis due to mispointing, -1.01mm, was reproduced from the calculation using Eqn. 4.11. Fig. 4.4 shows the position of the z-vertex before and after the mispointing correction. The position of the peak of the z_{ract} distribution after the correction agrees with the survey result, -1.01mm.

4.3 Computer and Electronic Dead Time

Computer dead time refers to the time when events are not being recorded because the data acquisition (DAQ) system is busy with processing the previous events. The complementary of the dead time, the computer live time (LT) was calculated from

Table 4.1: The Set of Trigger for the Experiment E01020. N/A means not applicable

Trigger Type	Event Type	Scalers	Comments
Input Trigger	N/A	S_1	RHRS fires
	N/A	S_3	LHRS fires
	N/A	S_5	LHRS and RHRS fire
Output Trigger	1	T_1	RHRS fires
	3	T_3	LHRS fires
	5	T_5	LHRS and RHRS fire

the number of raw triggers that were counted by scalers, and the number of accepted triggers that were processed by Trigger Supervisor (TS) i.e

$$LT = \frac{N^{rec}}{N^{cout}} \tag{4.12}$$

where N^{rec} is the number of events recorded, and N^{count} is the number of raw triggers counted. The LT depends on the pre-scaler factors of the trigger and total rates recorded by DAQ.

Electronic dead time is due to the non-zero time width (τ), or pulse width of logical pulse passed into the scaler. If two independent pulses arrive at the scalers within a time interval shorter than τ, then only one pulse will be recorded. The coincidence events rate was less than 2 kHz, so this effect was below 1 percent and was neglected. Here we only considered the computer dead time.

The raw triggers are denoted by S_i, where $i = 1, 3, 5$, while accepted triggers are denoted by T_i. The patterns of the input and output triggers are shown in the Table 4.1.

In this analysis, we only calculated the dead time of coincidence events (type 5 events). The total number of pure coincidence events after dead time correction can be written as:

$$N_{coin} = \frac{S_5}{T_5} N_{e,e'p} \tag{4.13}$$

Where $N_{e,e'}$ is the number of (e, e'p) events written in tape as type 5 events. The computer dead time for coincidence events is written as:

$$DT_{coin} = 1 - LT_{coin} \tag{4.14}$$

Where

$$LT_{coin} = \frac{N_{e,e'p}}{N_{coin}} = \frac{T_5}{S_5} \tag{4.15}$$

Fig. 4.5 shows the computer LT of coincidence events at $Q^2 = 0.8$, and $Q^2 = 2.1$ (GeV/c)^2 for different runs. At high $Q^2 = 2.1$ (GeV/c)^2, LT looks stable at around 95 %. At $Q^2 = 0.8$ (GeV/c) ^{2}, the events rate is higher at high run numbers. Therefore, at the higher events rates, LT is lowered.

4.4 Detector Efficiency

4.4.1 Trigger Efficiency

The Scintillator inefficiency arises because of the following:

- Statistical fluctuation of the energy deposited by the charged particles in the scintillator paddles.

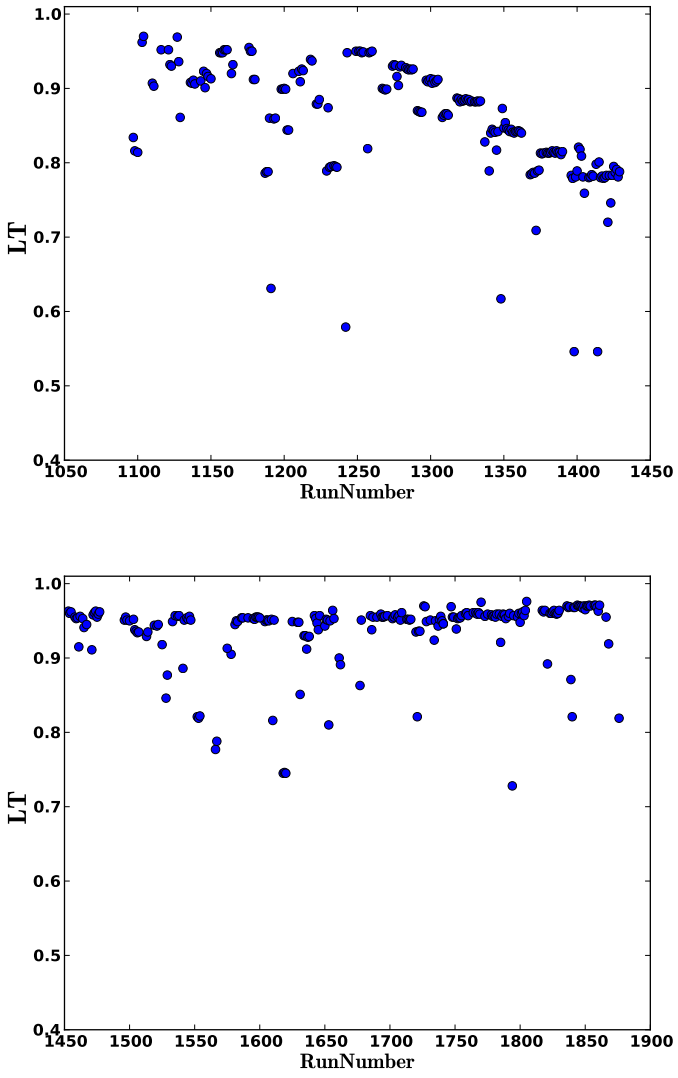

Figure 4.5: Computer Live time of type 5 events at (a) $Q^2 = 0.8$ and (b) $Q^2 = 2.1 GeV^2$ at different run periods.

- Imperfect transmission of the light emitted by the particle in the scintillator paddles to the Photo Multiplier Tubes (PMTs).

- Inefficiency of PMTs.

Most of the events missed by the main physics trigger types 1, 3 and 5 because of the trigger inefficiency are recorded as type 4 trigger (T_4) events in the electron arm and type 2 trigger (T_2) events in the proton arms. The trigger types T_2 and T_4 are useful to calculate the trigger efficiency. To determine the trigger efficiency, good VDC tracking is required, and the electrons are separated from negative pions using a particle identification (PID) cut on the Gas Cerenkov ADC sum signals($SUMADC > 80$). The trigger efficiencies ϵ_e and ϵ_p for the detection of electrons and protons can be calculated from the number of trigger type events, N_i, where $i = 1, ..., 5$ are the trigger types.

$$\epsilon_p = \frac{N_1 + N_5}{N_1 + N_5 + N_2} \tag{4.16}$$

$$\epsilon_e = \frac{N_3 + N_5}{N_3 + N_5 + N_4} \tag{4.17}$$

Fig. 4.6 shows the trigger efficiency of coincidence events at $Q^2 = 0.8$ and $Q^2 = 2.1$ (GeV/c)^2 at different kinematic runs. In both Q^2, we got around 99 % trigger efficiency.

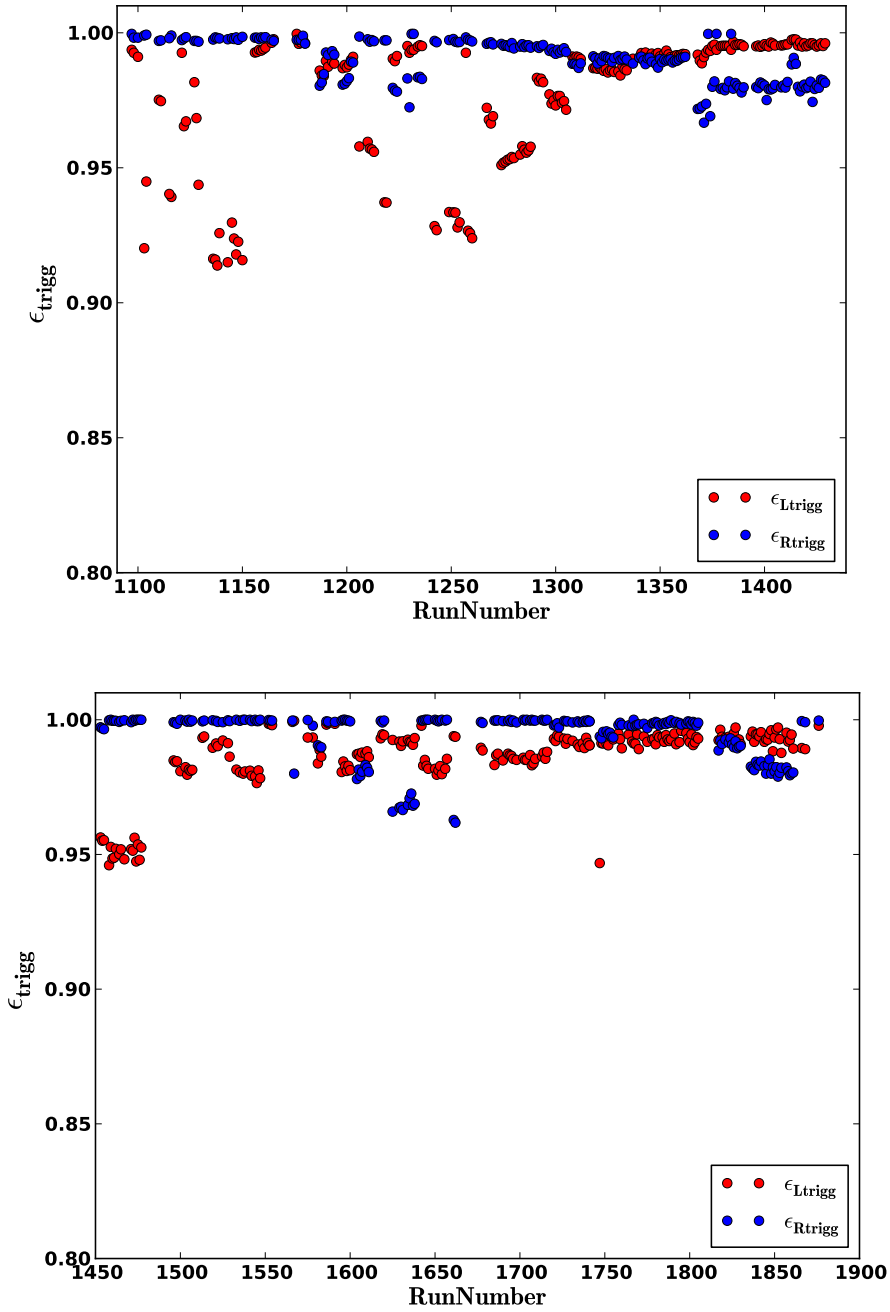

Figure 4.6: Trigger efficiency of type 5 events at (a) $Q^2 = 0.8$, and (b) $Q^2 = 2.1$ (GeV/c)^2, red: trigger efficiency for left spectrometer and blue: trigger efficiency for right

4.4.2 VDC Efficiency

The VDC efficiency is the probability that the VDC wire fires when a charged particle passes through the chamber. A small fraction of events have zero hits, and many events form multiple disjointed hits in the VDCs. For the VDCs, one minimum assumption was considered: any real particle traversing the VDC should produce three or more consecutive hits on each of the four wire planes. The number of wires hit is called multiplicity. A cut on multiplicity was applied in all four wire planes of each spectrometer. In this analysis, events with a multiplicity between 3 and 20 in each of the four wire planes were accepted. The VDC efficiency was calculated by counting events that fired all four VDC planes, and events that did not fire one of the planes. If N_0 is the number of events that fired all four VDC planes (u_1, u_2, v_1, v_2), and N_{u1} is the number of events which fired only the three VDC planes (u_2, v_1, v_2) but not u_1, then the efficiency of the u_1 plane is written as:

$$\epsilon_{u1} = \frac{N_0}{N_{u1}}. \tag{4.18}$$

By applying this method to the other planes, we can calculate the efficiency of all four VDC wire planes. Therefore, one can write the total VDC efficiency as:

$$\epsilon_{vdc} = \epsilon_{u1} \times \epsilon_{u2} \times \epsilon_{v1} \times \epsilon_{v2} \tag{4.19}$$

In both spectrometers, we got around 99 % VDC efficiency.

4.4.3 Tracking Efficiency

The basic assumptions to calculate the tracking efficiency are:

- All the events should fire all four VDC planes of each spectrometer.
- The multiplicity of the events should be between 3 and 20.

The tracking efficiency is defined as the probability of getting an event with a single track in the events with at least one track. The tracking efficiency is given by:

$$\epsilon_{track} = \frac{N_{1trac}}{N_{track>=1}} \tag{4.20}$$

where N_{1trac} is the number of events with one track only and $N_{track} >= 1$ is the total number of events with at least one track. The magnitude of the tracking efficiency ϵ_{track} varied between kinematic settings and depended mostly on the total particle rate in the detector. The tracking efficiency of both data sets is above 85 % as shown in Fig. 4.7.

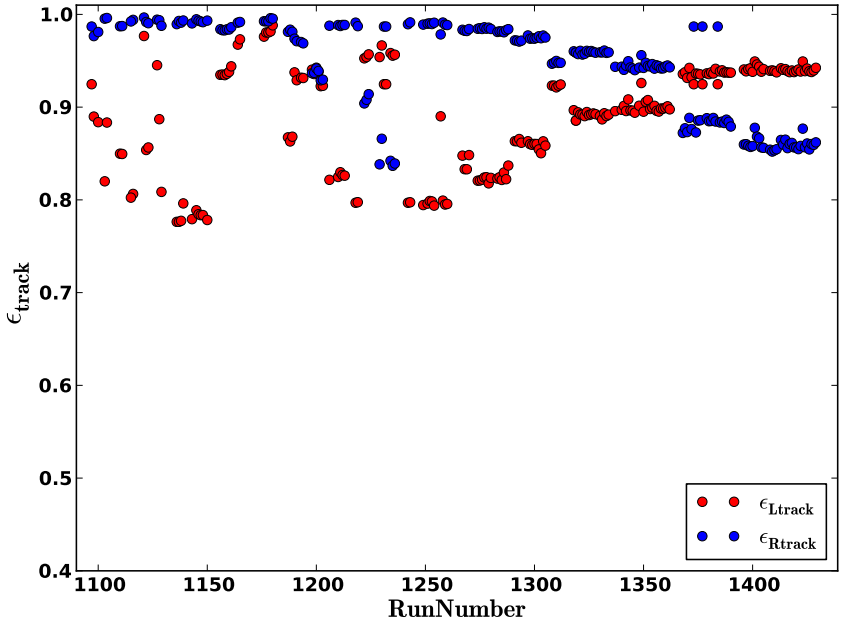

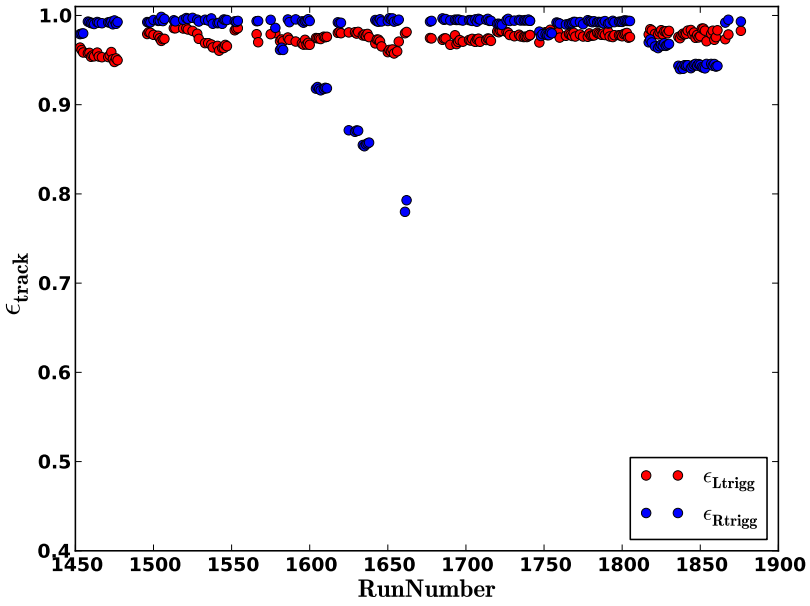

Figure 4.7: Tracking efficiency at (a) $Q^2 = 0.8$ and (b) $Q^2 = 2.1 GeV^2$, red: tracking efficiency for left spectrometer and blue: tracking efficiency for right.

Chapter 5

Data Analysis

In this chapter, the major parts of the analysis including the methods of optimization, correction of the spectrometers, Monte Carlo simulations, normalizing procedures and applied cuts in order to select the good events will be discussed.

5.1 Optimization Time of Flight

During the experiment, two scintillator planes known as S1 and S2 were installed in each spectrometer in order to calculate the time of flight (TOF) of the scattered electrons and protons. The scattered electrons were detected in the Left High Resolution Spectrometer(LHRS) while protons were detected in Right High Resolution Spectrometer (RHRS). In each HRS, the time reference was defined by one of the paddles in the S_2 scintillator plane. This signal was used to start all the spectrometer's TDCs. In order to optimize the time of flight, various factors were taken into account such as the corrections for path length difference(differences trajectory length of the particle from the center of target to the HRS focal plane) of scattered particles, time walk corrections, scintillator time offset corrections and pedestal corrections. Completion of the TOF optimization consisted of the following two steps:

- determining the TOF correction for each HRS
- determination of correction parameters for the coincidence time.

5.1.1 HRS Single Arm Timing Correction

The timing correction of each HRS consisted of the correction for the time needed the signal to propagate through the cable of each side of the scintillator paddle. Knowing the TOF of the particles between the two scintillator planes, the signal processing time in the paddles and the raw TDC value, one can calculate the time taken by the signal in the signal cable. This is also referred to as the TDC offset. A schematic TOF trajectory of the particle from the i^{th} paddle of $S_1(S_{1i})$ to j^{th} paddle of $S_2(S_{2j})$ is illustrated in Fig. 5.1. For simplification, first we considered the TOF between the first paddle of S_1 (S_{11}) and the first paddle of S_2 (S_{21}). It was then generalized from the i^{th} paddle of S_1 to the j^{th} paddle of S_2, where i and j go from 1 to 6. In each spectrometer, S_{21} provides the start signal while all remaining paddles provide the stop signal. The time difference between the stop signal and the start signal, measured by the TDC refers to the raw TDC value, and is proportional to,

$$TDC = (T)_{stop} - (T)_{start} \tag{5.1}$$

The scattered particle strikes the S_{11} paddle at time t_1. $R_{11p}(L_{11p})$ is the signal propagation time for the scintillator right(left)side paddle, and $R_{11O}(L_{11O})$ is the signal propagation time in the delay cable of the right(left) side paddle. The TDC value measured at the left side of the S_{11} is given by:

$$T_{l11} = t_1 + L_{11P} + L_{11O} - (T)_{start}. \tag{5.2}$$

Similarly, the TDC value measured at the right side of S_{11} is written as:

$$T_{r11} = t_1 + R_{11P} + R_{11O} - (T)_{start} \tag{5.3}$$

The average of the measured TDC values of the side right and left of the paddle can be written as:

$$T_{11} = \frac{T_{r11} + T_{l11}}{2} = t_1 - (T)_{start} + \frac{L_{11O} + R_{11O}}{2} + \frac{L_{11P} + R_{11P}}{2}. \tag{5.4}$$

Similarly for the S_{21} paddle, one can write,

$$T_{21} = t_2 - (T)_{start} + \frac{L_{21O} + R_{21O}}{2} + \frac{L_{21P} + R_{21P}}{2} \tag{5.5}$$

where t_2 is the time at which the scattered particle strikes S_2. As shown in Fig. 5.1, L_1 and L_2 are the lengths of the paddles of S_1 and S_2 respectively, and x is the distance from the right end of the paddle to the point where the particle strikes the scintillator. The signal propagation time within the scintillator in S_{21} is given by:

$$R_{21p} + L_{21p} = \frac{L_2 - x}{v_{eff}} + \frac{x}{v_{eff}} = \frac{L_2}{v_{eff}} \tag{5.6}$$

Where v_{eff} is the effective signal propagation speed in the scintillator paddle. Simi-

larly for S_{11} one can write

$$R_{11p} + L_{11p} = \frac{L_1 - x}{v_{eff}} + \frac{x}{v_{eff}} = \frac{L_1}{v_{eff}} \tag{5.7}$$

From Eqn. 5.4 and 5.5, we obtain

$$T_{21} - T_{11} = \triangle t + \frac{O_{21} - O_{11}}{2} + \frac{\triangle L}{2 * v_{eff}} \tag{5.8}$$

where $\Delta t = t_2 - t_1$ is the TOF of the particle from S_{11} to S_{21}. Moreover, $O_{21} = R_{21O} + L_{21O}$, $O_{11} = R_{11O} + L_{11O}$ and $\Delta L = L_2 - L_1$. For the particle moving from the i^{th} paddle of S_1 to j^{th} paddle of S_2, Eqn. 5.8 can be written as

$$y_{(1i)(2j)} = x_{(1i)(2j)} + C_{(1i)(2j)} \tag{5.9}$$

where $y_{(1i)(2j)} = T_{2j} - T_{1i}$, $x_{(1i)(2j)} = t_{2j} - t_{1i}$ and $C_{(1i)(2j)} = \frac{O_{2j} - O_{1i}}{2} + \frac{\triangle L}{2 * v_{eff}}$. The linear fit of Eqn. 5.9 gives the timing offset O_{2j} and O_{1i}.

5.1.2 Optimizing the Coincidence Time

The coincidence time (CT) between two spectrometers is defined as the TOF difference between the scattered electron and proton created at the same reaction vertex. The optimization of the CT is very important in the analysis becasue of the following reasons.

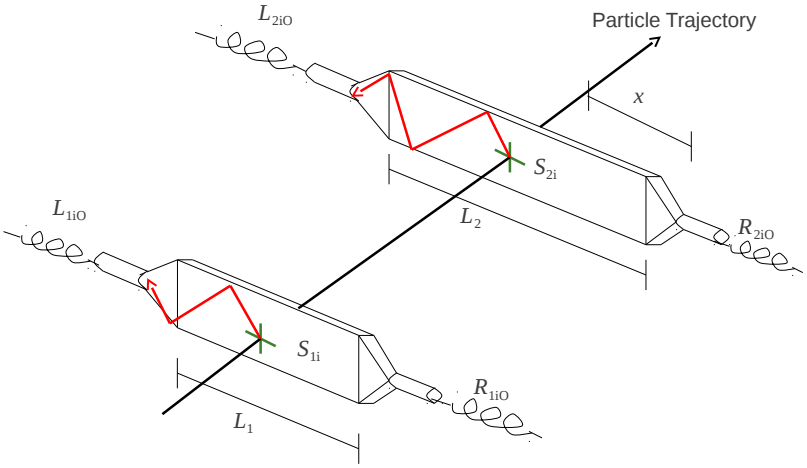

Figure 5.1: The measurement of the time of flight in two scintillator paddles.

- It helps to remove random coincidences. The percentage of the random coincidences is proportional to the width of coincidence window. Therefore, the main objective of the CT optimization is to minimize the width of coincidence window.

- It is also used for particle identification (PID) in order to separate the electron and proton events detected in the LHRS and RHRS respectively. The location of the peak of the CT distribution refers to the TOF of electrons with respect to the TOF of proton.

The same optimization method applied to correct the TOF in a single spectrometer was also used to optimize the CT between the two spectrometers. In this case, in

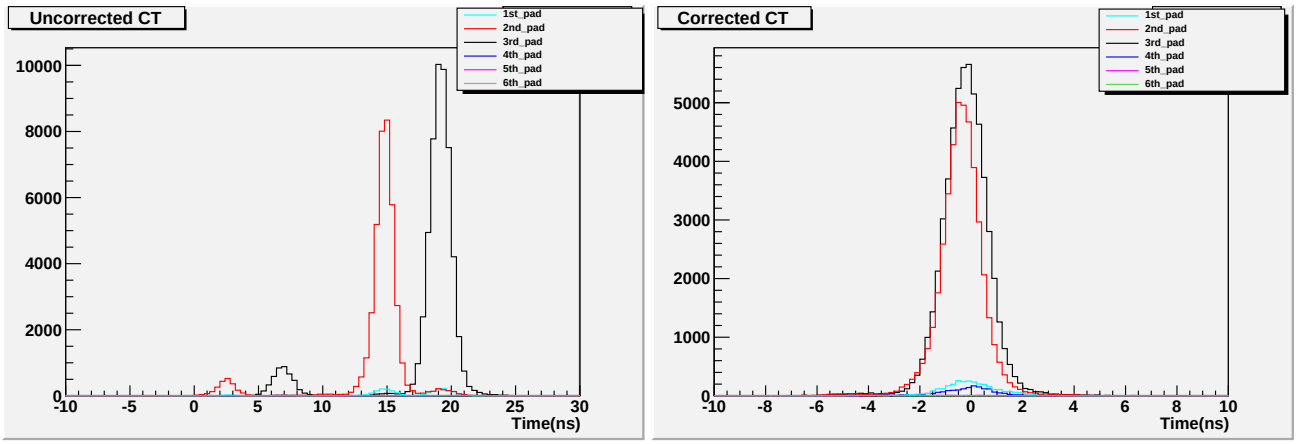

Figure 5.2: The Coincidence time before and after the correction

Eqn. 5.9, S_1 was replaced by the left S_2, S_{2L} and S_2 by the right S_2, S_{2R}.

$$y_{(li)(rj)} = x_{(li)(rj)} + C_{(li)(rj)} \tag{5.10}$$

where $y_{(li)(rj)} = T_{rj} - T_{li}$, $x_{(li)(rj)} = t_{rj} - t_{li}$ and $C_{(li)(rj)} = \frac{O_{rj} - O_{li}}{2} + \frac{\triangle L}{2 * v_{eff}}$. Finally linear fits of Eqn. 5.10 to experimental data determine the coincidence timing offset. The CT distribution due to individual paddles before and after optimization is shown in Fig. 5.2. The optimization aligns the location of the CT peak due to individual paddles to the same point.

5.2 Determination of the Beam Position

The Struck 7510 Analog to Digital Converter (ADC) was used in Burst Mode for beam raster and Beam Position Monitor (BPM) readings. In Burst Mode, the ADC values are read four times per trigger, separated by 4 μs. These four time readings allow one to precisely track the beam motion and correct the beam position for phase shift. In this analysis we only considered the beam positions measured from the

BPM. There are two BPM on either sides of the target, BPMA and BPMB. The four antennae of the each BPM are labeled as X_p, X_m, Y_p and Y_m. The antennae read the beam signals and the position signals are converted by the BPM ADC's. The beam positions measured in the rotated coordinate system of BPM are given by [43].

$$x_{rot} = \kappa \frac{X_{p,cor} - \alpha_x X_{m,cor}}{X_{p,cor} + \alpha_x X_{m,cor}} \tag{5.11}$$

Where the ADC values are corrected relative to their corresponding pedestals such that,

$$X_{p,cor} = X_p - X_{p,peed}. \tag{5.12}$$

The equation for y_{rot} is also calculated in similar manner. Here α_x is a parameter which corrects the different gains in the antenna, and κ is the conversion coefficient which converts the ADC value into the unit of length. The complete beam profile in the Hall A coordinate system is defined by four points. The x and y coordinates of each point of the beam profile are calculated by rotating the left handed BPM into the right handed Hall A coordinate system via

$$x = x_0 + \kappa_x \frac{y_{rot} - x_{rot}}{\sqrt{2}} \tag{5.13}$$

$$y = y_0 + \kappa_y \frac{y_{rot} + x_{rot}}{\sqrt{2}}. \tag{5.14}$$

Where κ_x and κ_y are the calibration coefficients. The coefficients α_x, α_y, κ_x and κ_y were determined from the hardware calibration while pedestals were obtained from special pedestal calibration runs.

5.2.1 Optimizing the Beam position

The beam position is optimized to correct for the beam offset, the beam motion amplitude and the phase of the raster motion. The motion of the electron beam can be described by a sinusoidal function.

$$y(t) = y_0 + Acos(\omega t + \phi) \tag{5.15}$$

which can also be written in the following way:

$$y(t) = y_0 + Acos(\omega t)cos(\phi) - Asin(\omega t)sin(\phi) \tag{5.16}$$

Where ω is $2\pi\nu$, ν the raster frequency. The non linear Eqn. 5.16 can written in the linear form as:

$$y(t) = \sum_{j=1}^{3} a_j(t) z_j \tag{5.17}$$

Where $a_1 = 1, a_2 = cos(\omega t), a_3 = sin(\omega t), z_1 = a_0, z_2 = Acos(\phi)$ and $z_3 = -Asin(\phi)$. Eqn. 5.17, a linear equation, gives the position of beam at any time t. Here z_j are the parameters and a_i are the independent variables. The major task here is

to fit Eqn. 5.17 to the given data points $y_i(a_j, t_i)$, which are read at time t_i, by χ^2 minimization, where χ^2 is given by:

$$\chi^2 = \sum_i (y_i - y(t_i))^2 = \sum_i (y_i - \sum_j (a_j^i z_j))^2 \tag{5.18}$$

To minimize the χ^2 we use the following relation:

$$\frac{\partial \chi^2}{\partial z_k} = 0 = \sum_i (y_i - \sum_j (a_j^i z_j) a_k^i) \tag{5.19}$$

Eqn. 5.19 can be written in the form of matrix

$$\begin{pmatrix} 4 & \sum_i cos(\omega t_i) & \sum_i sin(\omega t_i) \\ \sum_i cos(\omega t_i) & \sum_i cos^2(\omega t_i) & \frac{1}{2}\sum_i sin(\omega t_i) \\ \sum_i sin(\omega t_i) & \frac{1}{2}\sum_i sin(\omega t_i) & \sum_i sin^2(\omega t_i) \end{pmatrix} \begin{pmatrix} z_1 \\ z_2 \\ z_3 \end{pmatrix} = \begin{pmatrix} \sum_i y^i \\ \sum_i y^i cos(\omega t_i) \\ \sum_i y^i sin(\omega t_i) \end{pmatrix} \tag{5.20}$$

After solving Eqn. 5.20, one gets:

$y_0 = z_1$

$A = \sqrt{(}z_2^2 + z_3^2)$

$\phi = atan2(-z_3, z_2)$

Thus, the optimized beam position can be written as

$$y(t) = y_0 + Acos(\phi + \phi_{delay}) \tag{5.21}$$

where ϕ_{delay} is the phase constant. If (x_1, y_1, z_1) is the position of the beam measured in BPMA and (x_2, y_2, z_2) is the position of the beam at BPMB then one can write

$a_x = x_2 - x_1$

$a_y = y_2 - y_1$

$a_z = z_2 - z_1$.

The angle θ of beam in the xy plane of the Hall A Coordinate System can be written as

$$\theta_{beam} = \frac{a_x}{a_z} \tag{5.22}$$

The angle ϕ is the angle between beam direction and the xz plane:

$$\phi_{beam} = \frac{y}{\sqrt{(a_x^2 + a_z^2)}} \tag{5.23}$$

The beam axis is along the direction of z-axis in the Hall A coordinate system. The x and y positions of the beam in target are given by:

$$x_{beam} = \frac{x_1 z_2 - x_2 z_1}{a_3} \tag{5.24}$$

$$y_{beam} = \frac{y_1 z_2 - y_2 z_1}{a_3}. \tag{5.25}$$

Figs. 5.3 shows the optimized x and y positions of beam at target.

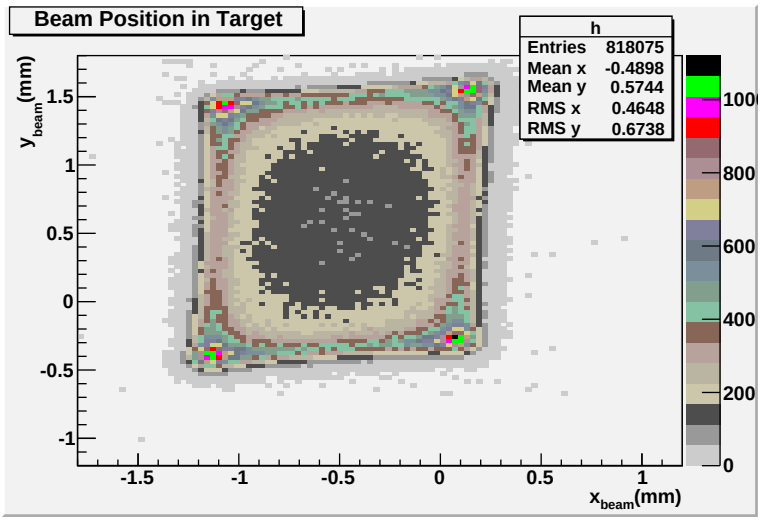

Figure 5.3: The corrected beam position in target with Raster size 2mm × 2mm.

5.3 Target Reconstruction

A cylindrical target cell with a spherical front cap (cigar tube shaped cell) was used in this experiment. Incident and scattered particles traverse through different material thicknesses in the target. The path length in the target is very important for the calculation of the energy loss for the incident and scattered particles. For incident electrons, the path length in the target cell is equal to the distance between front window and the reaction point.

$$d_{target} = z_{front} - z_0 \tag{5.26}$$

where z_{front} is the z-position of the front window of the cell in the target coordinate system and z_0 is the z-position of the reaction vertex. The path length of the scattered particles depends upon the position of the reaction vertex O(x_0, y_0, z_0), the scattering

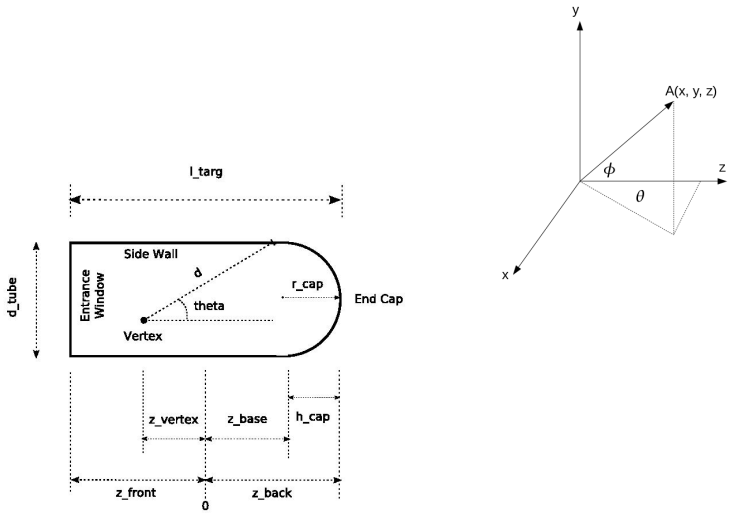

Figure 5.4: Geometry and coordinate of the target Cell.

polar angle (θ), the azimuthal angle (ϕ) and the geometry of the target. In the target coordinate system as shown in Fig. 5.4, A(x, y, z) is the point of intersection of the particle trajectory with the target wall. In a spherical coordinate system we can write

$x - x_0 = dsin\theta cos\phi$

$y - y_0 = dsin\phi$

$z - z_0 = dcos\phi cos\theta$

The radius of the tube is given by:

$$x^2 + y^2 = r_{tube}^2 \tag{5.27}$$

The path length of a particle that escaped from the side-wall of the cylinder is given by:

$$d_{side} = \frac{-b_1 \pm \sqrt{(b_1^2 - 4a_1c_1)}}{2a_1} \tag{5.28}$$

Where

- $a_1 = sin^2\phi + sin^2\theta cos^2\phi$
- $b_1 = 2(x_0 sin\theta cos\phi + y_0 sin\phi)$
- $c_1 = x_0^2 + y_0^2 - r_{tube}^2$

If the scattered particles have escaped from the spherical surface of the end cap then Eqn. 5.27 has to be modified as

$$x^2 + y^2 + (z - z_c) = R_{cap}^2 \tag{5.29}$$

Where $z_c = l/2 - R$ is the position of the center of the end cap on z-axis and R_{cap} is the radius of the spherical end cap. After solving Eqn. 5.29 for the path length, we get

$$d_{cap} = \frac{-b_2 \pm \sqrt{(}b_2^2 - 4a_2c_2)}{2a_2} \tag{5.30}$$

where

- $a_2 = 1$
- $b_2 = 2(x_0 sin\theta + y_0 sin\phi cos\theta + (z_0 - z_c)cos\theta cos\phi)$
- $c_2 = x_0^2 + y_0^2 + (z_0 - z_c)^2 - R^2$

The actual path of particle,d, can be calculated according to the following criteria

- *Case A*: $z_0 < z_{base}$

  $$\mathrm{d} = \begin{cases} d_{side} & \text{if} d_{side} \leq d_{base} \\ d_{cap} & \text{if} d_{side} > d_{base} \end{cases}$$

- *Case B*: $z_{base} \leq z_0$

  $$d = d_{cap}$$

where

$$d_{base} = \frac{z_{base} - z_0}{cos\theta} \tag{5.31}$$

$$z_{base} = l/2 - h_{cap} \tag{5.32}$$

where h_{cap} is the length of the end cap.

5.4 Energy Loss Correction

The incident and scattered particles further lose energy as they traverse through windows, air, detectors and target. The goal of the energy loss correction is to calculate the momentum of the particles at the reaction vertex. At the vertex, the energy of the incident electron is less than the beam energy before entering the target cell. On the other hand scattered particles have more energy at the vertex than the energy measured in the spectrometers. The incident electron loses energy as it travels through the target cell wall and liquid target material, while scattered particles lose energy in the material, the target cell, the target chamber window, air and kapton (spectrometers windows). The energy of the incident particles E_{in} and scattered

particles E_{sc} at vertex can be written as:

$$E_{in} = E_{beam} - E_l(cell) - E_l(target) \tag{5.33}$$

$$E_{scat} = E_{measured} + E_l(cell) + E_l(target) + E_l(chamber) + E_l(air) + E_l(kapton) \tag{5.34}$$

where E_l = energy loss.

5.4.1 Mean Energy Loss

Heavy charged particles such as protons lose energy in elastic collisions with electrons in the atom called atomic collision. Energy loss also occurs in elastic scattering of nuclei. However this process does not happen as often as atomic collisions with electrons and very little energy is transferred. A large number of atomic collisions occur per unit length in matter and its cumulative effect is statistical in nature and best described by the average energy loss per unit length. For the proton, the mean energy loss per unit length can be described by the Beth-Bloch equation[44].

$$-\frac{1}{\rho}\frac{dE}{dx} = Kz^2\frac{Z}{A}\frac{1}{\beta^2}[\frac{1}{2}ln\frac{2m_ec^2\beta^2\gamma^2T_{max}}{I^2} - \beta^2 - \frac{\delta(\beta\gamma)}{2} - \frac{C}{Z}] \tag{5.35}$$

where,

- $K = 4\pi N_A r_e^2 m_e c^2$
- $T_{max} = \frac{2m_e c^2 \beta^2 \gamma^2}{1+2\gamma m_e/M+(m_e/M)^2}$ which is the maximum kinetic energy transferred to a free electron in a single collision
- I is the mean excitation energy of the medium
- δ is the density effect correction
- C_z is the shell correction.

The energy loss of an electron is somewhat different than the energy loss of a heavy charged particle like a proton because of two reasons. First, the electron has much smaller mass. Second, the incident particle, the electron, collides with an identical particle, an atomic electron, so that their indistinguishably must be taken into account in the calculation. When high energy electrons traverse through matter, they lose energy in atomic collisions as well as in the electric field of nuclei in the form of electromagnetic radiation (bremsstrahlung radiation). Energy loss due to radiation is corrected in radiative corrections. In this section, we only discuss the energy loss of electrons due to atomic collisions. For electrons, the Beth-Bloch formula for the mean energy loss given in Eqn. 5.35 has been modified as [44]:

$$-\frac{1}{\rho}\frac{dE}{dx} = Kz^2\frac{Z}{A}\frac{1}{2\beta^2}[ln(\frac{T^2}{I^2}) + ln(1+\frac{\tau}{2}) + F(\tau) - \delta - 2\frac{C}{Z}] \tag{5.36}$$

where,

$$F(\tau) = (1-\beta^2)[1 + \frac{\tau^2}{8} - (2\tau+1)ln2] \tag{5.37}$$

and $\tau = T/m_e c^2$ is the kinetic energy of the electron in the unit of $m_e c^2$. The mean energy loss distribution of protons and electrons, and their corresponding path length distribution in the target are shown in Fig. 5.5. The energy loss of the majority of the scattered particles in the target is 6 MeV and less.

5.4.2 The Most Probable Energy Loss

In a low density and thin target, the number of collisions is too small and a larger amount of the energy is transferred in a single atomic collision. In this case, one gets a long tail on the low energy side of the energy loss probability distribution. It indicates that the peak in the distribution does not correspond to the mean value of the energy. The most probable value of energy loss is calculated using a Landau-Vavilov distribution [45].

$$\Delta_p = \xi[ln(\frac{2m_e c^2 \beta^2 \gamma^2}{I}) + ln(1+\frac{\xi}{I}) + j - \beta^2 - \delta(\beta\gamma)] \tag{5.38}$$

Where $\xi = (KZ/2A)(x/\beta^2)$ in MeV, x is the thickness of target in g/cm^2 and j = 0.200 is constant.

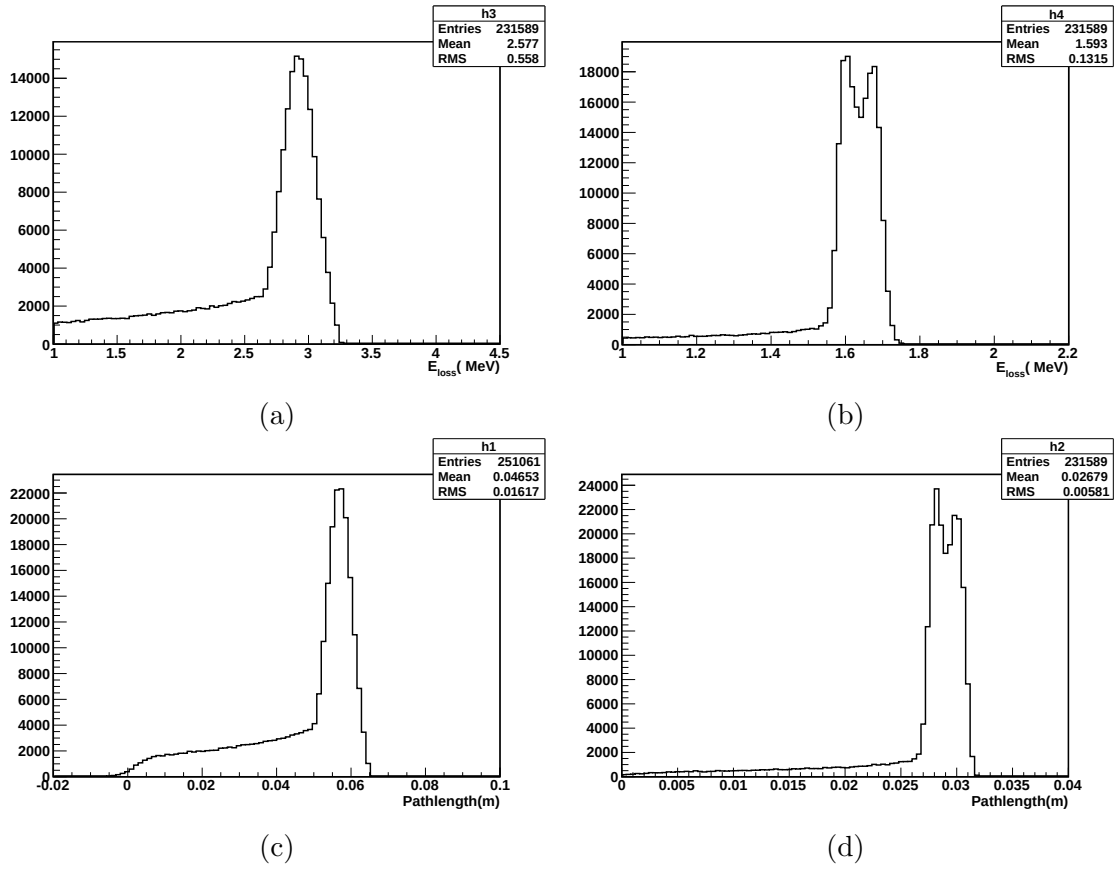

Figure 5.5: (a) and (b) are the mean energy loss by the scattered electron and proton in the target and (c) and (d) are the distribution of the path length of scattered electron and proton in extended target

5.5 The Spectrometer Calibration

The objective of the spectrometer calibration is to determine the spectrometer absolute momentum and angular offsets of scattered particles. The methods of χ^2- fitting to the equations of conservation of momentum and energy for a given reaction, an elastic scattering of hydrogen at a fixed and known beam energy, were used. The main work was to correct the central kinematic variables, the spherical in-plane angle θ, out-plane angle ϕ and momentum of the particles p, of each spectrometer. (θ_e, ϕ_e, p_e) are the central kinematics variables of the LHRS and (θ_p, ϕ_p, p_p) are those for the RHRS. The spectrometer calibration is very important to determine the angular distribution of the recoiling neutron and the absolute reaction cross section. The central kinematic variables were corrected by using calibration runs with the liquid hydrogen target at $Q^2 = 0.8$ (GeV/c) ^{2}, $E_{beam} = 2.834$ GeV and $x_{bj} = 1$.

The momentum vector of the incident electron beam in the Hall A coordinate system is given by:

$$\vec{k} = (0, 0, \vec{e}). \tag{5.39}$$

.

Similarly the momentum vectors of the scattered electron and proton are:

$$\vec{p_e} = (p_e sin\theta_e cos\phi_e, p_e sin\phi_e, p_e cos\theta_e cos\phi_e) \tag{5.40}$$

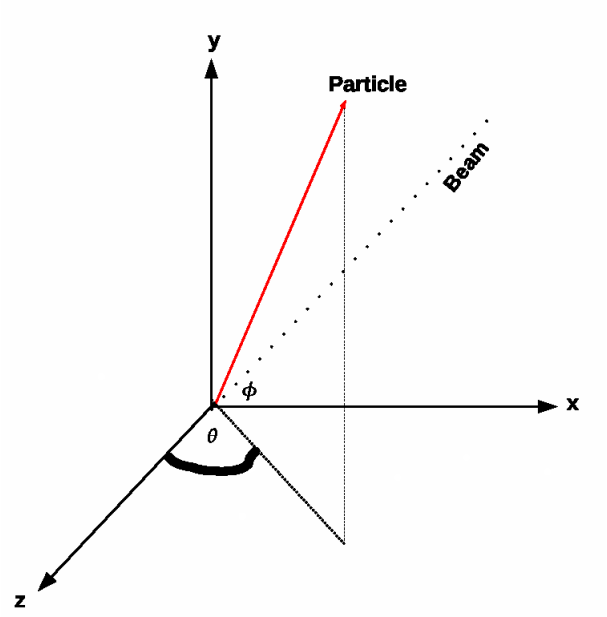

Figure 5.6: Electron scattering from the hydrogen target in the hall coordinate system.

$$\vec{p}_p = (p_p sin\theta_p cos\phi_p, p_p sin\phi_p, p_p cos\theta_p cos\phi_p) \tag{5.41}$$

Using Eqn.(5.39 - 5.41), one can write the x, y and z components of the missing momentum vector, $\vec{p}_m$ as:

$$p_{mx} = 0 - (p_e sin\theta_e cos\phi_e + p_p sin\theta_p cos\phi_p) \tag{5.42}$$

$$p_{my} = 0 - (p_e sin\phi_e + p_p sin\phi_p) \tag{5.43}$$

$$p_{mz} = e - (p_e cos\theta_e cos\phi_e + p_p cos\theta_p cos\phi_p) \tag{5.44}$$

Table 5.1: Kinematic Correction Factor for q1 and q2 data sets.

$Q^2(GeV)^2$	δp_e(GeV/c)	$\delta\theta_e$(rad)	$\delta\phi_e$(rad)	δp_p(GeV/c)	$\delta\theta_p$(rad)	$\delta\phi_p$(rad)
2.1	1.6 $\times 10^{-4}$	1.4 $\times 10^{-4}$	5.0 $\times 10^{-4}$	7.0 $\times 10^{-4}$	-1.75 $\times 10^{-4}$	1.46 $\times 10^{-4}$
0.8	5.46 $\times 10^{-4}$	6.53 $\times 10^{-4}$	7.5 $\times 10^{-4}$	-1.65 $\times 10^{-3}$	-1.4 $\times 10^{-3}$	-1.5 $\times 10^{-4}$

The missing energy of the reaction is written as :

$$E_{miss} = e - p_e + M_p - E_p. \tag{5.45}$$

Where E_p and M_p are the energy and mass of the proton. In order to optimize the above equations, correction terms were added in the kinematic variables on the right hand sides of Eqn.(5.42 - 5.45) i.e $p_e \rightarrow p_e+\delta p_e$, $\theta_e \rightarrow \theta_e+\delta\theta_e$, $\phi_e \rightarrow \phi_e+\delta\phi_e$, $p_p \rightarrow p_p+\delta p_p$, $\theta_p \rightarrow \theta_p + \delta\theta_p$ and $\phi_p \rightarrow \phi_p + \delta\phi_p$, where the δ's are the correction terms. The χ^2 minimization fitting of Eqns.(5.42 -5.45) to the experimentally measured quantities, $\theta_e, \phi_e, p_e, \theta_p, \phi_p, p_p, p_{mx}, p_{my}, p_{mz}$ and E_{miss}, on an event by event basis was used to determine the absolute momentum corrections and angular offsets, where χ^2 is given by:

$$\chi^2 = \Sigma(y(x,\delta) - y(x))^2 \tag{5.46}$$

where x represents the kinematics variable. All the correction terms for central kinematic variables are given in Table 5.1.

The corrected missing energies of the (e,e'p) reaction for the hydrogen and deuterium targets are shown in Fig. 5.7. For the deuterium target, the missing energy distri-

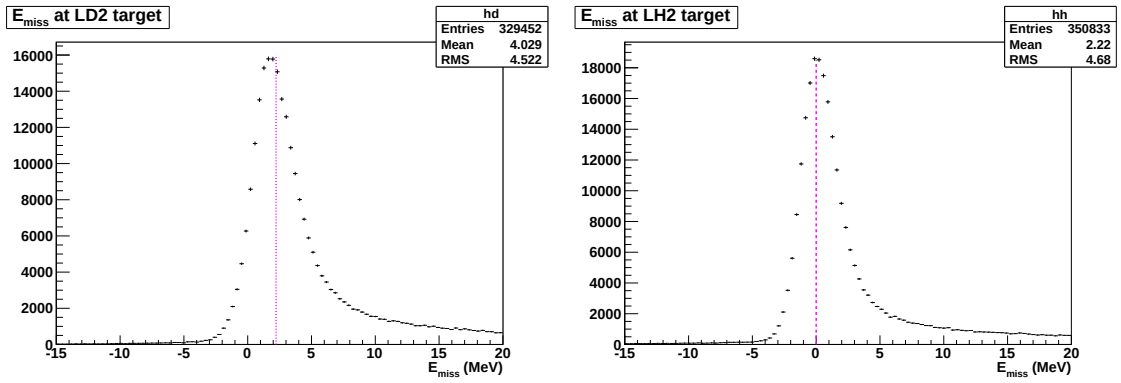

Figure 5.7: Corrected Missing Energy at Deuterium and Hydrogen target at $Q^2 = 0.8$ $(\mathrm{GeV/c})^2$

bution peak lies approximately at 2.224 MeV, its binding energy while for hydrogen target it lies approximately at zero.

5.6 The Software

The raw data from the data acquisition (DAQ) system were decoded and analyzed by the standard Hall A event processing software called the ANALYZER. The most common physics analysis task for inclusive (e, e') and coincidence (e, e'p) reactions are available in the ANALYZER. The performance of the ANALYZER is based on the data obtained from the standard Hall A experimental equipment, the high resolution spectrometers and detectors. During experiment E01020, the ANALYZER was not completed. At that time the analysis software ESPACE was used for event processing in Hall A. In order to analyze data with the new ANALYZER and have similar output as ESPACE, many classes and functions were rewritten to the software. Mainly, classes used to calculate the TOF, coincidence time, beam position and reaction

vertex location were rewritten. The ANALYZER uses multi-dimensional polynomials to transform the position and angles($y_{fp}, \theta_{fp}, \phi_{fp}$) of the scattered particles measured in the focal plane to the reaction vertex coordinate ($y_{tg}, \theta_{tg}, \phi_{tg}$) [7]. The final physics analysis was carried out using several software systems and high level programming languages, PyROOT, ROOT, Matplotlib, C++ and python.

5.7 Event Selection

Many cuts were applied during the analysis in order to select good coincidence events in the final state. The following are the major cuts:

5.7.1 Event Selection Cut

Coincidence events between left and right spectrometers were selected using T5 trigger types events.

5.7.2 VDC tracking cut

The group of VDC wires which fire in each wire plane when a particle traverses through all four VDC planes of each spectrometer is called multiplicity (Mult). The VDC tracking cut is applied in order to select the good events such that the multiplicity of each event should be equal or larger than three.

5.7.3 Target Length cut

Events that originated close to the entrance window and end of the target walls can be eliminated by cutting the reconstructed reaction point along the beam direction. In this analysis cut $|z_{react}| < 5.0$ cm was used resulting in an effective target length of 10cm instead of the full length of 15cm.

5.7.4 Cut on the difference of vertex position

For coincident events, the vertex position measured from either spectrometer should be the same. A cut on the absolute difference of the vertex position, $\delta z = |z_{lreact} - z_{rreact}| < 2.0$ cm was used to remove most of the accidental coincidence events. The vertical dashed red lines in Fig. 5.8 show the cut limits in a histogram of δz used in the analysis.

5.7.5 Coincidence Time Cut

The distribution of the coincidence time between left and right spectrometers is shown in Fig. 5.9. The vertical dashed lines separate the real and accidental coincidence time windows. The timing window between blue lines, W_r, is the real window which has both real and accidental coincidence events, while the windows between two red lines W_{a1} and W_{a2} are accidental windows and have only accidental coincidence events.

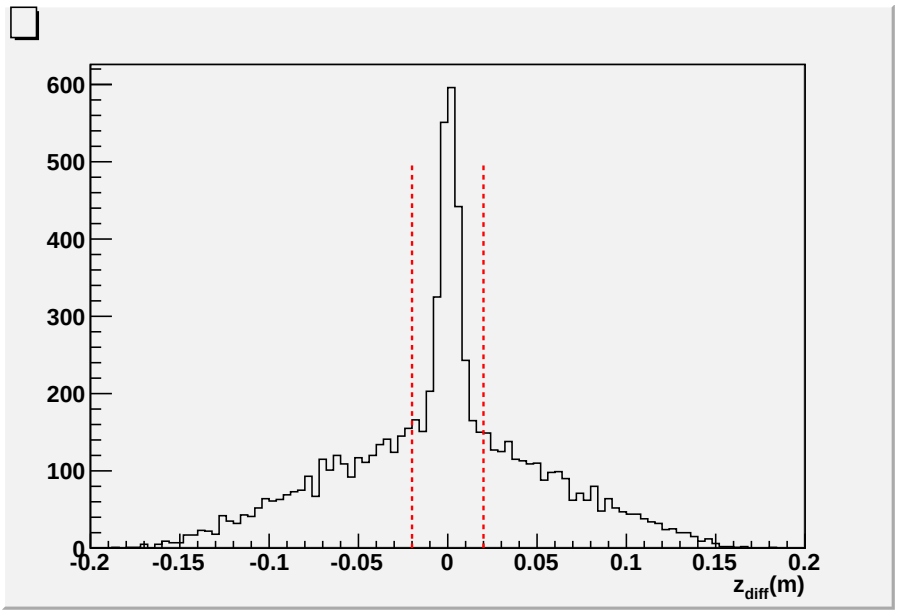

Figure 5.8: Cut applied in the difference of the vertex positions measured from left and right spectrometers.

The number of true coincidence events N_t in W_r were determined from the following relation:

$$N_t = N_r - N'_a. \tag{5.47}$$

Where N_r and N'_a are the real and accidental coincidence events within real window W_r. The average accidental coincidence events per unit coincidence time is given by

$$< N_a >= \frac{N_{a1} + N_{a2}}{W_{a1} + W_{a2}} \tag{5.48}$$

Therefore, we can write

$$N'_a =< N_a > W_r \tag{5.49}$$

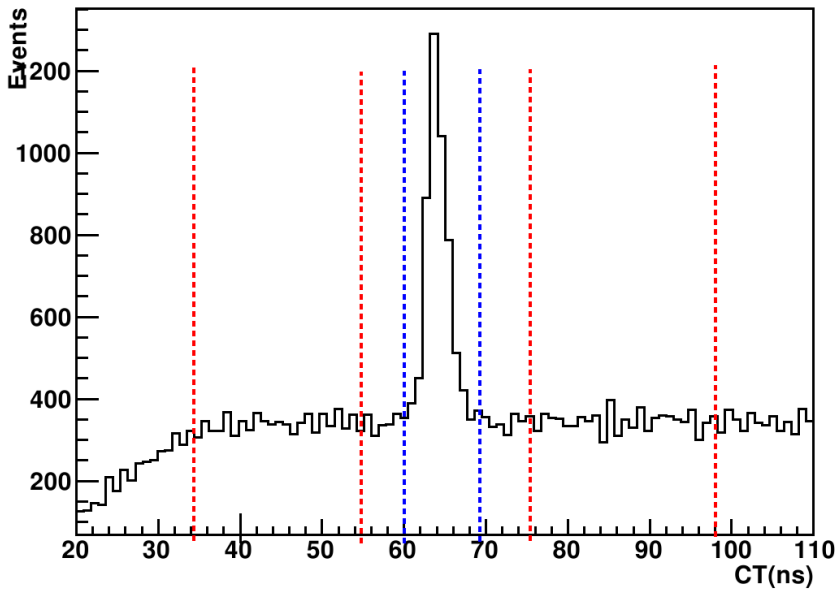

Figure 5.9: Coincidence time spectrum measured in two spectrometers.

Putting the values of $< N'_a >$ in Eqn. 5.47 gives the true coincidence events within W_r.

5.7.6 Missing Energy Cut

In deuteron electron-disintegration, the peak of the missing energy distribution should be at the binding energy of the deuteron of 2.224 MeV. However the peaks in the real data were found to be at slightly different positions. The missing energy cuts from -10 MeV to 15 MeV was used in both data and simulation to remove remaining contributions from pions in the data, and are shown in Fig. 5.10.

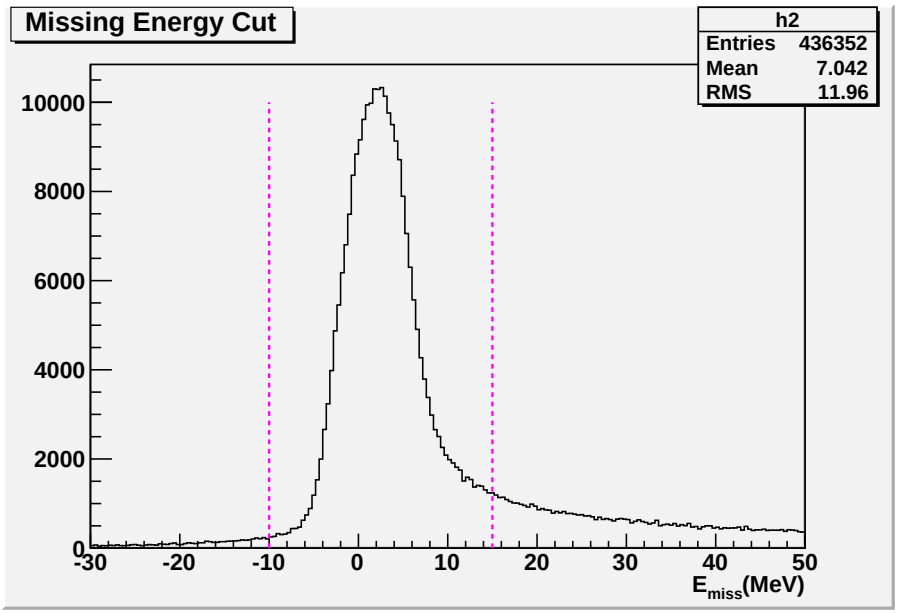

Figure 5.10: Missing Energy cut $-10(MeV) < E_{miss} < 15.0(MeV)$.

5.7.7 Relative Momentum Cut

The quantity $\delta = (p - p_0)/p_0$ measures the fractional deviation of the momentum, p, of the particle from the central momentum, p_0, of the spectrometers. This was limited by the cut $|\delta| < 0.04$.

5.7.8 PID Cut

As described in 3.6.3, pions produce much less radiation in the Cerenkov detector than electron. The cut on the sum of the ADC values ($ADCSUM > 80$) in the Cerenkov detector was to separate the pion events from the electron events.

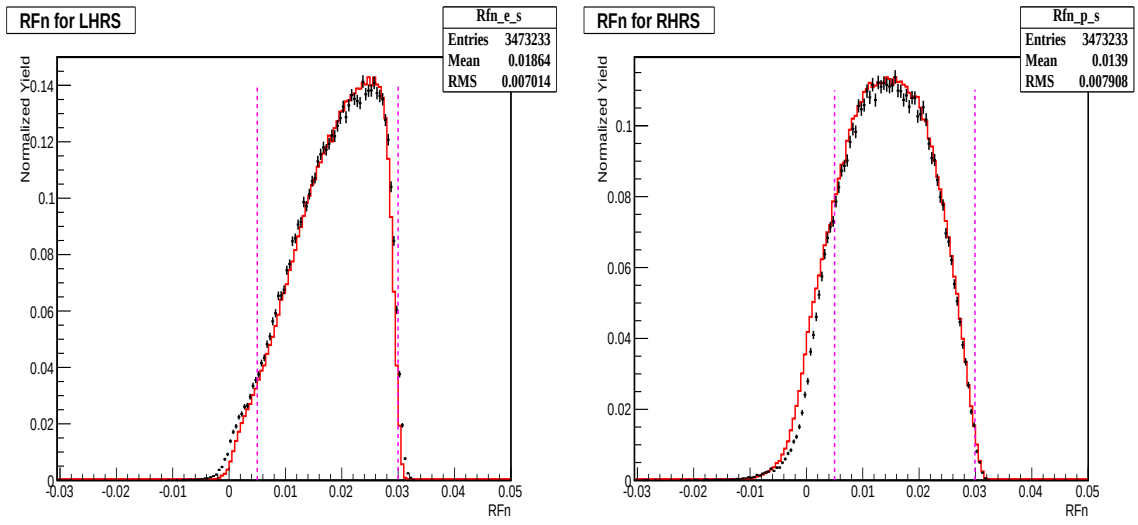

Figure 5.11: Cut applied in the R-Function (a)Left Spectrometer and (b) Right Spectrometer. Red solid line is from Monte Carlo simulation. Cut $0.005 < RFn < 0.03$ was chosen in both spectrometers

5.7.9 R-Function Cut

The acceptance of the spectrometer can be treated as a four-dimensional region of the target variables $y_{tg}, \theta_{tg}, \phi_{tg}$ and δ_{tg}. The distribution of the pair variables $(\theta_{tg}, \delta_{tg}), (\phi_{tg}, \delta_{tg}), (\phi_{tg}, y_{tg})$ and (θ_{tg}, ϕ_{tg}) represents the acceptance of the spectrometers. The function of these variables $RFn(y_{tg}, \theta_{tg}, \phi_{tg}, \delta_{tg})$ is called an R-Function. The R-function is a real-valued function whose sign is completely determined by the signs of its arguments [46]. The value of R is a measure of how far an event is from the acceptance boundary. $RF_n = 0$ means on the boundary, while $RF_n < 0$ means outside of it. Fig. 5.11 shows the cut applied in RFn of left and right spectrometers.

5.8 The Radiative Correction

As the electron passes near the target atoms it interacts with the nucleus, and it accelerates in the electric field of the nucleus. This acceleration leads to the emission of virtual and real photons called internal Bremsstrahlung. Radiation of a real or virtual photon changes the (e, e'p) reaction cross section as well as the reaction kinematics at the vertex. Therefore, the measured cross sections were corrected for these radiative effects. The electron radiates photons, while it interacts with the coulomb field of a nucleus involved in the (e, e'p) reaction. This process is called internal Bremsstrahlung. The electron can also interact with the coulomb field of a nucleus other than the one involved in the scattering process and thereby radiate the photon. These radiations are known as external Bremsstrahlung. The electron can radiate before and/or after the reaction. If the electron radiates after the reaction, the kinematic at the location of the vertex is changed. The radiative correction due to internal bremsstrahlung has been first calculated by Schwinger [47] and later improved by Mo and Tsai [48]. The correction due to external bremsstrahlung has been done by Bethe [49]. In this analysis, the Monte Carlo program SIMC [50] was used to determine radiative corrections. The radiative correction for each bin was determined by comparing yields before and after the radiation effects have been applied in the simulation. The correction was done in the following two steps:

- The radiative correction factor (RCF), the ratio of yield of the non-radiative

distribution to the radiative distribution, for each bin was determined.

$$RCF = \frac{Y_{norad}}{Y_{rad}} \tag{5.50}$$

- The measured cross sections were multiplied by RCF to remove the effect of radiation losses.

The RCF for $p_{miss} = 200MeV/C$ at $Q^2 = 2.1$ (GeV/c) ^{2} and $Q^2 = 0.8$ (GeV/c)^2 is shown in Fig. 5.12. The different points show the RCF for different kinematic settings. At both valus of Q^2, it is shown that radiative effects increase the measured cross section by about a factor of 1.8 on average.

5.9 Hydrogen Normalization

In the present analysis, the measurement of the elastic ($^1H(e, e'p)$) cross section was used for normalization, and to determine the overall coincidence efficiency of the production data. The measured yield was compared to a simulation [51] using the proton electromagnetic form factor parametrization based on a comprehensive analysis of the world data. Cuts as described in section 5.7 were applied in both data and simulation. The ratio of measured yield to the simulation yield integrated within the cut of missing energy determined the normalization factor. As in the previously analyzed data at $Q^2 = 3.5$ GeV^2 [3], Arrington's parametrization [52] was used. Using [52] at both $Q^2 = 2.1$ (GeV)^2 and 0.8 (GeV)^2, a normalization factor $f_n = 0.84 \pm 0.02$ was determined, and a correction factor of (1.0/0.84) has been applied to all the measured $D(e, e'p)n$ cross section.

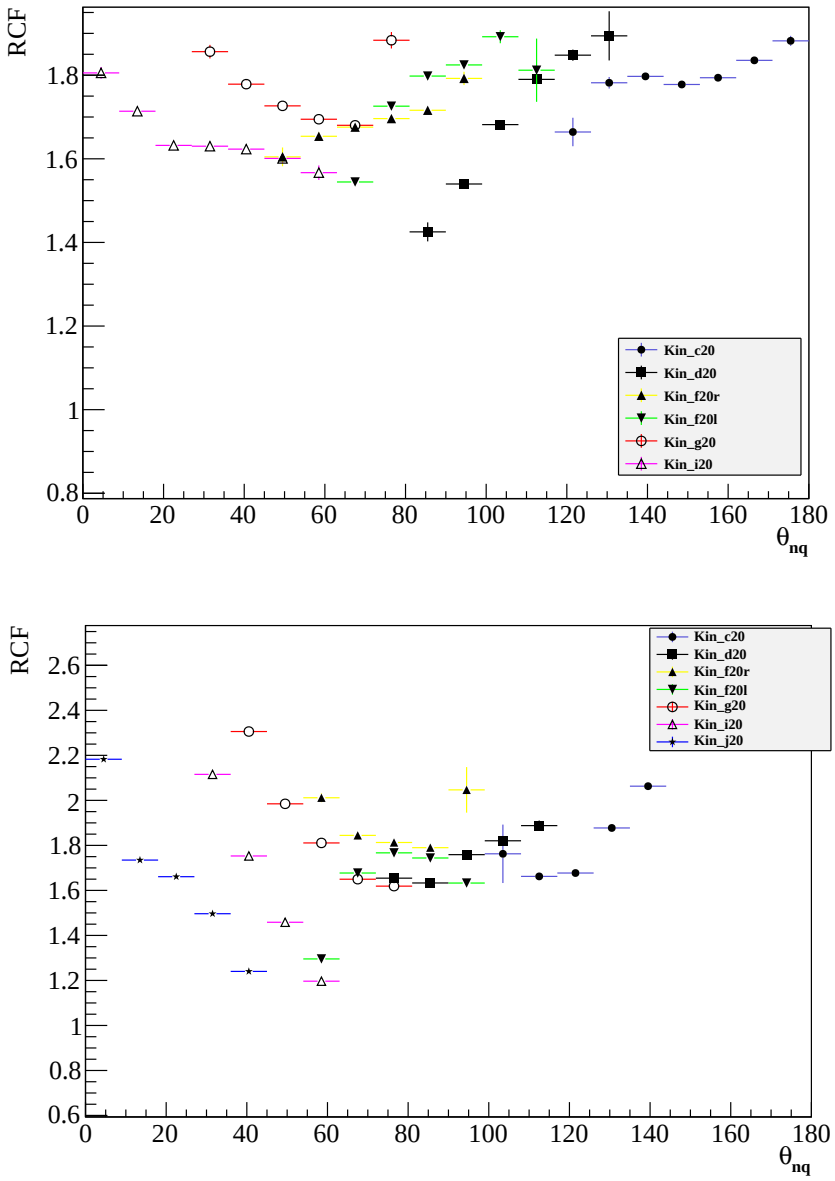

Figure 5.12: RCF for $p_{miss} = 200 MeV/c$ (a) at $Q^2 = 2.1 GeV^2$ (b) at $Q^2 = 0.8 GeV^2$

5.10 Extraction of Cross Section

The following steps were taken in order to extract the final cross section:

- Coincident proton and electron events were selected.
- The kinematic quantities at the reaction vertex were used to reconstruct the four momenta of the two particles.
- The measured electron and proton momenta were corrected to account for the energy loss due to the interaction with detectors and target materials.
- Cuts as described in section 5.7 were applied to select clean events in the final state.
- The background due to accidental coincidences was subtracted.
- Histograms of various kinematic variables were constructed. The necessary corrections including detector efficiency, the computer live time corrections, hydrogen normalization and target boiling factors were then applied to the data yield.
- The yields were normalized with the luminosity of incidence beam.
- From the SIMC Monte Carlo simulation [53], phase space and radiative correction factor were determined.
- The radiative corrections were applied to the corrected data yield.

- The final experimental cross section was obtained by dividing the correct yield by SIMC phase space.

The experimental five-fold differential cross section per bin is defined as:

$$\frac{d^5\sigma}{d\omega d\Omega_e d\Omega_p}(E_{miss}, p_{miss}, Q^2) = \frac{N'(E_{miss}, p_{miss}, Q^2)}{V(E_{miss}, p_{miss}, Q^2)}. \tag{5.51}$$

Where $N'(E_{miss}, p_{miss}, Q^2, W)$ is the corrected data yield and $V(E_{miss}, p_{miss}, Q^2)$ is the acceptance volume per bin in the momentum space obtained from the SIMC Monte-Carlo integration [54].

$$N'(E_{miss}, p_{miss}, Q^2) = \frac{f_{rc}.N_{uncorr}(E_{miss}, P_{miss})}{CLT.f_n.\epsilon_{track}.\epsilon_{vdc}.\epsilon_{trigg}.f_\rho(z_{react}, I)} \tag{5.52}$$

Where:

- $N_{uncorr}(E_{miss}, P_{miss})$ is the uncorrected data yield per bin,
- f_{rc} is the radiative correction factor,
- $f_\rho(z_{react}, I)$ is the boiling factor,
- f_n is the normalization factor,
- CLT is the computer live time,
- ϵ_{track} is the tracking efficiency,
- ϵ_{trigg} is the trigger efficiency,

- ϵ_{vdc} is the vdc efficiency.

The phase space volume per bin for the D(e, e'p)n reaction as calculated by SIMC Monte Carlo is:

$$V(E_{miss}, p_{miss}, Q^2) = \frac{N_{simc}(E_{miss}, P_{miss})}{N_{total}} \Delta V_{phspace} \tag{5.53}$$

where $N_{simc}(E_{miss}, P_{miss}$ is the number of sampled events in a bin and N_{total} is the total number of events in sample. The spectrometer phase space hypercube is:

$$\Delta V_{phspace} = \Delta\omega \Delta\Omega_e \Delta\Omega_p \tag{5.54}$$

Where $\Delta\Omega_e = \Delta\theta_e \cdot \Delta\theta_p$ is the electron spectrometer solid angle and $\Delta\Omega_p = \Delta\theta_p.\Delta\theta_p$ is the proton spectrometer solid angle.

5.11 Bin Centering Correction

The goal of the analysis is to extract the $D(e, e'p)n$ cross section for the range of recoil angles, θ_{nq}, at a fixed values of missing momentum, p_m and Q^2. Bin centering corrections are necessary to convert the experimental cross section from bin counts to the value of the cross section at the center of each bin. The correction factor is the ratio of the model cross sections calculated for each bin from the average kinematics, $\sigma^{calc}_{kin_{ave}}$, and the averaged cross section calculated from the SIMC Monte

Carlo Simulation,$\bar{\sigma^{calc}}$ [55] using the same theoretical model for the same bin.

$$f_{bc} = \frac{\sigma^{calc}_{kin_{ave}}}{\bar{\sigma^{calc}}} \tag{5.55}$$

where f_{bc} is the bin correction factor. The correction is of the order of few percent and it is typically larger at the edge of the acceptance. In this analysis, different theoretical models were used to check the model dependency. The experimental cross sections were corrected for bin centering:

$$\sigma^{exp}_{bc} = f_{bc}\sigma^{exp} \tag{5.56}$$

One of the advantage of the bin centering correction is that one can compare the experimental results to theoretical models without having to perform a time consuming Monte Carlo simulation.

Figs. 5.13 to 5.18 show the bin centering correction factors for different kinematic settings for $p_m = 200, 400$ and 500 MeV/c. The correction was carried out by using different theoretical models, Laget full and Laget PWIA [34]. The comparison between the bin centering correction with different models gives the model dependency correction of the cross section.

5.12 Systematic Uncertainties

Two types of systematic error were considered in the present analysis: uncertainties in overall normalization and kinematic variable uncertainties. The normalization

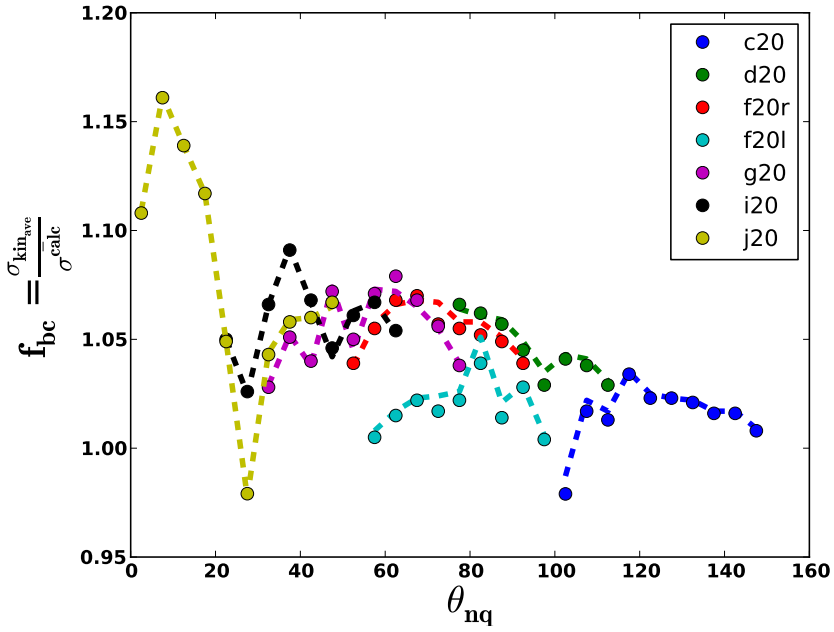

Figure 5.13: The comparison between the bin-centering correction factors using different theoretical models for $p_m = 200$ MeV/c at $Q^2 = 0.8$ GeV ^{2}. The points correspond to the bin-centering correction factor calculated with the full Laget Model. The thick dashed lines represent the bin correction with Laget PWIA.

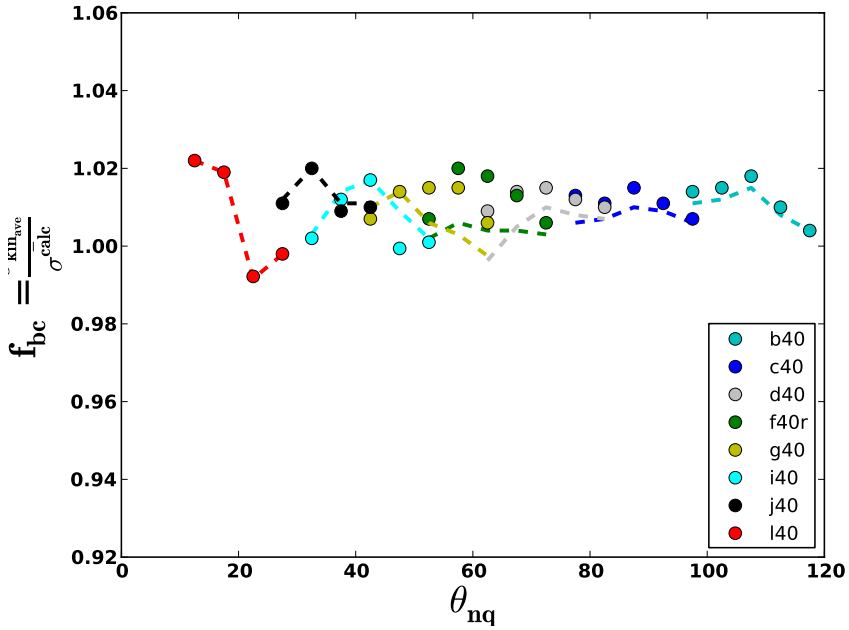

Figure 5.14: Like Fig. 5.13 for $p_m = 400$ MeV/c.

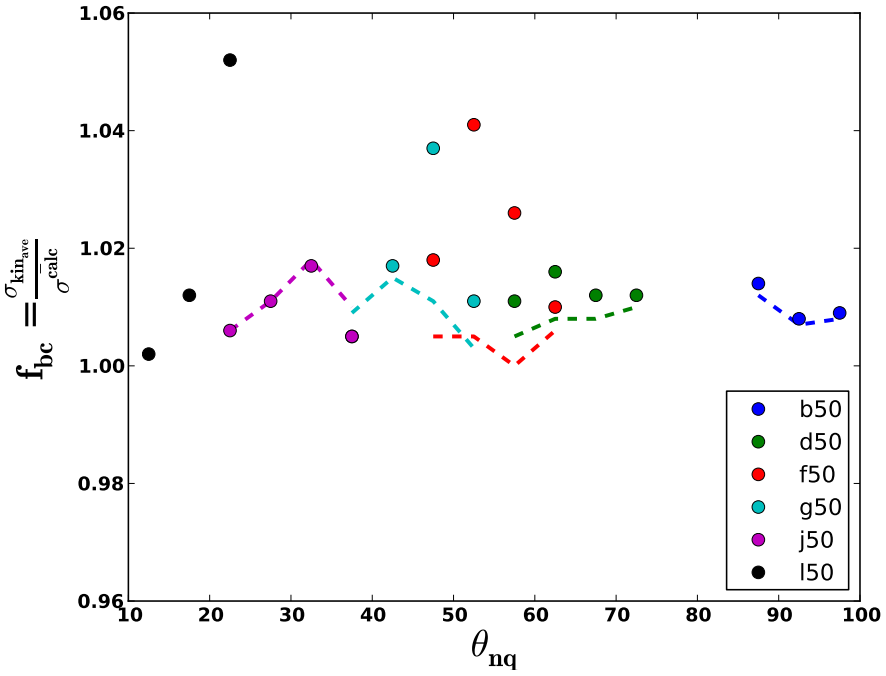

Figure 5.15: Like Fig. 5.13 for $p_m = 500$ MeV/c.

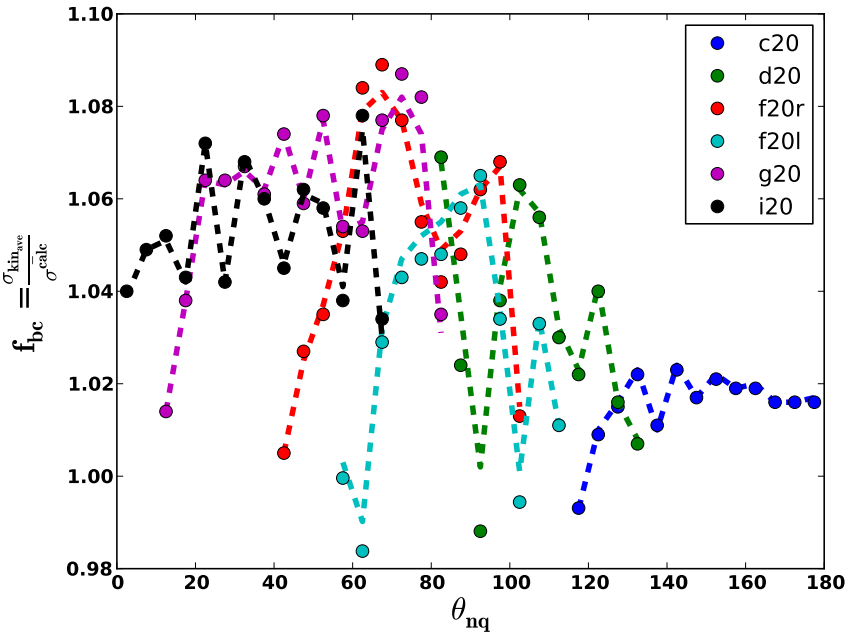

Figure 5.16: The comparison between the bin-centering correction factors using different theoretical models for $p_m = 200$ MeV/c at $Q^2 = 2.1$ GeV ^{2}. The points correspond to the bin-centering correction factor calculated with the full Laget Model. The thick dashed lines represent the bin correction with Laget PWIA.

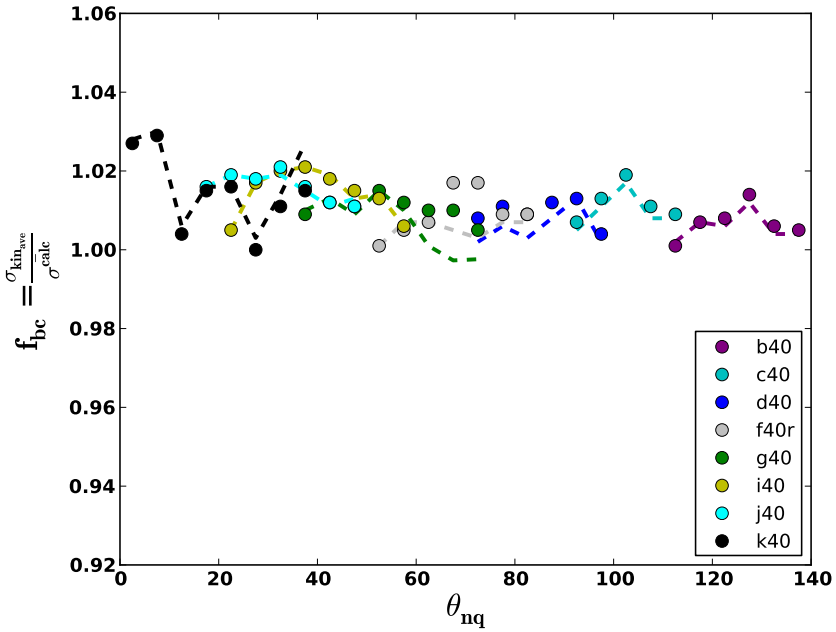

Figure 5.17: Like Fig. 5.16 for $p_m = 400$ MeV/c.

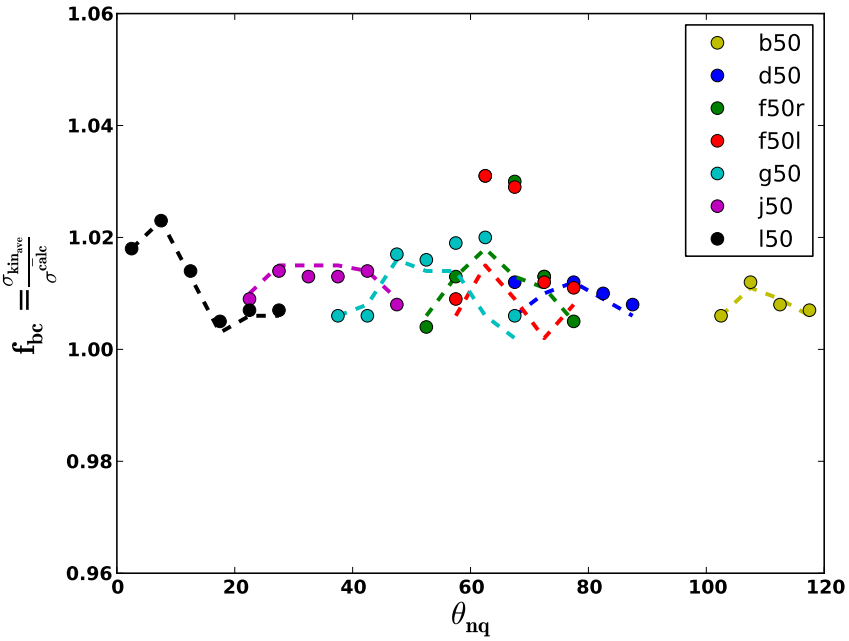

Figure 5.18: Like Fig. 5.16 for $p_m = 500$ MeV/c.

Table 5.2: Kinematics uncertainties due to the beam energy, and the particles detected in the two spectrometers

Variables	Symbols (GeV/c)	Uncertainties
Beam Energy	E_{beam}	0.3×10^{-03}
Beam out-of-plane angle	θ_{beam}	0.1 mrad
Beam in-of-plane angle	ϕ_{beam}	0.1 mrad
Electron scattered energy	e	0.15×10^{-03}
Scattered electron out-of-plane angle	θ_e	0.12 mrad
Scattered electron in-of-plane angle	ϕ_e	0.23 mrad
Outgoing proton out-of-plane angle	θ_p	0.13 mrad
Outgoing proton in-of-plane angle	ϕ_p	0.29 mrad

uncertainty propagates as a multiplication correction to the measured cross section, angular distribution and momentum distribution. Normalization uncertainties have the following sources:

- errors associated with the measurement of the density of liquid $^2H_1$ at different beam currents (uncertainties due to boiling effects)
- errors associated with the beam charge (uncertainties in luminosity measurement) measurement
- errors in the correction of inefficiencies of detectors.

The uncertainty due to kinematic variables includes the uncertainty in the beam energy, the spectrometer momenta and the scattered angles, which are given in Table. 5.2.

The kinematic errors were determined by calculating the change of the model cross section due to small variation of each of the quantities mentioned in the Table 5.2

averaged over the acceptance. For every θ_{nq} and p_m bin, the kinematic uncertainties have been calculated separately as follow. First the nominal cross section was calculated using the averaged kinematics of each bin. The uncertainties given in Table 5.2 were used in the corresponding averaged kinematics to calculate eight other cross sections. The fractional shifts of the eight cross sections from the nominal cross section determine the uncertainty due to each kinematic variable for the given bin:

$$\epsilon = \frac{\sigma(x's) - \sigma(x + \delta x)}{\sigma(x's)} \tag{5.57}$$

$$S_{err} = \sqrt{(\Sigma \epsilon_i^2)} \tag{5.58}$$

where $x's$ are the kinematic variables. The sum of the squares of the systematic error and statistical errors give the total error associated with the $D(e, e'p)n$ cross section measurements.

Chapter 6

Result and Discussion

6.1 Angular Distribution

In order to study the angular dependence of FSI contributions we determined the ratio $R = \sigma_{exp}/\sigma_{pwia}$ of the experimental cross section (σ_{exp}) to the PWIA cross section (σ_{pwia}). If there were no FSI and we would have a perfect model for the deuteron, then $R = 1$ independent of θ_{nq} would be found. The experimental values of R are shown for missing momenta $p_m = 0.2, 0.4$ and 0.5 GeV/c and at $Q^2 = 0.8$ and 2.1 $(\text{GeV})^2$ in Figs. 6.1 and 6.2.

At low Q^2, the distributions are quite broad with large FSI contributions even at small angles $\theta_{nq} < 40^\circ$ and missing momenta of $p_m = 0.4$ and 0.5 GeV/c. Only small fluctuations around $R = 1$ are found for $p_m = 0.2$ GeV/c.

In contrast, at $Q^2 = 2.1(\text{GeV})^2$, R has a well defined peak at around 75° as shown in Fig.6.2. At a missing momentum $p_m = 0.2$ GeV/c, R is reduced by about 30% at θ_{nq} around 75°. For $p_m = 0.4$ GeV/c and $p_m = 0.5$ GeV/c, R increases at around 75° by factor 2.5 and 3.5 respectively. The angular dependence of R clearly indicates that FSI between the two final state nucleons at high missing momenta is highly anisotropic. For both data sets the experimental results have been compared to results from Monte Carlo simulations using Laget's Model [34] including FSI. The solid lines represent

the distributions calculated from the theoretical model. At $Q^2 = 0.8$ (GeV/c)^2 the calculated angular distributions agree well with the experimental results for $p_m = 0.2$ GeV/c and $\theta_{nq} < 40^\circ$ only. For all other kinematic settings at this momentum transfer they do not very well reproduce the experimental results for R. At $Q^2 = 2.1$ (GeV/c)^2 and at $p_m = 0.2$ GeV/c, theoretical calculations agree quite well with experimental results, while larger discrepancies exist at higher missing momenta.

Figs. 6.3 and 6.4 show the comparison of the experimental results with the results from M.Sargsian's theoretical model [5]. At $Q^2 = 0.8$ GeV^2, the discrepancy of the Sargsian model is greater for $p_m = 200$ MeV/c and $p_m = 400$ MeV/c. But the model agrees well at the high missing momentum $p_m = 500$ MeV/c. At $Q^2 = 2.1$ GeV^2, the discrepancy between the angular distribution calculated from[5] and experiment is higher at missing momentum $p_m = 500$ MeV/c. However, the model agrees well with experiment for $p_m = 200$ MeV/c and $p_m = 400$ MeV/c. M.Sargsian's model is based on the generalized eikonal approximation (GEA) as described in section 1.4. The calculation includes the PWIA, forward ,and charge-exchange FSI amplitudes, and it completely neglects the contributions from IC and MEC in the reaction. The main theoretical frame work is developed to describe electro-disintegration of the deuteron at high Q^2.

6.2 Differential Cross Sections

The measured differential cross sections as a function of θ_{nq}, the angle between the momentum transfer and the direction of the missing momentum, for fixed missing momenta $p_m = 200, 400$ and 500 GeV/c at $Q^2 = 0.8$ and 2.1 (GeV)^2 are shown in

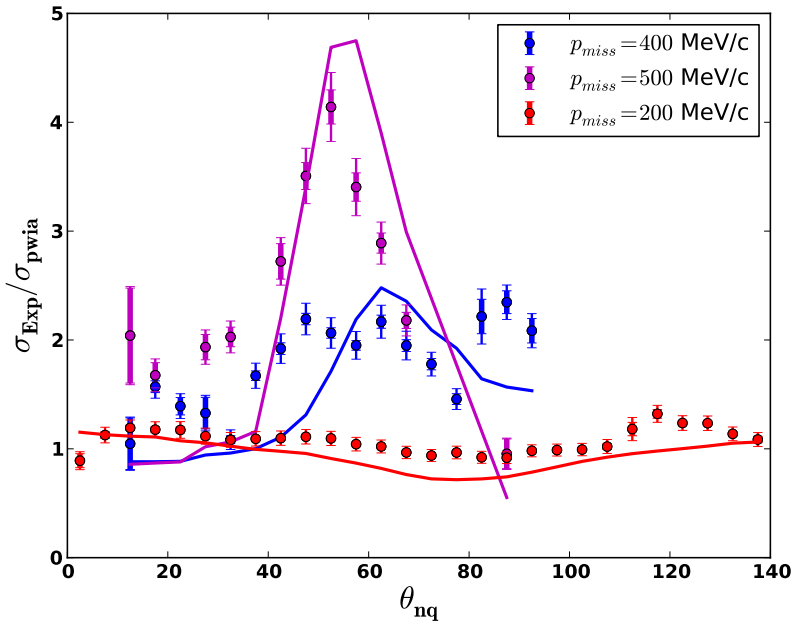

Figure 6.1: R as a function of θ_{nq} for $Q^2 = 0.8(\mathrm{GeV/c})^2$. Red: $p_m = 0.2\mathrm{GeV/c}$, blue: $p_m = 0.4$ GeV/c and magenta: $p_m = 0.5\mathrm{GeV/c}$. The corresponding sold lines represent calculations using Laget's model including FSI.

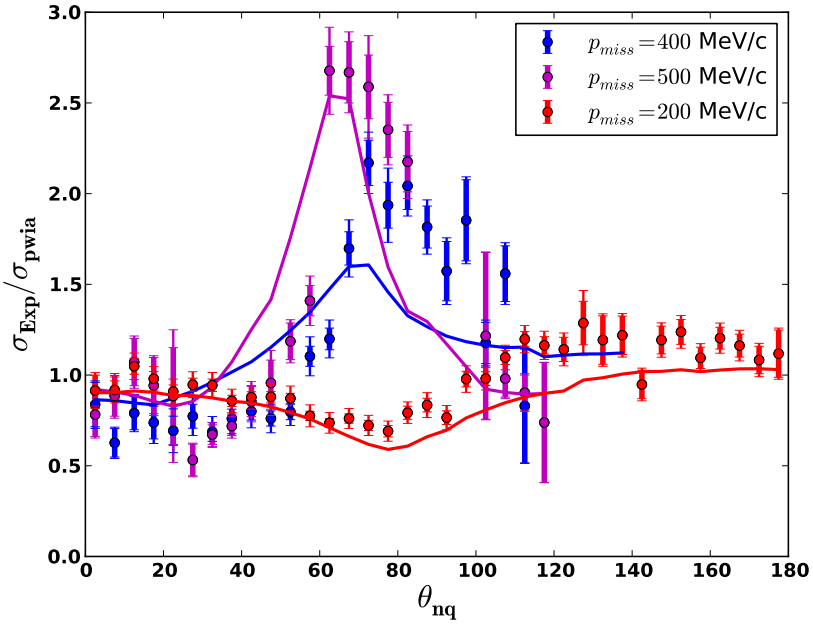

Figure 6.2: Like Fig. 6.1 for $Q^2 = 2.1$ $(\mathrm{GeV/c})^2$.

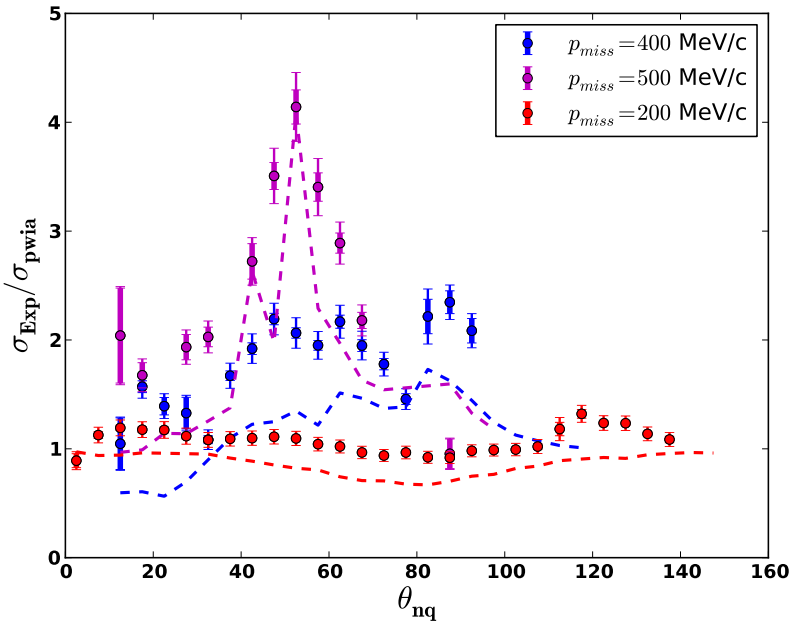

Figure 6.3: R as a function of θ_{nq} for $Q^2 = 0.8(\mathrm{GeV/c})^2$. Red: $p_m = 0.2$ GeV/c , blue: $p_m = 0.4$ GeV/c and magenta: $p_m = 0.5$GeV/c . The corresponding dashed lines represent calculations using full M. Sargsian's model including FSI.

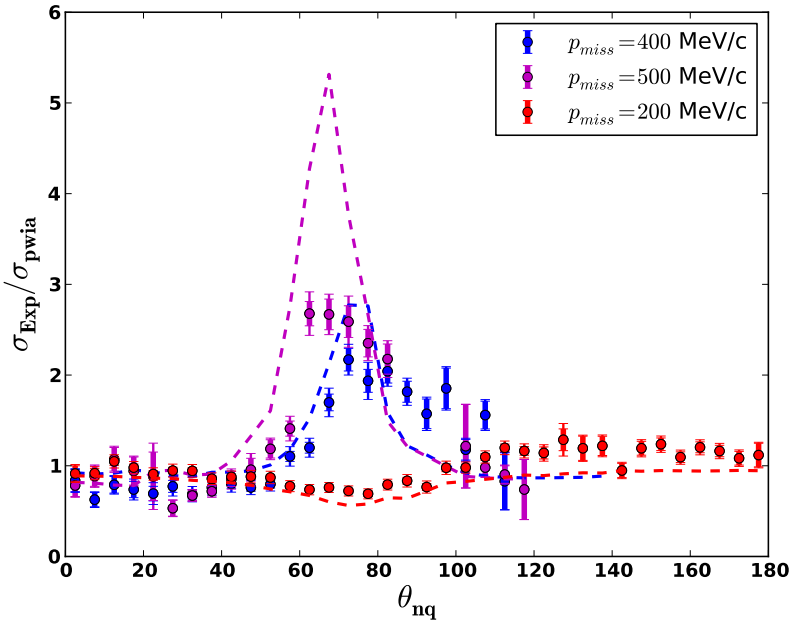

Figure 6.4: Like Fig. 6.3 for $Q^2 = 2.1$ $(\mathrm{GeV/c})^2$.

Figs. 6.5 to 6.10. They are compared to the theoretical calculation using Laget's full model including FSI. The data points with error bars are the experimentally measured values while the solid lines are the theoretical predictions. The error bars shown are the total errors. The statistical errors are plotted on the top of total errors. Total error is the absolute value of the statistical error and systematic error. When changing the kinematic settings from from one to another, the electron scattering angle θ_e as well as the energy transfer ω are changed in order to keep Q^2 constant. The small change in θ_e brings large variation in the Mott cross section, σ_{mott}, where $\sigma_{mott} \propto \frac{cos^2(\theta_e)}{sin^4(\theta_e/2)}$. Thus, variations of the cross section in different kinematic settings are observed at same θ_{nq} binning. The identification of the kinematic settings on the basis of spectrometer angles and momentum are given in Appendix A

In both data set for $p_m = 200$ MeV/c, as shown in Figs. 6.5 and 6.8, the measured cross sections agree well with the Laget model [34] for all θ_{nq} angles. At low Q^2, for $p_m = 400$ and 500 MeV/c, as shown in Figs. 6.6 and 6.7, the discrepancy between the measured cross section and the calculated one with the Laget model [34] is significantly larger everywhere. In contrast, at high Q^2, for $p_m = 400$ and 500 GeV/c, as shown in Figs. 6.9 and 6.10, the model agrees better with experimental cross sections, though considerable differences still exist for certain settings.

6.3 Deuteron Momentum Distributions

If there were no FSI, the momentum distribution could be extracted from the measured cross sections by dividing them by $K\sigma_{ep}$. In reality, FSI are always present to a certain degree and this ratio is referred to as the reduced cross section, σ_{red}.

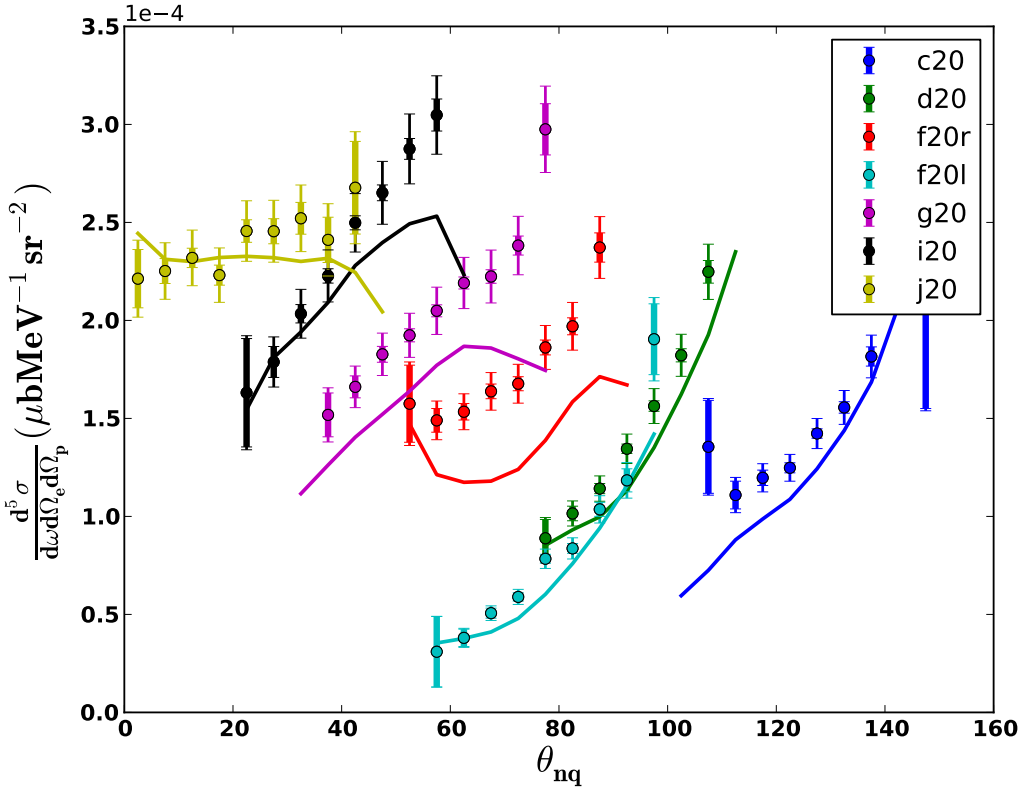

Figure 6.5: The measured reaction cross section as a function of the recoil angle θ_{nq} for missing momenta $p_m = 200$ MeV/c at $Q^2 = 0.8$ GeV^2. The solid line represents the theoretical calculation of the cross section using Laget model.

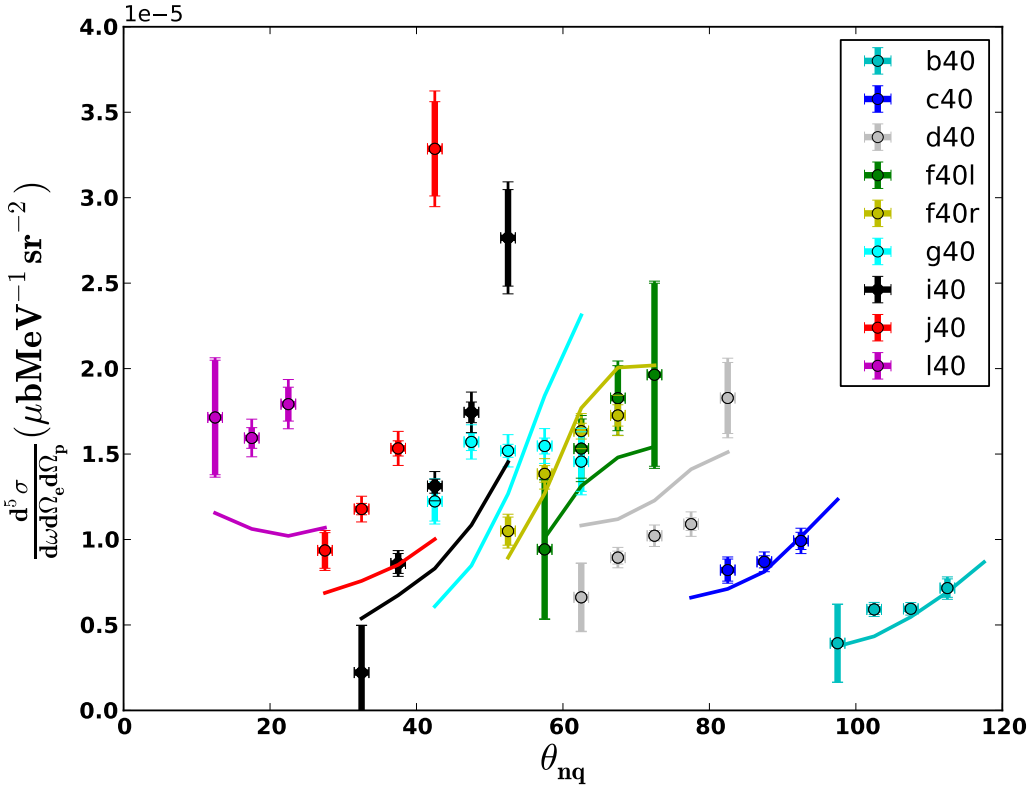

Figure 6.6: The measured cross section as a function of the recoil angle θ_{nq} for missing momenta $p_m = 400$ MeV/c at $Q^2 = 0.8$ GeV^2. The solid line represents the theoretical calculation using Laget model.

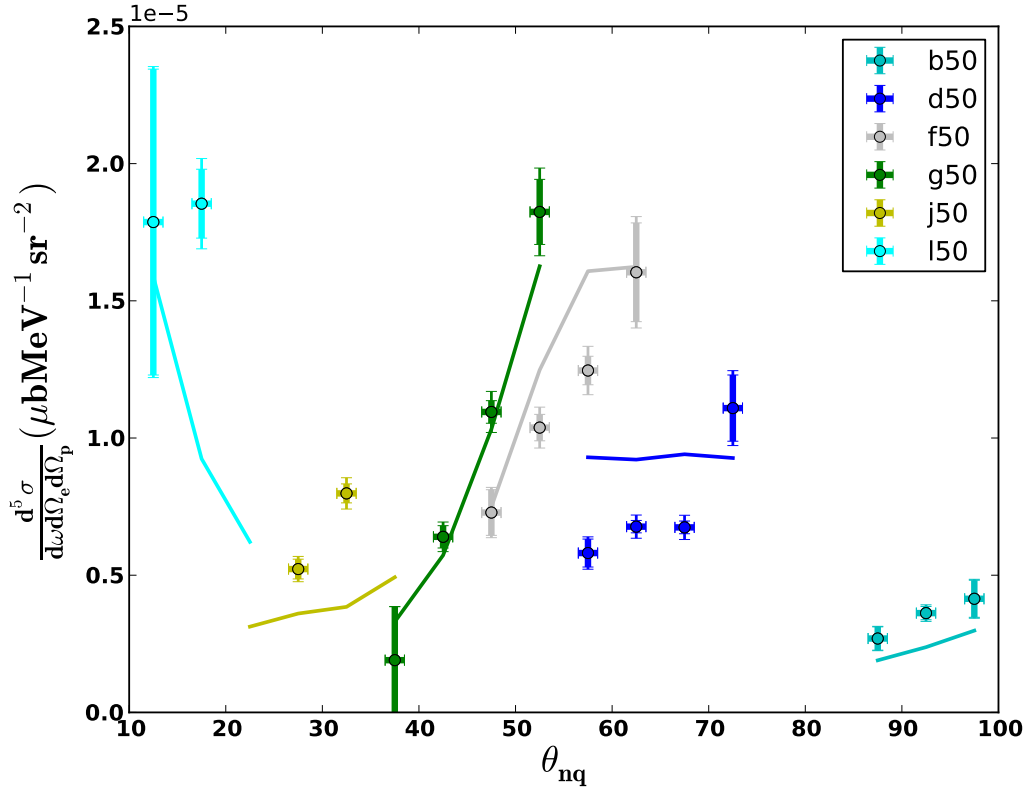

Figure 6.7: The measured cross section as a function of the recoil angle θ_{nq} for missing momenta $p_m = 500$ MeV/c at $Q^2 = 0.8$ GeV^2. The solid line represents the theoretical calculation using Laget model.

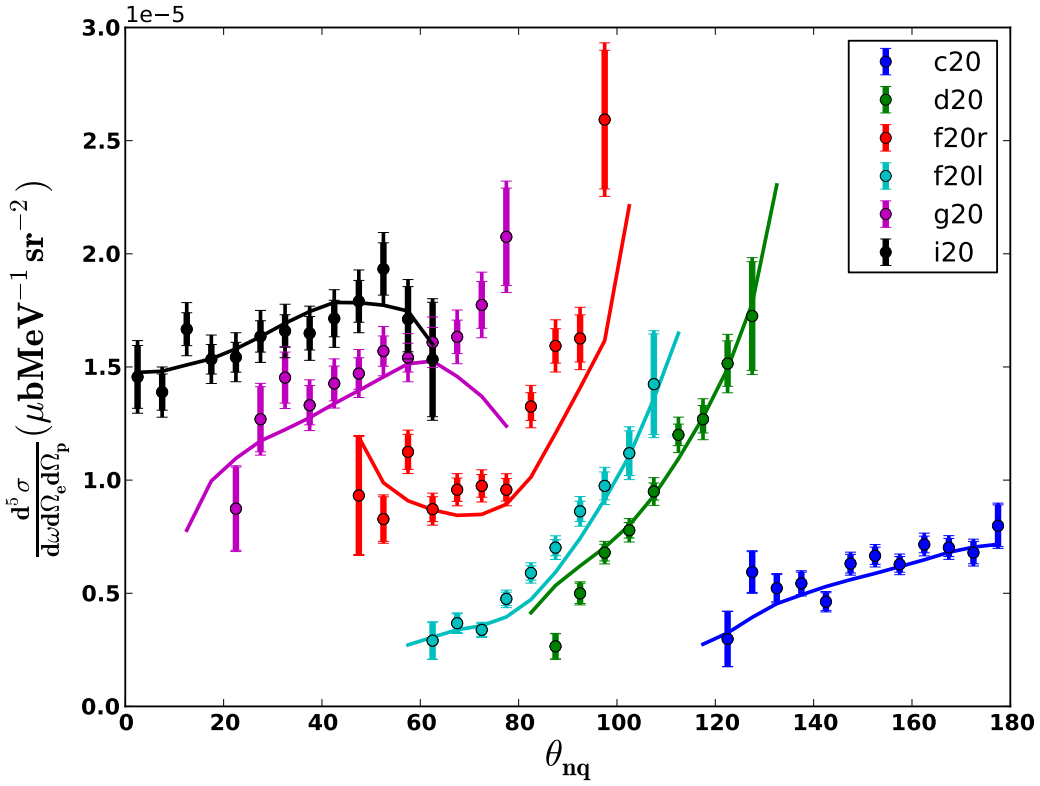

Figure 6.8: The measured cross section as a function of the recoil angle θ_{nq} for missing momenta $p_m = 200$ MeV/c at $Q^2 = 2.1$ GeV^2. The solid line represents the theoretical calculation using Laget model.

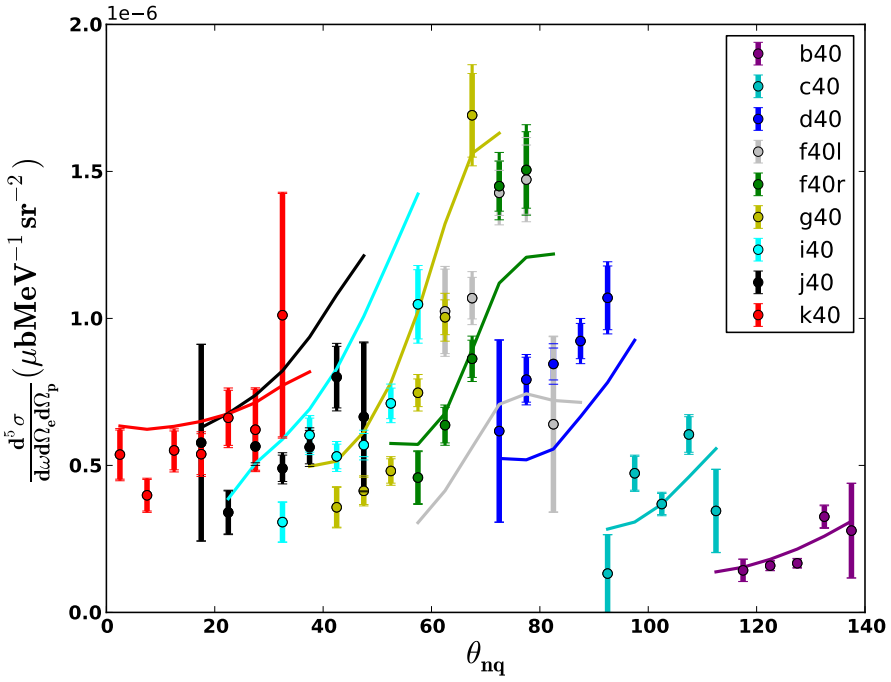

Figure 6.9: The measured cross section as a function of the recoil angle θ_{nq} for p_m = 400 MeV/c at $Q^2 = 2.1$ GeV^2. The solid line represents the theoretical calculation of the cross section using Laget model.

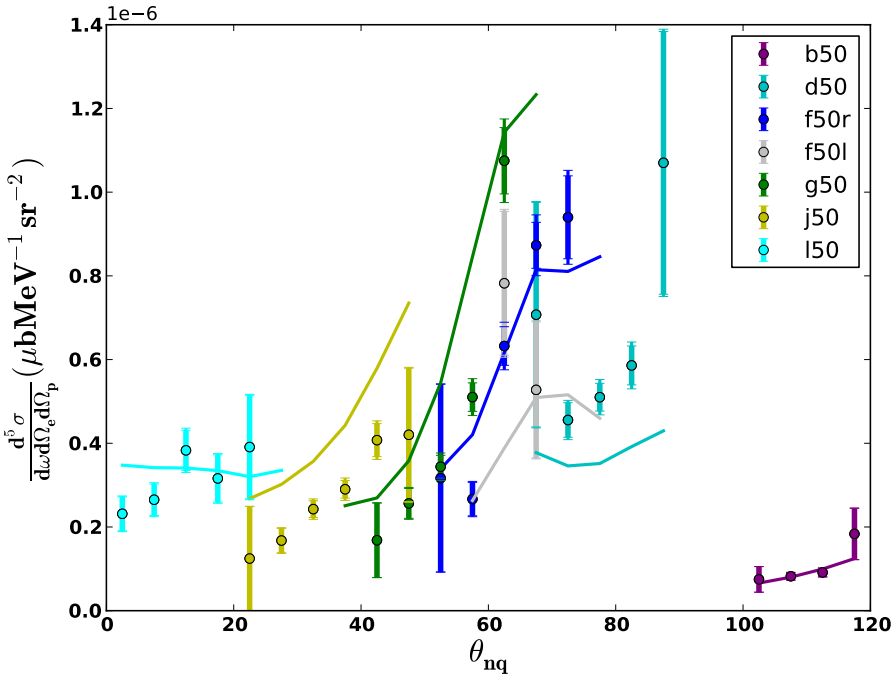

Figure 6.10: The measured cross section as a function of the recoil angle θ_{nq} for p_m = 500 MeV/c at Q^2 = 2.1 GeV ^{2}. The solid line represents the theoretical calculation of the cross section using Laget model.

Figs. 6.11 and 6.12 show the reduced cross section as a function of the missing momentum for a set of four fixed recoil angles and for $Q^2 = 0.8$ and $Q^2 = 2.1$ (GeV/c)^2. The θ_{nq} bin width of each setting of recoil angle is $\pm 5^\circ$ and the missing momentum bin width is $\pm$10MeV/c. The experimental reduced cross section has been compared to a calculation with and without FSI. At low Q^2, FSI start to contribute significantly for missing momenta above 0.2 - 0.3 GeV/c for all angles. In contrast at higher Q^2 as shown in Fig. 6.12, FSI dominate the cross section only around $\theta_{nq} = 75^0$. The experimental reduced cross sections are compared to the theoretical calculation based on J.M.Laget's [34]. For [34], the PWIA results are shown as dashed(green) and the FSI results as dashed(blue). At both Q^2 the calculations including FSI for $\theta_{nq} = 75^\circ$ agree quite well with the measurements. The PWIA calculation can reproduce the data for $p_m < 0.15$ GeV/c only. At $Q^2 = 0.8$ (GeV/c)^2, the discrepancy between the PWIA calculations and experiments is large for $p_m > 0.15$ even at small recoil angles $\theta_{nq} = 35^\circ$ and 45°, indicating large FSI. At $Q^2 = 2.1$ (GeV/c)^2 and small recoil angles, strong FSI were not observed. Therefore at small recoil angles the experimental reduced cross section closely reflects the momentum distribution of the deuteron. Fig. 6.13 shows a comparison of the experimental reduced cross sections at $Q^2 = 0.8, 2.1$ and 3.5 (GeV/c)^2 [3]. All distributions agree with each other in the low missing momentum region. Fig. 6.14 shows a comparision of experimentally measured momentum distribution at low $Q^2 = 0.8$ and 0.665 (GeV/c)^2 [4]. The data at $\theta_{nq} = 55^\circ$ agree well with [4] where data at $p_m > 400$ MeV/c lie between $\theta_{nq} = 50^\circ$ and 60°, as shown in Fig. 6.15. At large p_m values there are very big differences

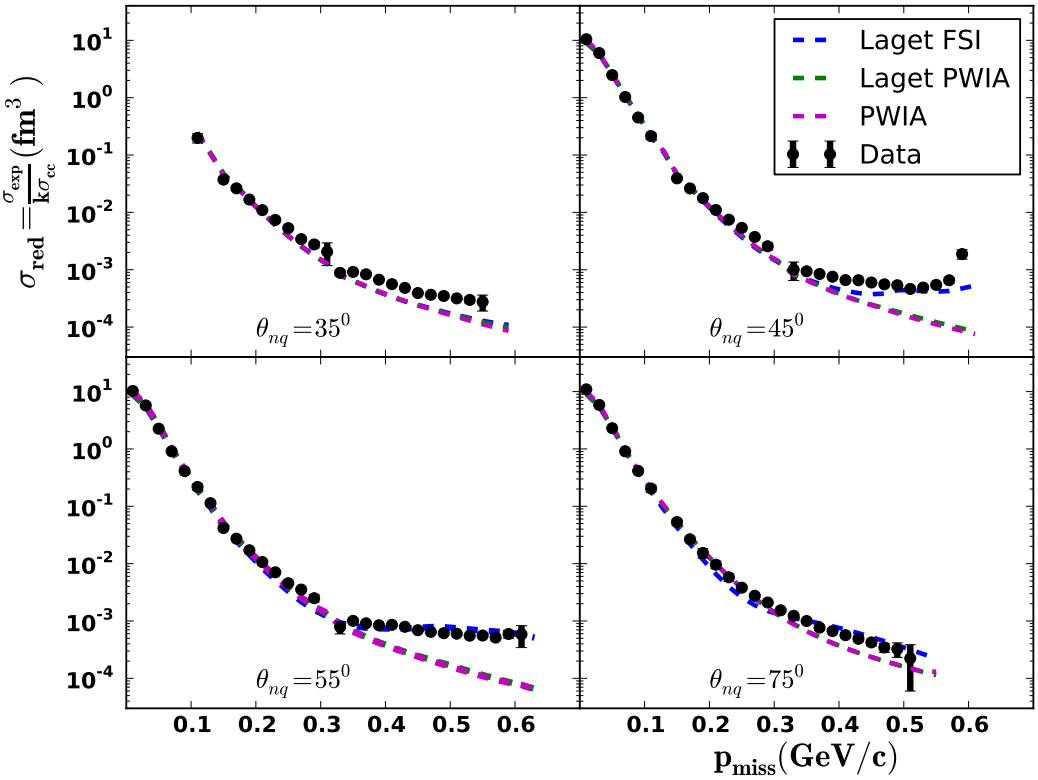

Figure 6.11: The momentum distribution as a function of missing momentum p_m at $Q^2 = 0.8$ (GeV/c)^2 for recoil angles $\theta_{nq} = 35°$, $45°$, $55°$, and 75 °. PWIA: dashed(magenta), Laget PWIA: dashed(green) and Laget with FSI: dashed(blue).

between the reduced cross sections at $Q^2 = 0.8$ and 0.665 (GeV/c)^2, and those measured at $Q^2 = 2.1$ and 3.5 (GeV/c)^2. This is an indication that at $Q^2 = 0.8$ (GeV/c)^2 the eikonal regime has not yet been reached for the description of FSI.

6.4 Summary

The goal of the experiment was a systematic study of the dynamics of the D(e, e'p)n reaction at high momentum transfer. The five-fold differential reaction cross section has been measured as a function of the recoil angle, θ_{nq}, at $Q^2 = 0.8$ and 2.1 GeV^2 for missing momenta $p_m = 0.2, 0.4$ and 0.5 GeV/c. About a 5 -6 % systematic uncertainty was included in the final results. The final results were compared to

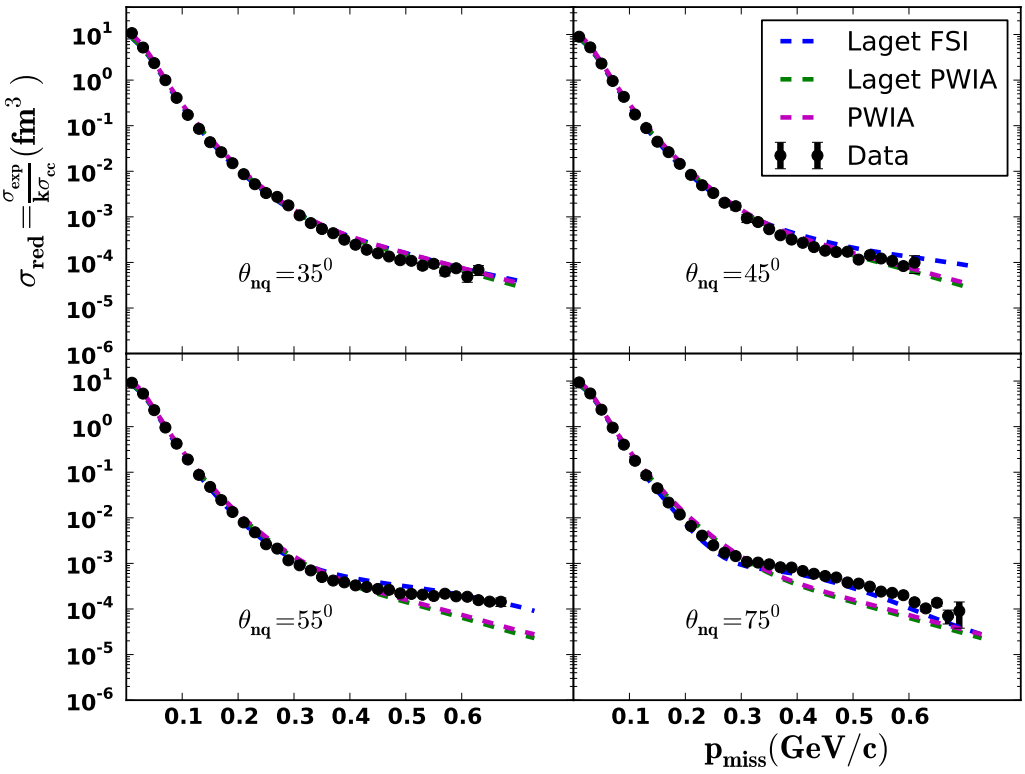

Figure 6.12: The momentum distribution as a function of missing momentum p_m at $Q^2 = 2.1$ (GeV/c)^2 for recoil angles $\theta_{nq} = 35°$, $45°$, $55°$, and $75°$. PWIA: dashed(magenta) lines, Laget PWIA: dashed(green)lines and Laget with FSI: dashed(blue) lines.

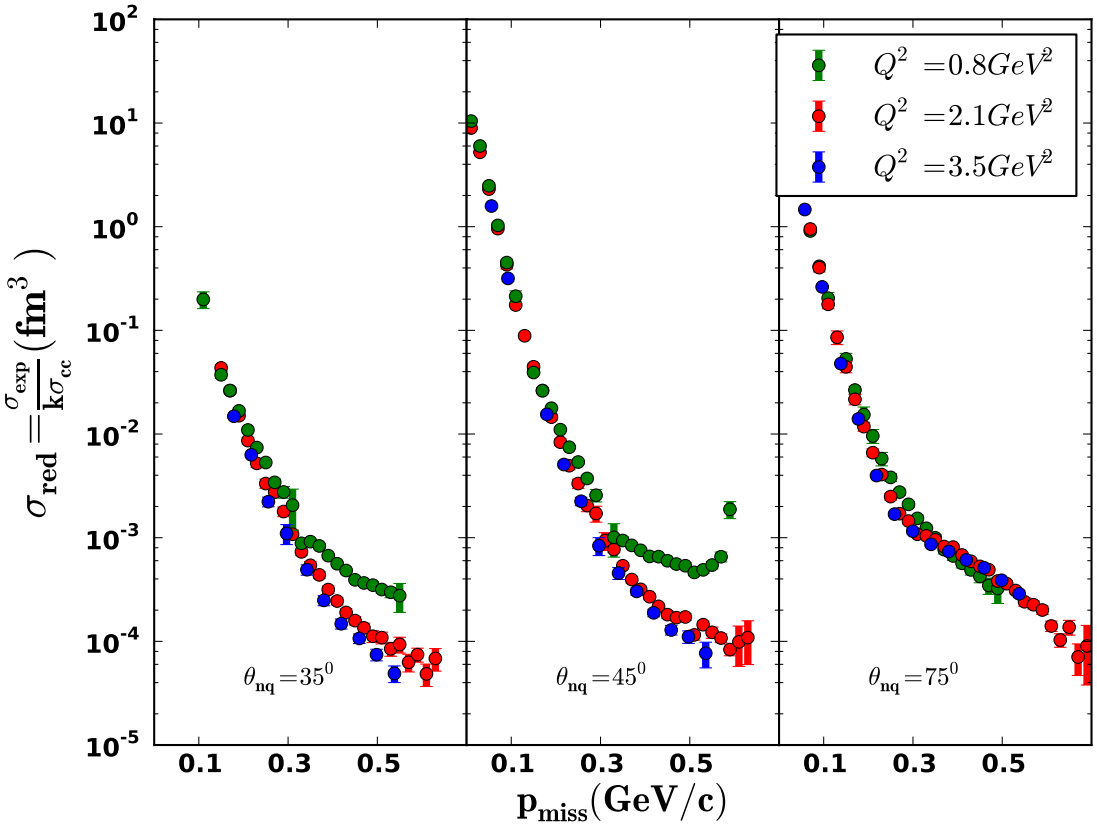

Figure 6.13: Comparison of the experimental momentum distributions for $Q^2 = 0.8$ (green), 2.1 (red), and 3.5 (GeV/c)^2 [3] (blue) for different values of θ_{nq}.

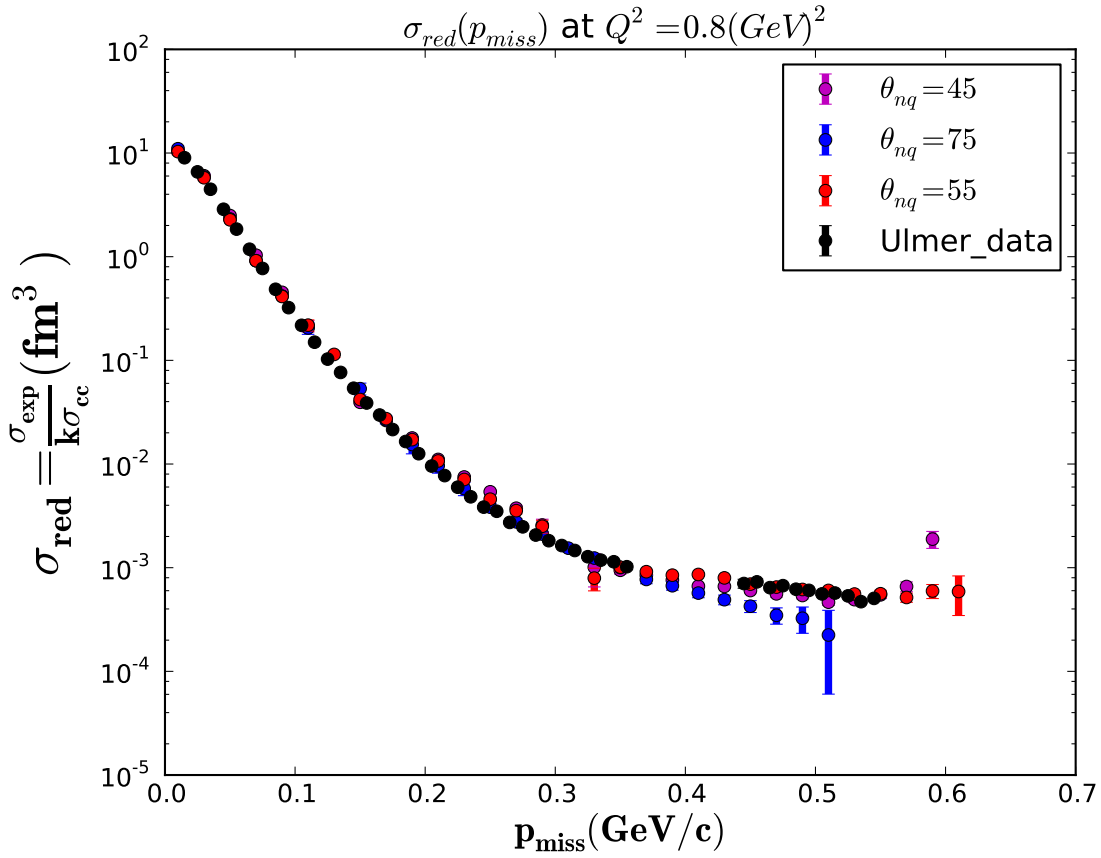

Figure 6.14: Comparison of the experimental momentum distributions for $Q^2 = 0.8$ and 0.665 (GeV/c)^2 [4] (black).

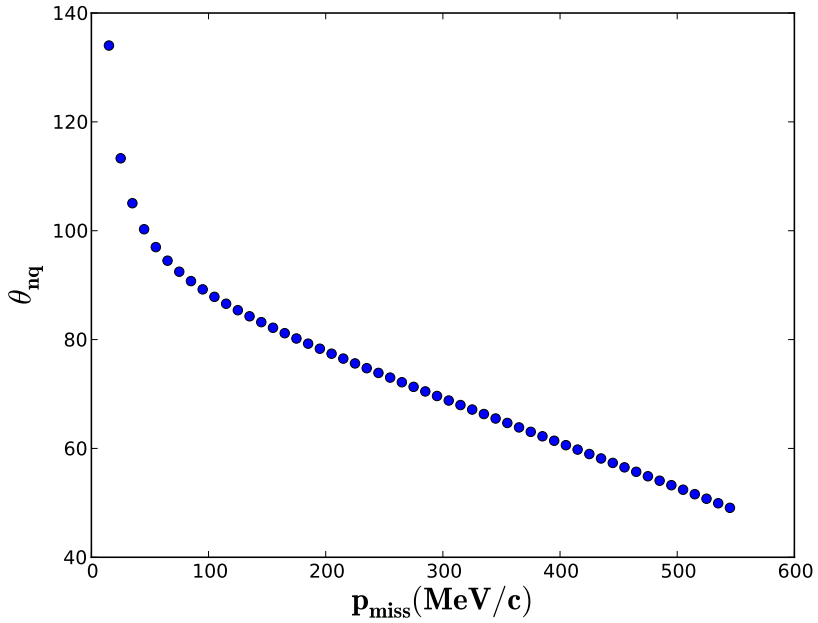

Figure 6.15: Recoil angle as a function of missing momentum calclated at $Q^2 = 0.665$ (GeV/c)^2 [4].

theortical calculation. At a few kinematic settings, especially at low Q^2 and high p_m, there are very large(a factor of 2 and more) discrepancies between the observed cross section and the calcuated one. The angular distribution of the recoiling neutron were measured at both Q^2 for fixed missing momenta p_m = 0.2, 0.4 and 0.5 GeV/c. The θ_{nq} dependency of Final State Interaction (FSI) between the proton and neutron were evaluated at both Q^2. At high Q^2, for p_m = 0.4 GeV/c and p_m = 0.5 GeV/c and θ_{nq} =75°, FSI increases the cross section, as compared to the Plane Wave Impulse Approximation (PWIA) by factor 2.5 and 3.5 respectively. However at Q^2 = 0.8 (GeV/c)^2, FSI dominates the reaction for all θ_{nq} and $p_m > 0.15$ GeV/c. The measured angular distributions were compared to theoretical calculations by M.Sargsian and J.M.Laget. From the angular distributions and the momentum distributions one can

conclude that at Q^2 = 0.8 (GeV/c)^2, FSI cannot be very well described by eikonal models while at the higher momentum transfer (Q^2 =2.1 and 3.5 (GeV/c)^2) the eikonal regime has been reached.

In addition to FSI, the non-nuclonic contributions: meson exchange currents(MEC) and isobar configuration (IC), which are expected to be higher at low Q^2, are not addressed properly in the existing theoretical models. The understanding of short-range part of the NN interaction still requires high-precision $D(e, e'p)$ cross section measurements of higher missing momenta, and improvements in the existing theoretical models are necessary.

Bibliography

[1] K.I. Blomqvist et al. *Phys. Lett. B*, 424:33, 1998.

[2] K.S. Egiyan et al. *Phys. Rev. Lett.*, 98:2625, 2007.

[3] W. U. Boeglin et al. Probing the high momentum component of the deuteron at high q2. *Physics Review Letters*, 107, 2011.

[4] P.E. Ulmer et al. *Phys. Rev. Lett.*, 89:6, 2002.

[5] M.M.Sargsian. *Phys. Rev. C*, 82:14612, 2010.

[6] Marat. M. Rvachev. $^3H(e,e'p)$ *studies at* $Q^2 = 1.5\ GeV^2$. PhD thesis, Massachusetts Institute of Technology, MA, 2003.

[7] J.Alcorn et al. *Basic Instrumantation for Hall A at Jefferson Lab.* Thomas Jefferson Lab , Newsport New , VA, 2004.

[8] K.G.Fissum et al. *Nuclear Instruments and Methods*, A 474, 2001.

[9] W.Boeglin et al. $(e,e'p)$ *studies of the Deuteron at High* Q^2. Thomas Jefferson Lab , Newsport New , VA, 2002.

[10] R.J.Glauber. *Phys. Rev.*, 100:242, 1995.

[11] et al. L.L.Frankfurt. *Z.Phys.A*, 325:97, 1995.

[12] M.M.Sargsian et al. L.L.Frankfurt. *Phys. Rev. C*, 56:1124, 1997.

[13] M.M.Sargsian. *Int.J.Mod.Phys.*, 10:405, 2001.

[14] J.Mougey et al.. *Nucl.Phys.A*, 264:461, 1976.

[15] Jr. T.de Forest. *Nucl.Phys.A*, 392:232, 1983.

[16] John R. Arrington. *The inclusive electron scattering from nuclei.* PhD thesis, California Institute of Technology, CA, 1998.

[17] H.Breuker et al. *Nucl. Phys. A*, 455:641, 1986.

[18] S.Turck-Chieze et al. *Phys. Lett. B*, 142:145, 1987.

[19] H.J. Bulten et al. *Phys. Rev. Lett.*, 74:4775, 1995.

[20] M. ven der Schaar et al. *Phys. Rev. Lett.*, 66:2855, 1991.

[21] B.D. Milbrath et al. *Phys. Rev. Lett.*, 80:452, 1998.

[22] J.E. Ducret et al. *Phys. Rev. C*, 49:1783, 1994.

[23] H.Arenhovel et al. *Phys. Rev. C*, 52:1232, 1995.

[24] V.G.J. Stoks et al. *Phys. Rev. C*, 49:2950, 1994.

[25] V.G.J. Stoks R.B. Wiringa and R. Dchiavilla. *Phys. Rev. C*, 51:38, 1995.

[26] R. Machleidt. *Phys. Rev. C*, 63:024001, 2001.

[27] W.Leidemann H. Arenhovel and E.L. Tomusiak. *Phys. Rev. C*, 46:455, 1992.

[28] W.Leidemann H. Arenhovel and E.L. Tomusiak. *Phys. Rev. C*, 52:1232, 1995.

[29] T. Wilbois F. Ritz, H. Goller and H. Arenhovel. *Phys. Rev. C*, 55:2214, 1997.

[30] M.I.Strikman L.L.Frackfurt, M.M.Sargsian. *Int. J. Mod. Phys. A*, 23:2991, 2008.

[31] S. Jeshchonnek and T. W. Donnelly. *Phys. Rev. C*, 57:2438, 1999.

[32] S. Jeshchonnek and J.W. Van Orden. *Phys. Rev. C*, 57:2438, 1999.

[33] C.Ciofi delgi Atti and L.P.Kaptari. *Phys. Rev. Lett.*, 100:122301, 2008.

[34] J.M. Laget. 609:49, 2005.

[35] M.I.Strikman L.L.Frackfurt, M.M.Sargsian. *Phys. Rev. C*, 56:1124, 1997.

[36] J.M. Richard R. Vinh P. Pires M.Lacomebe, B.Loiseau and R. de Tourreil. *Phys. Rev. C*, 21:861, 1980.

[37] J.M. Laget. *Phys. Rev. Lett.*, 493:199, 1987.

[38] J.M. Laget. *Nucl. Phys. A*, 597:333, 1994.

[39] J.J Kelly. *Adv. Nucl. Phys.*, 23:75, 1996.

[40] A. Picklesimer and J.W. Van Orden. *Phys. Rev. C*, 40:290, 1989.

[41] A.S. Raskin and T.W. Donnely. *Adv. Nucl. Phys.*, 191:78, 1989.

[42] S. Frullani and J. Mougey. *Adv. Nucl. Phys.*, 14:1, 1984.

[43] The Hall A Collabration. *ESPACE MANUAL*. Thomas Jefferson Lab, Newsport New, VA, 2003.

[44] W.R. Leo. *Techniques for Nuclear and Particle Physics Experiments*. Springer-Verlag, 1994.

[45] J.Bringer et al. *Physical Review D, Particle, Fields, Gravitation, and Cosmology*. American Physical Socity, July 2012.

[46] Marat Rvachev. Effective use of jlab hall r hrs acceptance with r-function. *Massachusetts Institute of Technology*, 2001.

[47] J.Schwinger. The electromagnetic properties of the electron-radiative corrections to scattering. *Physical Review*, 76, 1949.

[48] L.W.MO and Y.S.TSAI. Radiative corrections to elastic and inelastic ep and up scattering. *Reviews of Modern Physics*, 41, 1969.

[49] H.A. Bethe and W.Heitler. *Proc. Roy. Soc*, 146-83, 1943.

[50] Dipangra Dutta. *Radiative Corrections -The SIMC Way*. Thomas Jefferson Lab , Newsport New , VA, 1999.

[51] Simc monte carlo, 2009.

[52] J.Arrington. *Phys. Rev. C*, 68:034325, 2003.

[53] John Arrington. *A-B-SIMC*. Thomas Jefferson Lab , Newsport New , VA, 2000.

[54] L. Coman. *$^2H(e,e'p)n$ studies the deuteron at high Q^2*. PhD thesis, Florida International University, FL, 2007.

[55] W. U. Boeglin et al. f_{LT} response function of $^2h(e,e'p)$ at high $q^2 = 0.33gev^2$. *Physics Review C*, 78, 2008.

Appendix A

Appendix

Table A.1: Kinematics for q2 data

Kin	E_{inc}(GeV)	E'_f(GeV)	p_f (GeV/c)	θ_e^0	ω (GeV/c)	x_{bj}	Q^2 (GeV/c)^2
b30	4.70124	2.57837	2.86151	24.5037	2.12288	0.548229	2.1
b40	4.70125	2.5697	2.83549	24.0971	2.13154	0.526755	2.1
b50	4.70123	2.56291	2.7981	23.8543	2.13834	0.513265	2.1
c20	4.70324	3.06017	2.37954	22.4969	1.64307	0.710744	2.1
c40	4.70325	3.04939	2.32691	21.9502	1.65388	0.670589	2.1
d20	4.70325	3.38175	2.03098	20.8914	1.32149	0.844453	2.1
d40	4.70325	3.37011	1.97711	20.7421	1.33315	0.822508	2.1
d50	4.70326	3.36721	1.93228	20.7498	1.33605	0.820589	2.1
f00	4.70323	3.58606	1.82502	20.2129	1.11717	0.991695	2.1
f10r	4.70324	3.61408	1.78918	20.3182	1.08917	1.03649	2.1
f10l	4.70324	3.5583	1.85204	19.9343	1.14494	0.934692	2.1
f20l	4.70325	3.56723	1.82442	20.0741	1.13601	0.957664	2.1
f20r	4.70324	3.61007	1.7763	20.2558	1.09317	1.02556	2.1
f30r	4.70326	3.60581	1.75128	20.2535	1.09745	1.01984	2.1
f30l	4.70324	3.56657	1.79667	19.8905	1.13666	0.939407	2.1
f40l	4.70325	3.57079	1.75257	19.9677	1.13247	0.951421	2.1
f40r	4.70324	3.60014	1.71783	20.1459	1.10311	1.00261	2.1
f50r	4.70324	3.59503	1.6761	19.9792	1.10819	0.980259	2.1
f50l	4.70322	3.57536	1.69962	19.882	1.12789	0.947929	2.1
g20	4.70325	3.7613	1.602	19.6333	0.941938	1.16523	2.1
g40	4.70325	3.75259	1.5408	19.6059	0.950663	1.14908	2.1
g50	4.70322	3.75198	1.49104	19.6341	0.951242	1.15164	2.1
i20	4.70325	3.84177	1.5086	19.1025	0.861486	1.23175	2.1
i40	4.70324	3.88223	1.38739	19.2962	0.821018	1.33296	2.1
j30	4.70325	3.95914	1.3371	18.7287	0.744105	1.41286	2.1
j40	4.70324	3.96358	1.289	18.804	0.739664	1.43436	2.1
j50	4.70326	3.96295	1.23614	18.8113	0.740316	1.43412	2.1
k40	4.70326	4.02995	1.20604	18.619	0.673307	1.57079	2.1
l50	4.70325	4.08452	1.08103	18.5733	0.618738	1.72388	2.1

Table A.2: Kinematics for q1 data

Kin	E_{inc} (GeV)	E'_f (GeV)	p_f (GeV/c)	θ_e^0	ω GeV	x_{bj}	Q^2 (GeV^2)
b40	2.84356	2.03542	1.37501	21.0599	0.808129	0.510446	0.8
b50	2.84358	2.03204	1.32582	20.9715	0.811522	0.503018	0.8
c20	2.84382	2.22717	1.21102	20.4125	0.616652	0.688308	0.8
c40	2.84384	2.21796	1.14678	20.1632	0.625885	0.65922	0.8
d20	2.84349	2.34055	1.06379	19.8431	0.502943	0.838678	0.8
d40	2.84348	2.33298	0.991331	19.7319	0.510502	0.814554	0.8
d50	2.84352	2.3288	0.937225	19.5446	0.514692	0.791085	0.8
f00	2.84349	2.41773	0.985919	19.4848	0.425765	0.986511	0.8
f10r	2.84353	2.43071	0.961881	19.7032	0.41282	1.04659	0.8
f10l	2.84348	2.40803	0.993632	18.9934	0.435457	0.913648	0.8
f20l	2.84349	2.41334	0.963913	19.3567	0.430145	0.962545	0.8
f20r	2.84349	2.42377	0.949099	19.4391	0.419716	0.999272	0.8
f30r	2.8435	2.40736	0.927944	19.152	0.436149	0.927176	0.8
f30l	2.84349	2.41222	0.930617	19.0119	0.431273	0.925871	0.8
f40l	2.84349	2.417	0.88142	18.8951	0.426498	0.925886	0.8
f40r	2.84354	2.41348	0.875986	19.1207	0.43005	0.939389	0.8
f50	2.84351	2.41375	0.812347	19.0789	0.429727	0.9359	0.8
g20	2.84312	2.48214	0.864234	19.1243	0.360994	1.15153	0.8
g40	2.84315	2.47515	0.783537	18.86	0.368004	1.09525	0.8
g50	2.84313	2.4765	0.712803	19.0144	0.366621	1.1176	0.8
i20	2.84315	2.52634	0.798642	18.6482	0.316807	1.26951	0.8
i40	2.84315	2.52589	0.703634	18.7347	0.317278	1.27914	0.8
j20	2.84313	2.5602	0.745364	18.4753	0.28293	1.41391	0.8
j40	2.84314	2.56171	0.643514	18.572	0.281425	1.43696	0.8
j50	2.84316	2.56349	0.561957	18.6604	0.279654	1.46078	0.8
l40	2.83141	2.59943	0.55844	18.4294	0.231958	1.73475	0.8
l50	2.84314	2.61029	0.465692	18.5456	0.232874	1.76408	0.8

VITA

HARI KHANAL

	Born, Jhapa, Nepal
2002	Tribhuvan University Scholarship Award
2001	B.Sc. in Physics Tribhuvan University Kathmandu, Nepal
2005	M.Sc. in Physics Tribhuvan University Kathmandu, Nepal
2005 - 2007	Faculty Member Xavier International College Kathmandu, Nepal
2008 - 2009	Graduate Teaching Assistant Florida International University Miami, Florida
2009 - 2014	Graduate Research Assistant Florida International University Miami, Florida
2008 - 2014	PhD Candidate Florida International University Miami, Florida

PUBLICATIONS AND PRESENTATIONS

(e,e'p)n Studies at High Q^2 "H.P.Khanal, W.Boeglin" *Hall A Annual Report JLab -2013*

The study of the D(e,e'p)n Reaction at High Four-Momentum Transfer "H.Khanal" *Bulletin of APS -2013*

Electroproduction of K^+ at JLab Hall -C, "T.Gogami ...H.Khanal", *Few-Body Sys 2013 53:1227-1230*

Electroproduction of Light Lambda Hypernuclei, "S.N Nakarum ...H.Khanal" *Few-Body Sys 2012 013-0688*

Lifetime of Heavy Hypernuclei, "X.Qiu ...H.Khanal" *arXiv.org 1212.1133*